Lappeenranta
University of Technology

Tomi Riipinen

MODELING AND CONTROL OF THE POWER CONVERSION UNIT IN A SOLID OXIDE FUEL CELL ENVIRONMENT

Thesis for the degree of Doctor of Science (Technology) to be presented with due permission for public examination and criticism in the Auditorium 1381 at Lappeenranta University of Technology, Lappeenranta, Finland, on the 28th of November, 2012, at noon.

Acta Universitatis
Lappeenrantaensis 493

Supervisor	Professor Pertti Silventoinen Department of Electrical Engineering LUT Institute of Energy Technology (LUT Energy) Faculty of Technology Lappeenranta University of Technology Finland
Reviewers	Professor Kai Zenger Department of Automation and Systems Technology School of Electrical Engineering Aalto University Finland
	Dr. Indrek Roasto Department of Electrical Drives and Power Electronics Tallinn University of Technology Estonia
Opponent	Dr. Indrek Roasto Department of Electrical Drives and Power Electronics Tallinn University of Technology Estonia

ISBN 978-952-265-323-9
ISBN 978-952-265-324-6 (PDF)
ISSN 1456-4491

Lappeenrannan teknillinen yliopisto
Yliopistopaino 2012

Abstract

Tomi Riipinen

Modeling and Control of the Power Conversion Unit in a Solid Oxide Fuel Cell Environment

Acta Universitatis Lappeenrantaensis 493

Dissertation, Lappeenranta University of Technology
138 p.
Lappeenranta 2012
ISBN 978-952-265-323-9, ISBN 978-952-265-324-6 (PDF)
ISSN 1456-4491

In this doctoral thesis, a power conversion unit for a 10 kW solid oxide fuel cell is modeled, and a suitable control system is designed. The need for research was identified based on an observation that there was no information available about the characteristics of the solid oxide fuel cell from the perspective of power electronics and the control system, and suitable control methods had not previously been studied in the literature. In addition, because of the digital implementation of the control system, the inherent characteristics of the digital system had to be taken into account in the characteristics of the solid oxide fuel cell (SOFC).

The characteristics of the solid oxide fuel cell as well the methods for the modeling and control of the DC/DC converter and the grid converter are studied by a literature survey. Based on the survey, the characteristics of the SOFC as an electrical power source are identified, and a solution to the interfacing of the SOFC in distributed generation is proposed.

A mathematical model of the power conversion unit is provided, and the control design for the DC/DC converter and the grid converter is made based on the proposed interfacing solution. The limit cycling phenomenon is identified as a source of low-frequency current ripple, which is found to be insignificant when connected to a grid-tied converter. A method to mitigate a second harmonic originating from the grid interface is proposed, and practical considerations of the operation with the solid oxide fuel cell plant are presented.

At the theoretical level, the thesis discusses and summarizes the methods to successfully derive a model for a DC/DC converter, a grid converter, and a power conversion unit. The results of this doctoral thesis can also be used in other applications, and the models and methods can be adopted to similar applications such as photovoltaic systems.

When comparing the results with the objectives of the doctoral thesis, we may conclude that the objectives set for the work are met. In this doctoral thesis, theoretical and practical guidelines are presented for the successful control design to connect a SOFC-based distributed generation plant to the utility grid.

Keywords: DC/DC converter, resonant push-pull, voltage source inverter, current mode control, electrical power conversion, power electronics, fuel cell, SOFC
UDC 681.51:621.314:621.352:004.942

Acknowledgments

The research documented in this book has been carried out at Lappeenranta University of Technology during the years 2007–2012. The research work was conducted as a part of the SofcPower project, funded by the Finnish Funding Agency for Technology and Innovation (TEKES), and several companies involved in the project.

I would like to express my gratitude to Professor Pertti Silventoinen for giving me an opportunity to participate in this exciting research project. I also want to thank Dr. Juha-Pekka Ström and Dr. Pasi Peltoniemi for steering my doctoral thesis both in the good and bad times. Especially I want to thank Dr. Pasi Peltoniemi for the guidance and help during the process.

I have had a privilege to work with many brilliant minds. I want to thank Mr. Vesa Väisänen and Mr. Jani Hiltunen for many hours of both frustration and excitement in the laboratory, as well as fruitful conversations in the office and in the lunch breaks. I would also thank Mr. Matias Halinen and Mr. Markus Rautanen from VTT Technical Research Centre of Finland for cooperation during the project. I would also like to thank Mr. Marko Laitinen for his help during the project.

I wish to thank the preliminary examiners of this doctoral thesis, Professor Kai Zenger and Dr. Indrek Roasto for their valuable comments. Your contribution has significantly improved this work.

I am very grateful to Dr. Hanna Niemelä for her help by continuously improving the language of the thesis. Your effort made the thesis readable and more understandable, even sometimes in an unpredictable and very hectic schedule. I really appreciate your contribution and support to the writing process.

It is an old cliché that the journey is more important than the destination. Nevertheless, I must say that this journey has been a lesson in many ways. I want to thank all the people who have participated in this journey, and made it easier for me to walk the path. Dear friends, there are so many of you that it is impossible to thank each of you individually. Thus, my warmest thanks go to all of you for your support and encouragement!

Financial support for this doctoral thesis by Emil Aaltonen Foundation, Walther Ahlström Foundation, South Karelia Regional Fund, Ulla Tuominen Foundation, and the Finnish Foundation for Technology Promotion is greatly appreciated.

Last but not least, I want express my deepest gratitude to my wife Pilvikki. It is not easy to be a wife of an absent-minded researcher who has a habit of getting lost in his thoughts even during a conversation.

Our daughter Amanda, your smile reminds me of what matters most.

Espoo, November 6th, 2012

Tomi Riipinen

Contents

List of Symbols and Abbreviations

Roman letters

A	area
a	phase shift operator
$\mathbf{A}$	coefficient matrix
$\mathbf{B}$	coefficient matrix
C	capacitance
c	scaling constant
d	length
$\mathbf{C}$	controller, matrix form
$\mathbf{C}$	coefficient matrix
D	duty cycle
$\tilde{d}$	duty cycle, small signal quantity
$\mathbf{D}$	coefficient matrix
E	potential
e	electron
F, f	frequency
$\mathbf{F}$	controller, matrix form
G	plant
G	transfer function
$\mathbf{G}$	plant, matrix form
H	transfer function, filter
h	order
H	hydrogen

I	RMS current
I	current, small ripple approximation
i	current
$\tilde{i}$	current, small signal quantity
$\mathbf{I}$	identity matrix
$\mathbf{i}$	current matrix
j	imaginary unit
$\mathbf{J}$	Jacobian matrix
K	gain
$\mathbf{K}$	component value matrix
L	inductance
$\mathbf{L}$	lowpass filter, matrix form
M	conversion ratio
M	equilibrium conversion ratio
N	discrete time constant
N	word length
N, n	count
O	oxygen
P	power
p	pressure
Q	quality factor
q	quantization step
R	gas constant (8,3143 J/(mol· K)
R, r	resistance
s	Laplace variable
z	discrete z variable
$\mathbf{sw}$	switching vector
T	open-loop transfer function
T	temperature in Kelvin
T, t	period

$\mathbf{T}$	tranformation matrix
u	fuel utilization ratio
$\mathbf{U}$	signal, matrix form
$\mathbf{u}$	independent input matrix
V	RMS voltage
V	voltage, small ripple approximation
v	voltage
$\tilde{v}$	voltage, small signal quantity
$\mathbf{v}$	voltage matrix
$\mathbf{W}$	decoupling matrix
x	generic quantity
$\mathbf{x}$	generic quantity matrix
$\mathbf{x}$	state variable matrix
$\mathbf{y}$	output matrix
Z	impedance

Greek letters

α	bandwidth
α	normalizing factor
α	phase angle
α	stationary coordinates, alpha axis
β	stationary coordinates, beta axis
Δ	change of the variable
Δ	value of the least significant bit
ε	electrical permittivity
η	voltage drop resulting from losses in the fuel cell
ω	angular frequency (rad/s)
Ω	unit of resistance
ϕ	phase angle
τ	integral variable
τ	time period

θ	phase shift
ξ	damping factor
ξ	temperature coefficient

Subscripts

0	temperature-dependent reference potential
1	mono
1	inverter side
1	primary
1	state 1
2	di
2	grid side
2	secondary
2	state 2
3	state 3
4	state 4
α	stationary coordinates, alpha component
A	allpass proportion
a	anode
a	phase a
a+	switching leg a, high-side
a-	switching leg a, low-side
abc	abc coordinates
ac	AC quantity
ac	DC/AC converter
act	activation
adc	analog-to-digital converter
β	stationary coordinates, beta component
b	phase b
b+	switching leg b, high-side
b-	switching leg b, low-side

nom	nominal
cell	conditions for a single cell
C	capacitor
c	cathode
c	closed loop
c	controller
c	crossover frequency
c	phase c
c	snubber capacitor
c1	snubber capacitor 1
c2	snubber capacitor 2
cbl	cable
cc	current controller
ci	from control to input current
conc	concentration
cr	resonance capacitor
cr1	resonance capacitor 1
cr2	resonance capacitor 2
cv	from control to output voltage
dlce	double layer charging effect
d	decoupled
d	derivative
d	synchronous coordinates, d component
dc	DC link
dc	DC quantity
dsp	digital signal processor
dsvpwm	digital space vector pulse width modulator
e	equivalent
e	error
elecyt	electrolyte

fc	fuel cell
ff	feed forward
fpga	field-programmable gate array
γ	stationary coordinates, zero component
g	input
(g)	gas, or in gas phase
gas	gas form
i	integrator
interc	interconnection
inv	inverse
L	inductor
l	load
lb	boost inductance
lc	limit cycle
lk	leakage
ln	line-to-neutral
lp	low pass
M	other portion
m	modulator
mv	middle voltage
-	negative
g	grid
grid	phase-to-phase
oa	operation amplifier
ohm	ohmic
ol	open loop
+	positive
p	pole
p	proportional
pi	PI controller

pid	PID controller
plant	plant
pll	phase-locked loop
pr	proportional+resonant controller
pri	primary
q	synchronous coordinates, q component
r	resonance
r	risetime
ref	reference
ripple	ripple component
stack	stack (multiple cells in series)
s	sampling
s	switching
s1	time domain 1, fpga
s2	time domain 2, dsp
sec	secondary
sens	sensor
sw	switching
tfr	transformer equivalent
X	generic DC component
X	reactance
0	zero component
0	zero phase
z	zero

Superscripts

ch	conditions at the anode or cathode channel
’	equivalent
in	input
out	output
ref	reference

*	effective value
*	estimate
s	stationary reference frame

Acronyms

A/D	Analog-to-Digital
AA	Anti-Aliasing
AC	Alternating Current
ACC	Average Current Control
ADC	Analog-to-Digital converter
AFC	Alkaline Fuel Cell
APU	Auxiliary Power Unit
BoP	Balance of Plant
CC	Charge Control
CCM	Continuous Conducting Mode
CHP	Combined Heat and Power
CMC	Current Mode Control
D/A	Digital-to-Analog
DC	Direct Current
DCM	Discontinuous Conducting Mode
DG	Distributed Generation
DIMC	Decoupling and Diagonal Internal Model Control
DLCE	Double-Layer Charging Effect
DMFC	Direct Methanol Fuel Cell
DPWM	Digital Pulse Width Modulator
DSC	Delay Signal Cancellation
DSP	Digital Signal Processor
DSVPWM	Digital Space Vector Pulse Width Modulation
EDC-AMB	Electronics Design Center - Active Magnetic Bearings
EMC	Electromagnetic Compatibility
EMI	Electromagnetic Interference

EMIF	External Memory Interface
EU	European Union
EV	Electric Vehicle
FC	Fuel Cell
FPGA	Field Programmable Gate Array
FRA	Frequency Response Analyzer
HEV	Hybrid-Electric Vehicle
ICE	Internal Combustion Engine
IEC	International Electrotechnical Commission
IEEE	Institute of Electrical and Electronics Engineers
IIR	Infinite Impulse Response
IMC	Internal Model Control
KCL	Kirchhoff's Current Law
KVL	Kirchhoff's Voltage Law
LC	Limit Cycling
LF	Low Frequency
LHP	Left Half-Plane
LSB	Least Significant Bit
LTI	Linear Time Invariant
LUT	Lappeenranta University of Technology
MCFC	Molten Carbonate Fuel Cell
MIMO	Multiple-In, Multiple-Out
OEM	Operating Expenses and Maintenance
OS	Operating System
OSFW	Open Source Framework
P+R	Proportional+Resonant
PA	Power Available
PAFC	Phosphoric Acid Fuel Cell
PCC	Peak Current Control
PCU	Power Conversion Unit

PEMFC	Proton Exchange Membrane Fuel Cell
PI	Proportional Integral
PID	Proportional Integral Derivative
PLC	Programmable Logic Controller
PLL	Phase-Locked Loop
PMSM	Permanent Magnet Synchronous Machine
PV	Photovoltaic
PWM	Pulse Width Modulation
QPR	Quasi-Proportional-Resonant
RAM	Random Access Memory
RHP	Right Half Plane
RMS	Root Mean Square
RPP	Resonant Push-Pull
SOFC	Solid Oxide Fuel Cell
SPWM	Sinusoidal Pulse Width Modulation
SSA	State Space Averaging
SVL	Space Vector Limit
SVPWM	Space Vector Pulse Width Modulation
SW	Switching leg
VDE	Verband der Elektrotechnik
VSI	Voltage Source Inverter
VTT	VTT Technical Research Centre of Finland

Chapter 1

Introduction

The European union (EU) has agreed in 2008 that all the member states will reduce the greenhouse gases by 20% by 2020 compared with the pollution levels in year 2005. As regards the reduction of emissions, the regulations will enter into force in year 2013, as defined under the Kyoto Protocol. Together with the rising demand for energy and finite resources of fossil fuels, this boosts the research of alternative power sources.

Important methods to reduce pollution are, first, to increase the use of renewable energy sources, and second, to improve the overall efficiency of the processes and plants. Fuel cells (FCs) provide a promising solution for both cases. By fuel cells, it is possible to use bio gas as a fuel to generate electrical energy and heat. Further, by using fuel cells, it is possible to draw more energy from natural gas with a higher efficiency, compared with traditional methods.

Even though the fuel cell is a relatively old invention, it has failed to make a commercial breakthrough. The reasons for this are the high costs of the cell technology and the technical problems related to the fuel cell plants. This doctoral thesis was conducted within the SofcPower project at Lappeenranta University of Technology (LUT). The SofcPower project is a part of a project coordinated by the Technical Research Centre of Finland, VTT. The project focuses on the demonstration and analysis of a 10 kW Solid Oxide Fuel Cell (SOFC) unit. The objective is to improve the modeling and control of the fuel cell plant and the development of the suitable balance-of-plant (BoP) components.

Within the SofcPower project, the objective was to develop a power conversion unit (PCU) that is able to transform the electrical energy of the fuel cell stack into a suitable form to be supplied to the power grid. In particular, high efficiency and high reliability of the PCU were set as targets of the project. From the viewpoints of high efficiency and high reliability, the control system plays a significant role. If the system is poorly controlled, the efficiency and reliability of the system may decrease. We may also state that the system reliability and efficiency are significantly interrelated, because the efficiency is directly connected to the losses, which increase the heat to be dissipated from the system and thereby affect the system reliability. In addition, a poor control design may produce unwanted oscillations, which may lead to a malfunction or breakdown of the system.

Hence, to achieve a successful control design, a suitable model of the plant is required. To this end, the behavior of the system has to be understood. Based on the understanding of the operation principle of the

plant, it is possible to obtain a mathematical model of the plant, and further, based on the mathematical model, it is possible to understand the dynamical behavior of the plant. In this doctoral thesis, the cooperation of the PCU with the SOFC plant is studied, the PCU is modeled, and the control system is designed and implemented. The control design is based on the guidelines derived from the literature and empirical research.

1.1 Fuel cell

A fuel cell is an electrochemical device that converts chemical energy bound in fuel directly into electrical energy and heat. The basic idea of the fuel cell dates back to 1893, when William Grove invented the method to generate electricity from hydrogen and oxygen through a reverse water electrolysis.

Fuel cells are similar to batteries in that in both cases the energy is produced from electrochemical form during the process. On the other hand, fuel cells are similar to engine-based generators, where the energy is taken from the fuel, which is consumed during the process. Besides these characteristics, fuel cells have very little in common with combustion engines and batteries.

A fuel cell does not need charging, and when operating with pure hydrogen, the end products of the electrochemical process of the fuel cell are heat, electricity, and pure water. The fact that distinguishes fuel cells from other thermal engines is that the efficiency of the thermal engine is limited by the Carnot efficiency, whereas fuel cells do not have a constraint of this kind (Hoogers, 2003).

In this section, the basic principles of fuel cells and typical fuel cell systems are introduced. Applications for fuel cells are reviewed, a comparison of different fuel cells is made, and the characteristics of the fuel cell as an electrical power source are presented.

1.1.1 Operation principle

Unit cells form the core of the fuel cell system. A basic unit cell consists of an electrolyte layer in contact with an anode and a cathode on either side. A schematic of a single cell is presented in Fig. 1.1.

In a typical cell, the fuel is fed to the anode and the oxidant to the cathode. As a result of the electrochemical reactions taking place, positive or negative ions are conducted from one electrode to another through a membrane that produces a voltage over the electrodes. When a load is connected to the electrodes, electrons start to flow, and consequently, the chemical energy fed to the cell is converted into electrical energy.

In practical fuel cell applications, single cells must be combined together to obtain higher voltage and power levels. The stack is assembled from multiple cells in series with electrically conducting interconnects. The most common stacking methods are planar and tubular stackings.

The stack size can be several kilowatts, depending on the cell type, stacking method, and application. The trend is to increase the size of a single stack and to combine the stacks into plants from 100 kWs to megawatts. In (National Energy Technology Laboratory, 2004) it is stated that there are some fundamental

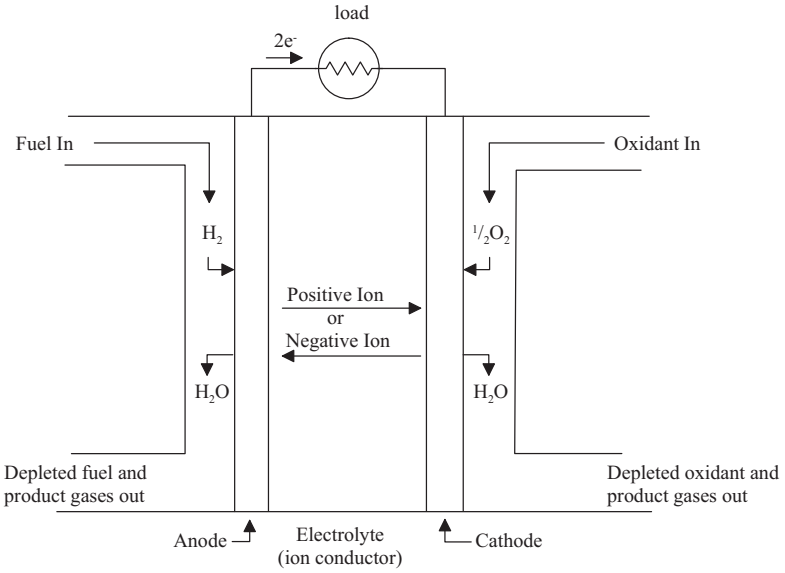

Figure 1.1. Schematic of a single unit cell. The operation of the fuel cell is based on the electrochemical reactions taking place in the cell; ions are conducted from one electrode to another through a membrane that produces a voltage over the electrodes. When a load is connected to the electrodes, this voltage makes the electrons to flow (National Energy Technology Laboratory, 2004).

limits that restrict the size of a single cell and stacks; however, these limits are out of the scope of this thesis.

1.1.2 Operating regions

The polarization curve of a fuel cell can be divided into three operating regions. In each region, the dominant source of power losses is different. The generalized polarization curve of a fuel cell is presented in Fig. 1.2.

In the figure, the following regions can be defined (National Energy Technology Laboratory, 2004; Santi et al., 2002; Hoogers, 2003):

1. Region of activation losses
2. Region of ohmic losses
3. Region of gas transport losses.

In Region 1, the main source of power losses is the activation energy losses caused by the electrochemical reactions. For very small currents, the cell voltage drops rapidly as the current increases.

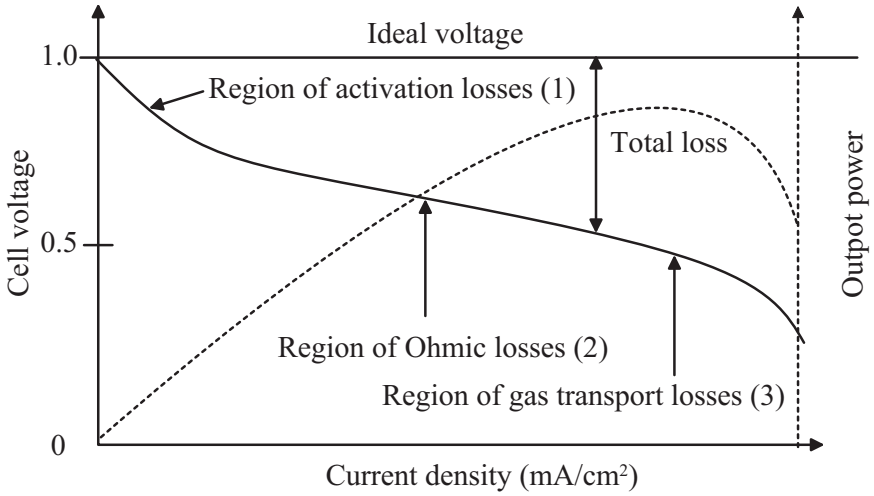

Figure 1.2. Generalized polarization curve and power output curve of the fuel cell. In the curve, three operation regions are illustrated: the region of activation losses (1), the region of ohmic losses (2), and the region of gas transport losses (3). The normal operating area of the fuel cell is in the region of ohmic losses, while operation in the region of gas transport losses can be hazardous to the cell.

Region 2 is the normal operation region of a fuel cell. In Region 2, the losses are caused by the resistance to the flow of ions in the electrolyte and the resistance of the electrode. In this region, voltage decreases, in practice, linearly as a function of current drawn from the cell.

In Region 3, the dominant source of losses is the mass-transport-related losses. The losses are based on the limited mass transport rate caused by the finite capability to transport fresh reactants and evacuate the product. After exceeding a certain value of current, the cell voltage decreases rapidly, which is also the boundary of the safe operation region.

The polarization curve is a function of fuel utilization ratio u, which defines the ratio between the energy drawn from the fuel and the energy of the reactants fed to the cell (Hatziadoniu et al., 2002). It is suggested that the fuel utilization ratio should not exceed 0.8 to limit a possible damage to the cell (Oates et al., 2002). In (Li et al., 2007) it is suggested that the allowable range for u is between 0.7 and 0.9. It must be noticed that u, and therefore the knee point between Regions 1 and 2, is a function of the feed of reactants. If we examine u and the flow of reactants in the V-I domain, the knee point moves to higher current levels when the hydrogen flow is higher (Santi et al., 2002).

1.1.3 Fuel cell types

Fuel cells are usually classified by the electrolyte used in the cell. However, another classification can be made by the fuel. Hydrocarbon-based fuels can be used in SOFCs and Molten Carbonate Fuel Cells (MCFC), which gives them competitive advantage over the fuel cells that need pure or reformed hydrogen, or methanol in the case of Direct Methanol Fuel Cells (DMFC). A list of common fuel cell types is presented in Table 1.1.

Table 1.1. Mobile ions and operating temperatures of the commonly used fuel cell technologies (Larminie and Dicks, 2003).

FC type	Mobile ion	Operating temperature	Applications and notes
Alkaline (AFC)	OH^-	50–200 °C	Space vehicles
Proton exchange membrane (PEMFC)	H^+	30–110 °C	Vehicles, mobile applications, and low-power Combined Heat and Power (CHP)
Direct methanol (DMFC)	H^+	20–90 °C	Low-power portable electronics
Phosphoric acid (PAFC)	H^+	220 °C	Several 200-kW CHP systems in use
Molten carbonate (MCFC)	CO_3^{2-}	650 °C	Medium- and large-scale CHP
Solid oxide (SOFC)	O^{2-}	500–1000 °C	All sizes of CHP

As stated above, fuel cells are suited for distributed generation (DG). On the other hand, the fuel cell technologies vary, even though the basic principle remains the same. A comparative analysis of different fuel cell types based on DG technologies is presented by Huang et al. (2006) and adapted in Table 1.2. The analysis shows that SOFCs and MCFCs offer a better efficiency compared with PEMFCs or PAFCs. As presented in the comparison, SOFC is not yet a mature technology, but it offers advantages over other cell types, and it is therefore justified to put research effort to develop the SOFC technology further.

1.1.4 Solid oxide fuel cell

Because the SOFC is in the focus of this thesis, a detailed introduction is given to the topic. The SOFC is a type of fuel cells that shares the same basic operating principles with other cells, but has some advantageous features, which makes it an interesting source of electrical power. Owing to the operation principle of the SOFC, it is able to operate basically on any combustible fuel, and it has a high conversion efficiency. The fuel specifications required by the different types of fuel cells are presented in Table 1.3.

The high operating temperature provides certain advantages compared with low-temperature fuel cells. The high temperature helps increase the efficiency that the fuel cell can reach. The high operating temperature also provides an opportunity to use a less expensive catalyst (Smith et al., 2002). In addition, the high temperature offers internal reforming, and therefore provides better fuel flexibility compared with low-temperature cell types. Another advantage of the SOFC is the utilization of the waste heat of the high operating temperature. The reported CHP efficiency can be up to 80% for the SOFC (Oates et al., 2002), while the electrical efficiency of the SOFC is >50% (Huang et al., 2006).

However, the SOFC has some problems related to high temperatures (500–1000 °C), costs, corrosion, and sealing. At high temperatures, ceramic materials are used, and therefore, issues with thermal stresses are present. The thermal expansion mismatch between materials and thereby the sealing between cells

Table 1.2. Comparison of different fuel cell types in distributed generation applications.

FC type	Advantages	Disadvantages	Electrical efficiency
PEMFC	• solid non-corrosive electrolyte • low-temperature operation • quick start-up • high power density • higher safety	• expensive platinum catalyst • sensitive to fuel impurities • lower efficiency • no internal reforming ability • expensive membrane	35–45%
PAFC	• produce high-grade waste heat • stable electrolyte characteristics	• corrosive liquid electrolyte • sensitive to fuel impurities • no internal reforming ability	40%
MCFC	• high efficiency • no metal catalysts needed • internal reforming ability	• corrosive liquid electrolyte • intolerance to sulfur • slow start-up	> 50%
SOFC	• solid electrolyte • high efficiency • high-grade waste heat • flexible fuel	• moderate intolerance to sulfur • slow start-up • no practical fabrication process yet • technology is not mature yet	> 50%

Table 1.3. Fuel requirements by different types of fuel cells (Larminie and Dicks, 2003).

Gas species	PEMFC	AFC	PAFC	MCFC	SOFC
H_2	Fuel	Fuel	Fuel	Fuel	Fuel
CO	Poison (>10ppm)	Poison	Poison (>0.5%)	Fuel[a]	Fuel[a]
CH_4	Diluent	Diluent	Diluent	Diluent[b]	Diluent[b]
CO_2 and H_2O	Diluent	Poison[c]	Diluent	Diluent	Diluent
S (as H2S and COS)	Few studies to date	Unknown	Poison (>50ppm)	Poison (>0.5ppm)	Poison (>1.0ppm)

[a] In reality, CO reacts with H_2O producing H_2 and CO_2 through a shift reaction, and CH_4 with H_2O reforms to H_2 and CO faster than reacting as a fuel at the electrode.
[b] A fuel in the internal reforming of MCFC and SOFC.
[c] The fact that CO_2 is a poison for the alkaline fuel cell more or less rules out its use with reformed fuels.

causes problems in flat plate configurations. The high operating temperature places rigorous demands on materials and results in a laborious fabrication process. Moreover, corrosion of metal stack components poses challenges to the SOFC stack. These factors limit the power density of the stack, efficiency, and stack lifetime (National Energy Technology Laboratory, 2004).

A single SOFC cell is composed of three main components: a porous cathode (air-side electrode), a porous anode (fuel-side electrode), and an ion-conducting ceramic membrane. In general, there are two major structural options for the SOFC: tubular and planar cells. When comparing tubular cells with planar cells, tubular cells suffer from higher manufacturing costs and ohmic losses. The high operating temperature ensures sufficient movement of ions through the membrane and improves the electrochemical reactions.

1.2 Fuel cell applications

In the 1960s, the first practical fuel cells were developed and used in the US space projects Gemini and Apollo. Since then, fuel cells have been used in various applications, but a real breakthrough of the fuel cells is still ahead. Therefore, fuel cells still remain a 'new' and 'promising' technology, at least when considering their commercialization. In the following, the most interesting fields of fuel cell applications and possible commercial opportunities are introduced in brief.

1.2.1 Portable fuel cells

Portable power is a potential niche for fuel cells. The power level of most interest is seen to be approximately 1 kW, and the most interesting application is to use the fuel cell as an auxiliary power

unit (APU). Considering the opportunities of fuel cells in portable applications, the following alternatives are suggested:

- Battery replacements
- Backup power
- Auxiliary power units for vehicles

The success of portable fuel cells depends on several issues. Will the battery technology develop faster than the fuel cell technology? Can fuel cells be made small enough to fit inside portable devices? Can the price get low enough? Will there be fuel widely available? We may argue that the success of fuel cells in commercial electronics depends on the winner of the race between batteries and fuel cells (Hoogers, 2003).

1.2.2 Fuel cells in transport

For almost 100 years, internal combustion engines (ICEs) have been the most important power source for transport. The demand for cleaner, more efficient transport has boosted the development of alternative power sources for transport. For example, the research on hybrid-electric vehicles (HEV) has been intense, and for instance Toyota is already launching the third-generation Prius to the market. The next major step for the withdrawal of fossil fuels such as petrol and diesel is the penetration of electric vehicles (EV). The driving force to change over to pure electric vehicles is the fact that local emissions are zero when driving with pure electricity. Of course, this electricity has to be produced somehow, and thus, we cannot claim that electric cars are totally emission free.

Because local emissions and total emissions are obviously not the same, a method called fuel cycle analysis is used to estimate the total emissions. The fuel cycle analysis, sometimes known as 'well-to-wheel analysis', considers the emissions and energy use of a process from the extraction of raw material (well) to the motive power of a vehicle (wheel). Hoogers (2003) presents a fuel cycle analysis for vehicles powered by fuel cells, internal combustion engines, and batteries. In the analysis, hydrogen-based fuel cell cars were the best performers in terms of emissions and energy, while the battery-powered electrical vehicles had problems with upstream NO_x and SO_x emissions. It is argued that hydrogen-based fuel cell vehicles are a very promising technology, if the hydrogen can be generated in an environmentally friendly way.

Compared with fuel-cell-based vehicles, the hybrid-electric vehicles still have certain advantages at the moment. The technology is well established, and it is already in the market. Further, the manufacturing costs could be reduced by larger-scale manufacturing and less sophisticated systems, or systems with a less powerful electric mode. It was also stated that hybrid vehicles have the highest fuel cycle efficiency. On the other hand, when the hybrid drive train is already implemented, the source of electrical power can be replaced, for instance, by a fuel cell (Hoogers, 2003).

Although fuel cells still have challenges to solve in the transport use, large automotive manufacturers have lately presented new fuel cell vehicles. Daimler announced recently that the first series-produced Mercedes-Benz F-CELL has finished the 30 000 km test-run around the world in the end of 2011, while Honda already leases fuel-cell-based FCX Clarity cars in California, USA. Hyundai has their Tucson IX,

which will be in the market in small quantities in 2012. Toyota is planning to have their fuel-cell vehicles on sale in 2015, which is also a common target of many other manufacturers. Due to the fact that fuel cells are considered to be the most efficient chemical energy conversion device known (Farooque and Maru, 2001), it can be assumed that fuel cells are an interesting choice for transporting applications, where the efficiency is directly linked to the operating range.

1.2.3 Distributed generation

Based on the energy source used, DG technologies can be divided into three categories.

1. DG based on fossil fuels,
2. DG based on renewable resource energy, and
3. mixed DG based on two or more technologies.

As the target is to get rid of the dependence on fossil fuels, the DG based on fossil fuels is not a possible option for the future power generation. It is obvious that renewable resources are the main topic of interest in the abandonment of fossil fuels. The mixed generation based on two or more technologies can be a solution for the transition period; for instance, a combination of different renewable power sources such as photovoltaic (PV), wind power, or fuel cell plants.

The fuel cells have several advantages over other DG technologies (Huang et al., 2006):

- High energy conversion efficiency. When operating with fossil fuels, the energy conversion efficiency of fuel cells is 17–33% higher than that of other fossil-fuel-based DG technologies.
- Low emissions. When using hydrogen, the local emissions of the fuel cell are almost zero.
- No moving parts apart from the air and fuel compressors. Thus, fuel cells are more reliable, relatively silent, and low-vibration devices. They also have lower maintenance costs and a longer operating life compared with an equivalent coal power plant or an internal combustion engine.
- Fuel cells are modular and scalable, and quick to install. Fuel cells are designed as standard-size units, and they can be easily combined to meet any amount of power demand without a need to redesign the whole plant.
- Suitability for cogeneration. In addition to electrical power, medium- to high-temperature fuel cells provide an opportunity to CHP production. In domestic or industrial applications this means pure hot water and medium-grade heat. If there is a need for heat, this increases the efficiency of the fuel cell plant even further.

In (Xu et al., 2004), the performance of various power generation technologies is reviewed in comparison with fuel cells. The comparison is presented in Table 1.4. For the presented reasons, and based on the comparison, fuel cells are well suited for DG, and they provide an improvement to the efficiency of electricity generation. With CHP generation, the efficiency is better with other technologies, but the local emissions are close to zero.

Table 1.4. Performance of various types of power generation (Xu et al., 2004).

Technology	Diesel engine	Micro turbine	Mini turbine	Fuel cell
Size (MW)	0.03–10	0.03–0.2	0.5–10	0.1–3
OEM ($/kWh)	0.005–0.015	0.004–0.010	0.003–0.008	0.002–0.015
Electric efficiency	36–45%	18–32%	21–40%	40–57%
Usable CHP temperature	Diesel 180–190	400–650	500–1100	140–700
Combined efficiency	80–85%	80–85%	80–90%	80–85%
Availability	90–97%	90–98%	90–98%	>95%
Footprint (m^2/kW)	0.023	0.023	0.028	0.084

However, there are also several drawbacks, which have delayed the commercial success of the fuel cells:

- High initial costs. Even though the costs of fuel cell systems have decreased from the first applications in the space industry, they are still not able to compete with other DG technologies. The situation may change with the increasing costs of fossil fuels.
- Complex support and control systems. The complexity of fuel cell systems increases significantly with an on-board reformer.
- Fuel sensitivity. Many fuel cells are sensitive to impurities in the fuel. Sensitivities to impurities are presented in Table 1.3.
- Unproven track record. Since fuel cells do not have a long history of commercial usage, the reliability of the fuel cell systems has not been verified.
- There is no commercially available hydrogen distribution network.

If the technological problems can be solved, there is no fundamental reason why the hydrogen economy, along with the fuel cells, could not break through. However, at the moment, the main research objective is the cost reduction of the fuel cell systems (Guerrero et al., 2010).

1.3 Fuel cell plant in distributed generation

A fuel cell itself is not able to deliver power to the load, and therefore, a composition of auxiliary circuits is needed. This composition is often called a 'fuel cell', but a more precise term is a 'fuel cell plant'. A schematic of the distributed generation fuel cell plant is presented in Fig. 1.3 (Padullés et al., 2000), where P is the active power and Q is the reactive power. The fuel cell system comprises burners, blowers, a reformer, a heat exchanger, and a PCU.

The plant controller is a system that controls the entire fuel cell system. The plant controller usually consists of mass flow meters, thermal sensors, pressure sensors, composition analyzers, and a control unit,

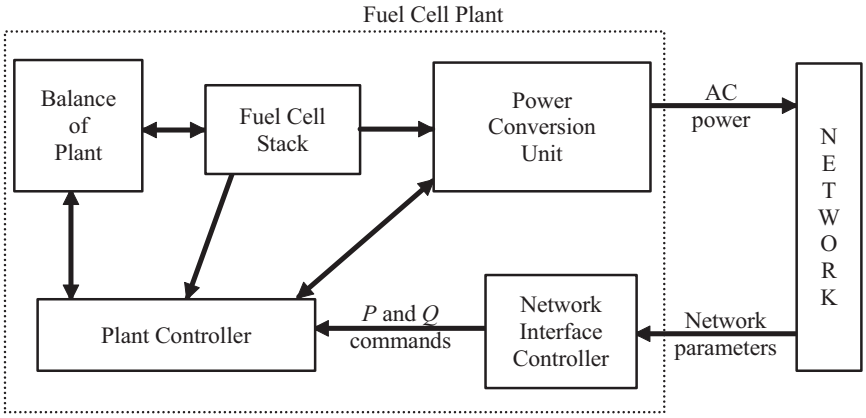

Figure 1.3. Schematic of a fuel cell power plant. The fuel cell power plant includes burners, blowers, a reformer, a heat exchanger, and a PCU. The plant controller controls the operation of the plant. Balance-of-Plant is responsible for feeding the fuel and oxidants to the process, and the PCU converts the output voltage of the fuel cell stack into a suitable form to be fed to the distribution network (Padullés et al., 2000).

such as a programmable logic controller (PLC) or an embedded system. The control unit is responsible for controlling the whole electrochemical process of the fuel cell system.

The task of the balance-of-plant unit is to feed and process the fuel and oxidants to the stack. Because the output of the fuel cell is unregulated direct current (DC), a PCU is needed to convert the low output voltage of the fuel cell into a suitable form to be fed to the distribution network.

1.3.1 Plant dynamics

A fuel cell plant is a combination of different mechanical, thermal, and electrical subsystems. Each of the subsystems has characteristic time constants, which affect the total dynamic behavior of the fuel cell system. The longest of the time constants are the thermal time constants. According to (Rajashekara, 2003), the startup time of an SOFC-based fuel cell system can be as long as 20 to 30 minutes. (Li et al., 2005) gives the response times of a 100 kW prototype SOFC plant; the hydrogen flow response time of the prototype plant is reported to be 2.91 seconds, the water flow response time 78.3 seconds, and the response time of the fuel processor 5 seconds.

The dominating time constants of the SOFC plant are given in (Wang and Nehrir, 2007a). In the small timescale, (of the order of 10^{-3}–10^{-1} s), it is stated that the double-layer charging effect (DLCE) mainly dominates the dynamic response, while in the medium timescale (from 10^{-1} to 10^{0} s), the fuel flow rate time constant is dominant, and in the large timescale (of the order of tens of minutes), the dynamic response is dominated by the thermodynamical properties of the cell.

The time constants of the fuel cell stack and the system itself are not directly related to the dynamics of the PCU unit, but it can be assumed that because of the relatively low response times of the fuel cell plant, the rate-of-change of the reference power value for the PCU is not able to change very rapidly.

We may conclude that the response rate of the fuel cell plant does not set any special requirements for the design of a PCU control system. From the perspective of the PCU, the DLCE constitutes the electrical dynamics of the fuel cell plant.

1.4 Power conversion unit

The fuel cell itself is not suitable to make a connection directly to the load. Therefore, a PCU is needed. In Fig. 1.4, the main topologies are presented for connecting the fuel cell to the load. If more power handling capacity or redundant operation is needed, the aggregation of multiple modules is possible (Ozpineci et al., 2004). Nevertheless, the main topologies remain the same. In this doctoral thesis, a DC/DC converter with a DC link and a DC/AC converter are used.

An in-depth analysis of the topologies, including the more accurate topologies of the grid converter and the DC/DC converter, is out of the scope of this thesis. Nevertheless, a brief introduction of the PCU used in this study is provided later in the thesis.

The control and operation of the PCU in an SOFC environment has some limitations and requirements that arise from the fuel cell stack, the load, and the PCU itself. In this section, the requirements and limitations of the PCU of the fuel cell plant are introduced and discussed. Here, the emphasis is on distributed generation.

1.4.1 Requirements set by the fuel cell

The requirements and limitations set by the fuel cell arise from the nature of the fuel cell system and the operation principle of the fuel cells. As described above, a fuel cell is a composition of electrochemical, mechanical, and thermal subsystems, which all affect the overall dynamics of the fuel cell power plant. In the following, the requirements set by the fuel cell plant to the PCU and the control system are discussed.

Tolerance to overcurrent

The SOFC is very vulnerable to overloading, which in practice occurs as an overcurrent and a rapid voltage drop. For the fuel cell, this means that the fuel utilization ratio is too high, and the cell may suffer from starvation and become permanently damaged (Padullés et al., 2000). The undervoltage is tightly linked to the overcurrent, which can be noticed from the polarization curve of the fuel cell (Fig. 1.2).

The output voltage of the stack is inversely proportional to the output current, and an undervoltage is always also an overloading condition. Therefore, the undervoltage is comparable with the overcurrent operation. If the plant control system sets the reference current too high, the operating point moves from the ohmic region (safe operating region) to the region of mass transport losses (hazardous region). Usually, the plant controller should detect the undervoltage situation and prevent further damages.

The overloading capability of the SOFC was investigated by Wang and Nehrir (2007b), and it was noticed that the overloading capability was mostly affected by the dynamic characteristics of the SOFC in the

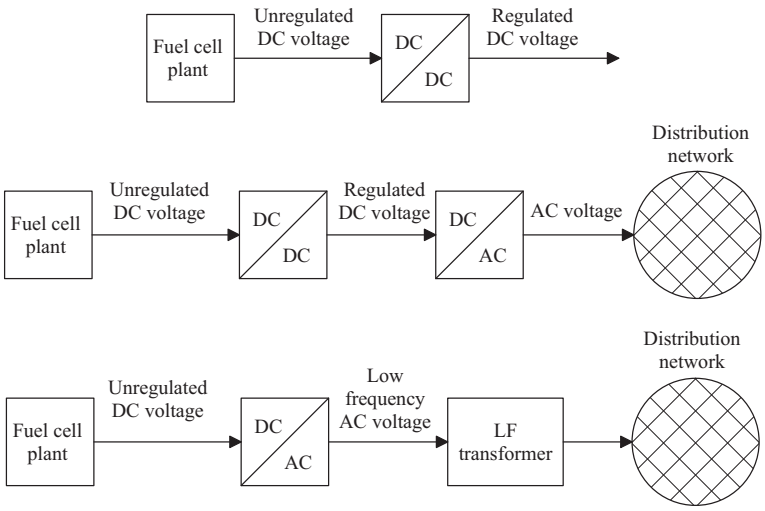

Figure 1.4. Simplified primary circuit topologies to connect the fuel cell to the load.

short and medium timescale. It was reported that the overloading capacity improved with an increase in the capacity of the DLCE and/or higher operating pressure (Wang and Nehrir, 2007b).

Current ripple tolerance

The current ripple can be divided into two parts, high- and low-frequency ripple. The origins of the ripple currents differ; the high-frequency ripple is usually produced by the switching of the DC/DC converter of the PCU, while the low-frequency ripple is caused by the grid interface in grid-connected systems.

The switching frequency ripple is always present, and it cannot be mitigated by the control system. The methods to mitigate the switching frequency ripple are to filter the output current of the stack (Liu and Lai, 2007), to choose an appropriate boost topology (Yakushev et al., 1999; Nymand and Andersen, 2008; Kwon and Kwon, 2009), to increase the switching frequency, and to improve the modulation. In (Fontes et al., 2007), it is shown that all high-frequency ripple is filtered by the double-layer equivalent capacitance, and it is therefore not harmful to the fuel cell. In spite of this conclusion, the long-term effects of the ripple current for the cell are not analyzed, and hence, more analysis is needed (Mazumder et al., 2004).

The low-frequency current ripple can be a result from the fluctuation of the DC link, which is caused by the grid-connected inverter. The fluctuation can be a consequence of an abnormal situation in the grid, too small a DC link capacitance, or a poor control design. The low-frequency ripple current is harmful to the fuel cell, because with large magnitudes it results in electrically induced thermal variations and variations in hydrogen utilization, which both have a direct impact on the performance, efficiency, and lifetime of a SOFC (Mazumder et al., 2004). Active mitigation methods for the low-frequency ripple current are presented in (Kwon et al., 2009; Liu and Lai, 2007).

Current rate-of-change

The capability of the fuel cell to produce current is proportional to the feed of fuel and oxidant (Li et al., 2007). Because the mechanical time constants are much larger than the electrical time constants, the capability to increase the feed of electricity in the transient state is proportional to the capability to increase the feed of fuel and oxidants. The difference between electrical and mechanical time constants limits the reference current rate of change to be proportional to the thermal and mechanical time constants. The reference power should be given from the plant controller to ensure that the power available from the cell is not exceeded. Usually, the power available (PA) signal is available for the PCU to operate and form a reference current.

Power requirements

A fuel cell plant can be operated in a grid-tied DG system, or it can be operated autonomously. The operating mode has a significant influence on the power requirements of the fuel cell plant. The plant can be operated for instance in a constant power flow (Candusso et al., 2002) (Li et al., 2007), constant fuel utilization (Li et al., 2005), (Li et al., 2007), constant voltage (Li et al., 2005), or load-following mode (Akkinapragada and Chowdhury, 2006). The chosen operating mode affects the chosen topology and the control scheme.

When operating in the constant power flow mode, the plant can be considered to be in a steady state, and no rapid changes in the rate of supply of fuel and oxidants are needed. Candusso et al. (2002) suggested a constant power flow scheme, where the independence of the operating point of the fuel cell is achieved with a bidirectional chopper and a supercapacitor bank. When the fuel cell plant operates in the load-following mode (or islanding), the plant must be able to respond to rapid changes in the load. If the rate of change is faster than the dynamic response of the fuel cell system, the demand for power must be drawn from an additional power storage such as a battery or a bank of supercapacitors.

Protection of the PCU

Protection schemes for the PCU are needed, despite the fact that the plant controller should not be able to operate in a region that is harmful to the SOFC or the PCU. From the viewpoint of the SOFC, the most important protection scheme for the cell is the overloading protection, and consequently, the overcurrent and undervoltage protection. Lee et al. (2006) suggest a protection scheme for residential use, which can be applied to distributed generation. The proposed protection scheme is presented in Table 1.5.

1.4.2 Requirements set by the grid

There is no universal set of grid requirements, because there is no universal standard for connecting distributed generation, even less fuel cells, to the grid. Actually, there is no worldwide standard available to connect distributed generation systems to the grid. In the following, the most important standards and grid codes are introduced in brief.

Table 1.5. Protection scheme for a PCU suggested by Lee et al. (2006).

Component	Protection
Fuel Cell	overvoltage, undervoltage, overcurrent
DC link	overvoltage, undervoltage
Load	overcurrent, short circuit
Heat sink	temperature limit for fan start, temperature limit for shutdown

Teodorescu et al. (2011) have reviewed grid standards for the connection of photovoltaic plants to the grid. The standards focus on the interconnection of distributed generation (IEEE, 2000, 2003; Underwriters Laboratories Inc, 2001), safety (VDE Verlag, 2006), EMC (Electromagnetic Compatibility) (IEC, 2000, 2003, 2005), and voltage quality (EN6100, 2005). According to Teodorescu et al. (2011), many of the standards refer to the IEEE (Institute of Electrical and Electronics Engineers) 1547 family, or have been modified to be used in conjunction with the IEEE 1547 series (IEEE, 2003).

The IEEE 1547 series does not only define the general requirements and responses to abnormal conditions, but also testing, power quality, islanding, requirements for design, production, installation evaluation, commissioning, and periodic tests. The IEEE 1547 also covers fuel cells in distributed generation.

From the viewpoint of the fuel cell stack, the most interesting part of the standards is the response to abnormal conditions. In practice, the response to abnormal grid conditions is to disconnect the distributed source from the grid. (Teodorescu et al., 2011) have presented an analytical and comparative analysis of the main grid requirements for the three main standard groups IEEE 1547/UL 1741 (IEEE, 2003; Underwriters Laboratories Inc, 2001), IEC (International Electrotechnical Commission) 61727 (IEC, 2004), and VDE (Verband der Elektrotechnik) 0126-1-1 (VDE Verlag, 2006).

Response to abnormal grid conditions

Distributed generation should observe the grid conditions while operating and respond to abnormal conditions by disconnecting the grid. This requirement is based on the safety of the utility maintenance and the general public, and protection against damages. The requirements for tripping vary depending on the standard. Based on the presented standards, it is possible to determine the behavior of the PCU when abnormal operation is detected. In this study, the standards are interpreted based on the power level below 30 kW.

Voltage deviations

Voltage deviation is the measured root mean square (RMS) voltage in the point of utility connection. The disconnection time is defined as the time from the abnormal voltage condition to the inverter tripping. The inverter needs to remain connected to the grid for monitoring purposes during reconnecting. The reason for tripping times is to ensure the ride-through capability in short-term disturbances and to avoid excessive nuisance tripping. The requirements of voltage deviation set by the corresponding standards

Table 1.6. Disconnection time for voltage variations.

IEEE 1547		IEC 61727		VDE 0126-1-1	
Voltage range (%)	Tripping time (sec.)	Voltage range (%)	Tripping time (sec.)	Voltage range (%)	Tripping time (sec.)
$V < 50$	0.16	$V < 50$	0.10	$110 \leq V < 85$	0.2
$50 \leq V < 88$	2.00	$50 \leq V < 85$	2.00		
$110 \leq V < 120$	2.00	$110 \leq V < 135$	2.00		
$V > 120$	0.16	$V > 135$	0.05		

Table 1.7. Disconnection time for frequency variations.

IEEE 1547		IEC 61727		VDE 0126-1-1	
Frequency range (Hz)	Tripping time (sec.)	Frequency range (Hz)	Tripping time (sec.)	Frequency range (Hz)	Tripping time (sec.)
$59.3 < f < 60.5$[a]	0.16	$f_n - 1 \leq f < f_n + 1$	0.2	$47.5 \leq f < 50.2$	0.2

[a] For systems with a power < 30 kW, the lower limit can be adjusted in order to participate in the frequency control.

are presented in Table 1.6.

Frequency deviations

The purpose of the allowed range of frequency deviation and time delay is to enable the ride-through capability of short-term disturbances. Improving the ride-through capability avoids excessive tripping in weak-grid situations. The requirements of frequency deviation set by the corresponding standards are presented in Table 1.7.

Reconnection after trip

After a disconnection caused by an abnormal operating condition (voltage or frequency), the reconnection of the grid converter can be made only in the conditions given in Table 1.8.

Power quality

The power quality provided by the grid converter for the AC (Alternating Current) loads or the grid is governed by several standards. The standards cover the voltage, flicker, frequency, harmonics, and power factors. A deviation from standards represents forbidden conditions, and may require disconnection of the grid converter from the utility grid.

Table 1.8. Reconnecting conditions after trip.

IEEE 1547	IEC 61727	VDE 0126-1-1
$88 < V < 110$ (%) AND $59.3 < f < 60.5$ (Hz)	$85 < V < 110$ (%) AND $f_n - 1 \leq f < f_n + 1$ (Hz) AND Minimum delay of 3 min.	

DC current injection

DC current injection to the utility grid can lead to saturation of the distribution transformers. This in turn leads to overheating and tripping. If the system is galvanically isolated, this problem is minimized.

Current harmonics

The grid converter should have low current distortion levels so that no harmful effects are caused to other grid-connected equipment. In Europe, the standard IEC 61727 is not approved, and therefore, the harmonic limits are set by the standard IEC 61000-3-2 (IEC, 2005) for Class A equipment.

Average power factor

Only in the standard IEC 61727 it is stated that a grid converter can have an average lagging power factor greater than 0.9 when the output is greater than 50%. In the standard IEEE 1547 there is no requirement for the power factor, which therefore allows distributed generation of reactive power. The standard VDE 0126-1-1 does not set any requirements for the power factor either.

Anti-islanding

Islanding is a condition of a distributed generator where the distributed generator continues to feed the grid when the grid connection is lost. Usually, this is not wanted owing to the safety of the utility workers. Anti-islanding is a method to prevent an unintended islanding situation. In the context of distributed generation, anti-islanding is a highly relevant and significant topic, which would require extensive and in-depth treatment. This, however, is beyond the scope of this thesis.

1.5 Space-vector theory

Before the modeling procedure of the three-phase VSI (Voltage Source Inverter) is introduced, it is convenient to introduce the space-vector theory and transformations. The three-phase linear system was

first described in a vector form by Park (1929), Kron (1938), and Stanley (1938), while Kovács and Rácz (1959) provided mathematical treatment along with a physical description. In the space vector theory, the three-phase linear system can be represented in a two-dimensional coordinate system. Originally, Park (1929) developed the space vector theory to describe the transient behavior of the electrical machines. Nowadays, the space vector theory is the basis of the modern three-phase control theories.

The space vector notation describes the phase variables of the three-phase system as one complex-plane variable, which has a length and a phase angle. The phase variables of the linear three-phase system can be written as

$$x_{\mathrm{a}}(t) = \hat{x}_{\mathrm{a}}(t)\cos(\theta(t) + \phi_{\mathrm{a}}(t)), \tag{1.1a}$$

$$x_{\mathrm{b}}(t) = \hat{x}_{\mathrm{b}}(t)\cos(\theta(t) + \phi_{\mathrm{b}}(t)), \tag{1.1b}$$

$$x_{\mathrm{c}}(t) = \hat{x}_{\mathrm{c}}(t)\cos(\theta(t) + \phi_{\mathrm{c}}(t)), \tag{1.1c}$$

where $\hat{x}_{\mathrm{a}}$, $\hat{x}_{\mathrm{b}}$, $\hat{x}_{\mathrm{c}}$, are the peak values of the phase variables. The phase angle $\theta(t)$ can be obtained from

$$\theta(t) = \int_0^t \omega(\tau)d\tau, \tag{1.2}$$

where $\omega(\tau)$ is the angular frequency.

Equations (1.1a), (1.1b), and (1.1c) can be written as a single complex vector and a zero-sequence component

$$\mathbf{x}^{\mathrm{s}}(t) = c\left(a^0 x_{\mathrm{a}}(t) + a^1 x_{\mathrm{b}}(t) + a^2 x_{\mathrm{c}}(t)\right), \tag{1.3a}$$

$$x_0(t) = c_0\left(x_{\mathrm{a}}(t) + x_{\mathrm{b}}(t) + x_{\mathrm{c}}(t)\right), \tag{1.3b}$$

where the superscript s denotes the stationary reference frame, a is the phase-shift operator, and c and c_0 are the scaling constants. The phase-shift operator a can be defined as

$$a = e^{j\frac{2\pi}{3}} = \cos(\frac{2\pi}{3}) + j\sin(\frac{2\pi}{3}) = -\frac{1}{2} + j\frac{\sqrt{3}}{2}. \tag{1.4}$$

The constants c and c_0 can be chosen arbitrarily, but commonly, c=2/3 and c_0=1/3 are used. This scaling is referred to as peak value scaling. Another alternative is to use the constants $c = \sqrt{2/3}$ and $c_0 = 1/\sqrt{3}$, which is referred to as power invariant scaling. In this thesis, the peak value scaling is used.

Equation (1.3a) can be written as

$$\mathbf{x}^{\mathrm{s}}(t) = x(t)e^{j\alpha(t)}, \tag{1.5}$$

where α is the phase angle of the space vector from the real axis of the stationary coordinates.

Clarke transformation

The Clarke transformation maps a three-phase linear system into a two-dimensional orthogonal system. In a symmetrical three-phase system, the absolute value of the space vector remains constant, while the phase angle varies. Thus, the space vector $\mathbf{x}^{\mathrm{s}}(t)$ circulates in the orthogonal coordinates with an angular speed of ω_{s}. The space vector $\mathbf{x}^{\mathrm{s}}(t)$ (1.3a) can be presented in a component form

$$\mathbf{x}^{\mathrm{s}}(t) = x_\alpha(t) + jx_\beta(t). \tag{1.6}$$

The α- and β-components of Equation (1.6) can be obtained by substituting Equation (1.4) into Equation (1.3a) and by observing the zero component (1.3b). This substitution can be written in the matrix form

$$\begin{bmatrix} x_\alpha \\ x_\beta \\ x_\gamma \end{bmatrix} = \mathbf{T}_{\alpha\beta\gamma} \begin{bmatrix} x_\mathrm{a} \\ x_\mathrm{b} \\ x_\mathrm{c} \end{bmatrix} = \frac{2}{3} \begin{bmatrix} 1 & -1/2 & -1/2 \\ 0 & \sqrt{3}/2 & -\sqrt{3}/2 \\ 1/2 & 1/2 & 1/2 \end{bmatrix} \begin{bmatrix} x_\mathrm{a} \\ x_\mathrm{b} \\ x_\mathrm{c} \end{bmatrix}, \tag{1.7}$$

which is known as the Clarke transformation. The inverse transformation back to *abc* coordinates can be written as

$$\begin{bmatrix} x_\mathrm{a} \\ x_\mathrm{b} \\ x_\mathrm{c} \end{bmatrix} = \mathbf{T}^{-1}_{\alpha\beta\gamma} \begin{bmatrix} x_\alpha \\ x_\beta \\ x_\gamma \end{bmatrix} = \frac{3}{2} \begin{bmatrix} 2/3 & 0 & 2/3 \\ -1/3 & \sqrt{3}/3 & 2/3 \\ -1/3 & -\sqrt{3}/3 & 2/3 \end{bmatrix} \begin{bmatrix} x_\alpha \\ x_\beta \\ x_\gamma \end{bmatrix}. \tag{1.8}$$

When the system is symmetrical, the zero component can be neglected because

$$x_\mathrm{a} + x_\mathrm{b} + x_\mathrm{b} = 0, \tag{1.9}$$

and Equation (1.7) can be written as

$$\begin{bmatrix} x_\alpha \\ x_\beta \end{bmatrix} = \mathbf{T}_{\alpha\beta} \begin{bmatrix} x_\mathrm{a} \\ x_\mathrm{b} \\ x_\mathrm{c} \end{bmatrix} = \frac{2}{3} \begin{bmatrix} 1 & -1/2 & -1/2 \\ 0 & \sqrt{3}/2 & -\sqrt{3}/2 \end{bmatrix} \begin{bmatrix} x_\mathrm{a} \\ x_\mathrm{b} \\ x_\mathrm{c} \end{bmatrix}. \tag{1.10}$$

Park transformation

The Park transformation maps an orthogonal stationary coordinate system into synchronous coordinates, which are formed by the d- and q-axes. The axes are rotated θ degrees with respect to the stationary $\alpha\beta$ reference frame. If the angular speed of the synchronous reference frame is the same as the angular speed of the three-phase system, the AC quantities of the angular frequency transform into DC quantities. The Park transformation is presented in Equation (1.11) and the inverse Park transformation in Equation (1.12).

$$\begin{bmatrix} x_\mathrm{d} \\ x_\mathrm{q} \\ x_0 \end{bmatrix} = \mathbf{T}_{\mathrm{dq0}} \begin{bmatrix} x_\alpha \\ x_\beta \\ x_\gamma \end{bmatrix} = \begin{bmatrix} \cos(\theta) & \sin(\theta) & 0 \\ -\sin(\theta) & \cos(\theta) & 0 \\ 0 & 0 & 1 \end{bmatrix} \begin{bmatrix} x_\alpha \\ x_\beta \\ x_\gamma \end{bmatrix} \tag{1.11}$$

$$\begin{bmatrix} x_\alpha \\ x_\beta \\ x_\gamma \end{bmatrix} = \mathbf{T}^{-1}_{\mathrm{dq0}} \begin{bmatrix} x_\mathrm{d} \\ x_\mathrm{q} \\ x_0 \end{bmatrix} = \begin{bmatrix} \cos(\theta) & -\sin(\theta) & 0 \\ \sin(\theta) & \cos(\theta) & 0 \\ 0 & 0 & 1 \end{bmatrix} \begin{bmatrix} x_\mathrm{d} \\ x_\mathrm{q} \\ x_0 \end{bmatrix} \tag{1.12}$$

1.6 Three-phase VSI

A three-phase VSI is equivalent to three individual single-phase inverters. A diagram of three-phase VSI with an L grid filter is presented in Fig. 1.5 When operating in the stationary $\alpha\beta$ frame, the control

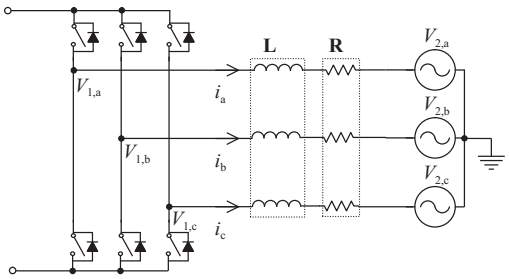

Figure 1.5. A simplified three-phase VSI with the L grid filter.

design of the three-phase current regulator can be carried out exactly as for two individual single-phase inverters. This can be shown by considering the phase interference of the system. It is pointed out that the phase interference will be canceled out when the system is mapped into the stationary $\alpha\beta$coordinates (Buso and Mattavelli, 2006).

A three-phase VSI with an L-filter can be presented as

$$L\frac{\mathrm{d}}{\mathrm{d}t}\begin{bmatrix} i_\mathrm{a} \\ i_\mathrm{b} \\ i_\mathrm{c} \end{bmatrix} = -R\mathbf{I}\begin{bmatrix} i_\mathrm{a} \\ i_\mathrm{b} \\ i_\mathrm{c} \end{bmatrix} + \frac{1}{3}\begin{bmatrix} 2 & -1 & -1 \\ -1 & 2 & -1 \\ -1 & -1 & 2 \end{bmatrix}\begin{bmatrix} v_{1,\mathrm{a}} \\ v_{1,\mathrm{b}} \\ v_{1,\mathrm{c}} \end{bmatrix} - \mathbf{I}\begin{bmatrix} v_{2,\mathrm{a}} \\ v_{2,\mathrm{b}} \\ v_{2,\mathrm{c}} \end{bmatrix}, \tag{1.13}$$

where the subscript 1 denotes an inverter-side quantity, the subscript 2 denotes a grid-side quantity, and $\mathbf{I}$ is the identity matrix. By substituting $\mathbf{x}_{\mathrm{abc}} = \mathbf{T}_{\alpha\beta}^{-1}\mathbf{x}_{\alpha\beta}$ and simplifying the matrix products, we get

$$L\frac{\mathrm{d}}{\mathrm{d}t}\mathbf{i}_{\alpha\beta} = -R\mathbf{I}\mathbf{i}_{\alpha\beta} + \mathbf{I}\mathbf{v}_{1,\alpha\beta} - \mathbf{I}\mathbf{v}_{2,\alpha\beta}. \tag{1.14}$$

Equation (1.14) shows that the phase interference is canceled out and both phases are independent of each other.

To obtain the equivalent DC circuit, the Park transformation must be applied. By noticing that there is no neutral wire connection, substituting $\mathbf{x}_{\alpha\beta} = \mathbf{T}_{\mathrm{dq}}^{-1}\mathbf{x}_{\mathrm{dq}}$, and taking into account that

$$\mathbf{T}_{\mathrm{dq}}\frac{\mathrm{d}}{\mathrm{d}t}\mathbf{T}_{\mathrm{dq}}^{-1} = \begin{bmatrix} 0 & -\omega \\ \omega & 0 \end{bmatrix}, \tag{1.15}$$

Equation (1.14) can be transformed into synchronous coordinates. Thus, a three-phase VSI with an L grid filter can be presented in synchronous coordinates with

$$L\frac{\mathrm{d}}{\mathrm{d}t}\mathbf{i}_{\mathrm{dq}} = \begin{bmatrix} -R & \omega \\ -\omega & -R \end{bmatrix}\mathbf{i}_{\mathrm{dq}} + \mathbf{I}\mathbf{v}_{1,\mathrm{dq}} - \mathbf{I}\mathbf{v}_{2,\mathrm{dq}}. \tag{1.16}$$

The procedure described here is suitable for modeling all grid filter topologies, although the L-filter was chosen because of its simplicity. Moreover, an L-filter is used to approximate the LCL filter at low frequencies (LFs), which is applied to the control design of the grid converter.

Table 1.9. 3% distortion limit of the discretization methods (Buso and Mattavelli, 2006).

Method	3% distortion limit
Backward Euler	$\frac{f_s}{f} > 20$
Forward Euler	$\frac{f_s}{f} > 20$
Tustin	$\frac{f_s}{f} > 10$

1.7 Digital control theory

The usual methods for discretization are the Backward Euler, Forward Euler, and Trapezoidal (Tustin) methods (Ogata, 1995; Åström and Wittenmark, 1997; Buso and Mattavelli, 2006). However, the effects of digitalization are not limited to mapping signals to the z-plane, but the influences extend to the computation delay, the effects of the digital pulse width modulation (DPWM), and the quantization caused by the finite word length. In the following, the most important effects of the digitalization are examined.

Z-transform

The Z-transform is an important tool in the analysis of the signals and LTI (Linear Time Invariant) systems, and we may state that it plays the same role in the discrete-time domain as the Laplace transform in the continuous-time domain. The two basic Z-transform methods to approximate the time-continuous integrals in the discrete domain are the Euler integration method and the Tustin integration method. If the approximation is considered as a graphical interpretation, the area under the curve is approximated as the sum of rectangular (Euler) or trapezoidal areas (Tustin).

Because numerical integrations are approximations, there is a difference between the time-continuous and discrete responses of the transfer functions. This distortion is known as frequency warping (Buso and Mattavelli, 2006; Åström and Wittenmark, 1997). Table 1.9 presents the limits for the ratio of the sampling frequency to the frequency of interest. It can be noticed that the Tustin approximation is more precise than the Euler method, and provides a smaller distortion at a certain frequency, or a higher frequency for the chosen distortion limit. The Z-form of the backward Euler can be written with

$$s = \frac{z-1}{zT_s}, \tag{1.17}$$

the forward Euler method with

$$s = \frac{z-1}{T_s}, \tag{1.18}$$

and the Tustin method with

$$s = \frac{2}{T_s}\frac{z-1}{z+1}. \tag{1.19}$$

We can see that with the forward Euler method it is possible that a stable continuous-time system is mapped into an unstable discrete-time system, and therefore, it should not be used. When the backward Euler is used, a stable continuous-time system is always mapped into a stable discrete-time system, and the Tustin approximation maps the LHP (Left Half Plane) inside the unit circle (Åström and Wittenmark,

1997). Thus, the backward Euler and Tustin approximations are suitable methods for the realization of digital controllers. Moreover, Buso and Mattavelli (2006) argue that the discretization methods that are more complex than the backward Euler are seldom motivated at least in PI (Proportional Integral) controllers.

Quantization

The quantization issue arises from the fact that actual systems have a finite word length, and thus, all numbers must be represented with a limited number of bits. In computing, a word is defined by a fixed set of bits that are handled by the hardware. Usually, the word length in embedded systems is 8, 16, 24, 32, or even 64 bits. For this reason, digital realization of a system is inherently nonlinear (Proakis and Manolakis, 1996).

In a binary system, it is possible to represent a word by using N bits taking 2^N separate values, where the largest possible value is $2^N - 1$ and N is the word length. Although a word is usually considered a positive integer, there is no standard definition. In practice, this means that the value of the N-bit binary word is dependent on its decoding.

Åström and Wittenmark (1997) define the following major sources for errors based on arithmetics:

- quantization in ADC (Analog-to-Digital converters),
- quantization of parameters,
- roundoff, overflow, and underflow in addition, subtraction, multiplication, division, function evaluation, and other operations, and
- quantization in D/A converters (DAC).

Delays

A digital system has inherent delays caused by transformations between the continuous and discrete time domains. A digital delay can be divided into a computational delay and a delay caused by sampling. An ADC can be modeled by different methods, but usually, an ADC is modeled as a cascade connection of an ideal sampler and a quantizer. Considering the dynamic behavior, the quantizer and the ideal sampler do not contribute to the dynamics of the system. In addition, a DPWM is another part of digital control systems involving time-domain transformations. A DPWM transforms a discrete time signal into a continuous-time signal by changing the state of the switches.

Considering the dynamics of the control algorithm, the ADC and the DPWM are points of interest. If we look at the controller as it is seen from the ADC to the DPWM, we notice that a delay occurs. This delay affects the overall performance of the control system. Therefore, it is important to develop a continuous-time equivalent model of the controller, which includes the inherent delays.

The delay can be modeled in the s-domain with

$$T_{\text{delay}}(s) = e^{-s\tau}, \tag{1.20}$$

where τ is the delay time. Because the delay presented in Equation (1.20) can be problematic to use, a first order Padé approximation can be used for easier handling of equations (Buso and Mattavelli, 2006)

$$T_{\text{delay}}(s) = e^{-s\tau} \cong \frac{1 - s\frac{\tau}{2}}{1 + \frac{\tau}{2}} \tag{1.21}$$

Because in the DPWM the transformation from the discrete to continuous-time domain is inherent, it is possible to use the standard delay equation to model the holder delay effect (Buso and Mattavelli, 2006). The delay of the holder depends on the synchronization of the DPWM, computational delays, and other delays involved in the controller loop.

Limit cycling

Limit cycling (LC) is a well-known phenomenon in digital filters (Proakis and Manolakis, 1996). In digital control, limit cycling raised interest when digital controllers were widely adopted, and this inherent problem was recognized.

In the realization of a digital filter (e.g. a digital controller), the quantization operations inherent in the finite precision arithmetics render the system nonlinear. In recursive systems, the nonlinearities resulting from the finite precision often cause periodic oscillations, called limit cycles. These oscillations are directly attributable to round-off errors in multiplication and overflow errors in addition. An extensive description of limit cycling in recursive systems is presented in (Proakis and Manolakis, 1996).

Peterchev and Sanders (2003) have studied the connection between the quantization resolution and limit cycling in digitally controlled PWM (Pulse Width Modulation) converters. Moreover, Peterchev and Sanders (2003) give three conditions to avoid limit cycling. However, even if the presented conditions are met, limit cycling may occur. Therefore, simulations are recommended (Buso and Mattavelli, 2006).

- **Condition 1**: It must be ensured that in all circumstances there is a value of the DPWM that results in a zero-error value of the error variable. This can be achieved by setting the resolution of the DPWM finer than the resolution of the ADC. It is suggested that a one-bit difference suffices in most applications.

- **Condition 2**: Even if Condition 1 is met, limit cycling may occur. The second condition defines that the controller needs to have an integrating term, the coefficient of which must be so small that it adjusts the duty cycle step similarly as the LSB (Least Significant Bit) of the DPWM.

- **Condition 3**: The third condition concentrates only on the nonlinearity of the ADC by applying the describing function (Buso and Mattavelli, 2006). This means that the feedback loop has a nonlinearity caused by the ADC, which is represented by the corresponding describing function. The describing function varies with the quantization method used. Thus, the description function included, the Nyquist stability criterion must be valid.

Figure 1.6. 10 kW SOFC prototype operated by VTT.

1.8 Plant under study

The SOFC unit operated by the VTT Technical Research Centre of Finland (VTT) was built to demonstrate a grid-connected SOFC system using natural gas as a fuel. The unit consists of two interconnected modules, the balance of the plant, and the stack module. The stack module is a 10 kW single planar module by Versa Power Systems, Inc. The SOFC plant is presented in Fig. 1.6.

1.9 Objective of the work

In this doctoral thesis, the power conversion of SOFCs is studied. The objectives of the work are to

- study how a SOFC operates as an electric power source,

- investigate how the characteristics of the SOFC affect the PCU,
- analyze how the PCU and characteristics of the SOFC affect the control design of the PCU,
- develop a model of the PCU,
- design a control system based on the developed model and the requirements set by the fuel cell plant, and finally
- verify the assumptions made on the simulation model with the prototype.

The key objective of this doctoral thesis is to find an answer to the question ”How should the PCU of the SOFC plant be controlled in distributed generation?” and to verify the solution with a prototype.

1.10 Outline of the thesis

This doctoral thesis focuses on the modeling and control of the PCU in a SOFC environment. The work focuses on the dynamical modeling of the power converting unit, study on the requirements set by the SOFC plant for the control system, and design and implementation of the control system based on the aforementioned aspects. In addition, the study addresses the digital control, where the inherent features of the digital system have an impact on the control design in the SOFC environment.

The first research question is: How does the fuel cell behave as an electrical power source? A literature study is made on the fuel cell as an electrical power source. The requirements and limitations related to the PCU are presented. A prototype PCU is built based on the literature survey on the power conditioning unit and the characteristics of the fuel cell. A prototype system has to be modeled, and therefore, modeling of the DC/DC and DC/AC stages is presented. Based on the requirements set by the fuel cell, grid, and the power electronics, a control system is designed.

The designed control system is simulated, and issues detected during the simulation are analyzed. In addition, an analysis based on the simulation model is made. The simulations focus on situations where the most notable transients occur, and which should therefore be mitigated in the stack current. Simulations are verified against an actual prototype wherever possible, taking into account the limitations set by the laboratory facilities. Finally, conclusions and suggestions for further research are made.

This doctoral thesis is divided into the following chapters:

Chapter 1 introduces the topic of fuel cells. The chapter provides a brief introduction to fuel cells in distributed generation. Further, the chapter describes the theoretical modeling process for the fuel cell system and its control. Finally, the objectives and outline of the work are described and the contributions of the study are listed.

Chapter 2 provides a model of the fuel cell, the DC/DC converter, and the grid converter. Further, the chapter theoretically analyzes the proposed models. The developed models are based on the theory presented in the introduction.

Chapter 3 presents the design of the control system for the PCU based on the developed dynamical model and the literature study. The contribution of this chapter is the design of the control system of the series connection of the DC/DC and the grid converter for the SOFC plant.

Chapter 4 presents the simulations and measurements of the proposed control system.

Chapter 5 concludes the work covered in this thesis and suggests topics for further research.

1.11 Scientific contributions of the thesis

The scientific contributions of this doctoral thesis are:

- Classification of the control requirements for the PCU in an SOFC environment.
- Formulation of a theoretical dynamic model of the resonant-push pull converter with a voltage doubler output.
- Proposition of systematic control design guidelines for the PCU in the SOFC environment.
- Development of a DSP-FPGA (Digital Signal Processor-Field Programmable Gate Array) platform architecture for the control of power electronics.
- Formulation of the theoretical models of the delays involved in the digital implementation of the presented control system.
- Proposition of the usage of a Proportional+Resonant controller in the DC/DC stage to mitigate the low-frequency grid harmonic detected in the output current of the stack.

The author has presented research results related to the topic of the doctoral thesis in the following publications:

1. T. Riipinen, V. Väisänen, M. Kuisma, L. Seppä, P. Mustonen, and P. Silventoinen, ”Requirements for power electronics in solid oxide fuel cell system,” in the *13th Power Electronics and Motion Control Conference, EPE-PEMC 2008*, 2008 (Riipinen et al., 2008).
2. T. Riipinen, O. Laakkonen, L. Lehonkoski, V. Väisänen, P. Silventoinen, and O. Pyrhönen, ”Design and analysis of FPGA-based control of a fuel cell line converter,” in the *35th Annual Conference of the IEEE Industrial Electronics Society, IECON 2009*, 2009 (Riipinen et al., 2009).
3. V. Väisänen, T. Riipinen, and P. Silventoinen, ”Effects of Switching Asymmetry on an Isolated Full-Bridge Boost Converter,” *IEEE Transactions on Power Electronics*, Vol. 25, Issue 8, 2010 (Vaisanen et al., 2010)
4. T. Riipinen, V. Väisänen, and P. Silventoinen, ”Requirements for the control system of an SOFC power conversion unit in stationary power generation,” in the *Twenty-Sixth Annual IEEE Applied Power Electronics Conference and Exposition (APEC)*, 2011 (Riipinen et al., 2011).

5. V. Väisänen, T. Riipinen, J. Hiltunen, and P. Silventoinen ”Design of 10 kW resonant push-pull DC-DC converter for solid oxide fuel cell applications,” in Proceedings of the *14th European Conference on Power Electronics and Applications (EPE 2011),* 2011 (Vaisanen et al., 2011).

The author is the primary author in publications 1, 2, and 4. The literature survey in publication 1 was made together by the authors. The author contributed to the modeling and control research.

In publication 2, the author contributed to the modeling and design of the fuel cell line inverter.

In publication 3, the author was responsible for the modeling of the converter, built the control system for the prototype, constructed the prototype with V. Väisänen, and cooperated in the measurements with V. Väisänen.

In publication 4, the author has made specific literature research to determine the requirements of the fuel cell plant and the grid interface in the design guidelines for the PCU control system.

In publication 5, the author was responsible for building and designing the control system of the prototype. The prototype was designed by V. Väisänen and J. Hiltunen, and implemented by J. Hiltunen.

Chapter 2

Modeling of the power conversion unit

2.1 Fuel cell

Numerous models to describe the dynamical behavior of the fuel cell have been proposed in the literature. Many of the models are combined thermodynamical and electrochemical models aimed to model the physical behavior of the fuel cell (Li et al., 2005; Xue et al., 2005; Chiu and Diong, 2003). Such models are usually complicated and require detailed knowledge of the cell. For an electrical engineer, a physically based model is usually unnecessarily complicated.

Another option is to model the fuel cell as an equivalent electrical circuit; for instance, by modeling the DLCE (Wang and Nehrir, 2007b) and the equivalent resistances (Fontes et al., 2007). Equivalent circuit modeling is usually familiar to an electrical engineer, and it provides enough information to design the PCU and the control system without the laborious and time-consuming process of electrochemical modeling.

Even though the fundamental electrode reaction in the SOFC differs from the reactions of the other cell types (National Energy Technology Laboratory, 2004), the operation principle remains the same. For the reason that the electrical equivalent circuit does not try to describe the exact electrochemical reactions inside the cell, the equivalent models of the fuel cells can be assumed to describe all the fuel cells with adequate precision. In the following, the SOFC modeling process proposed by Wang and Nehrir (2007a) is followed.

2.1.1 Fuel cell output voltage

The fuel cell output voltage can be determined by using the Nernst equation to calculate the reversible potential. In the SOFC the overall reaction is

$$2H_2 + O_2 = 2H_2O_{(g)}, \tag{2.1}$$

where H_2 is hydrogen, O_2 is oxygen, and the subscript (g) denotes the gas phase. Thus, reversible potential can be calculated from the corresponding Nernst equation

$$E_{\text{cell}} = E_{0,\text{cell}} + \frac{RT}{4F} \ln \left[\frac{(p^{\text{ch}}_{\text{H}_2})^2 (p^{\text{ch}}_{\text{O}_2})}{(p^{\text{ch}}_{\text{H}_2\text{O}})^2} \right], \tag{2.2}$$

where $E_{0,\text{cell}}$ is the temperature-dependent reference potential of the cell, R is the gas constant (8.3143 J/(mol·K)), T is the temperature in Kelvin, F is the Faraday constant, $p^{\text{ch}}_{\text{H}_2}$ is the hydrogen pressure, $p^{\text{ch}}_{\text{O}_2}$ is the oxygen pressure, and $p^{\text{ch}}_{\text{H}_2\text{O}}$ is the water pressure.

The temperature-dependent reference potential $E_{0,\text{cell}}$ can be expressed as

$$E_{0,\text{cell}} = E^0_{0,\text{cell}} - \kappa_E (T - 298), \tag{2.3}$$

where $E^0_{0,\text{cell}}$ is the standard reference potential in the standard state of 298 K and 1-atm pressure, κ is the empirical constant in calculating E_0, and T is the temperature in Kelvin.

The output voltage calculated from Equation (2.2) is the voltage of the cell without loading, that is, the open-circuit voltage. When the current is drawn from the cell, the losses increase as a result of the activation, ohmic, and concentration losses. The same phenomenon can be seen in the ideal voltage-current curve presented in Fig. 1.2, where the ideal voltage corresponds to the open-circuit voltage (2.2) in the current operating point.

The output voltage of a single cell can be calculated from

$$V_{\text{cell}} = E_{\text{cell}} - V_{\text{act,cell}} - V_{\text{ohm,cell}} - V_{\text{conc,cell}}, \tag{2.4}$$

where $V_{\text{act,cell}}$ is the activation voltage drop of the single cell, $V_{\text{ohm,cell}}$ is the ohmic voltage drop of the single cell, and $V_{\text{conc,cell}}$ is the concentration voltage drop of the single cell.

Based on (2.4) and assumption of the of lumped components, the output voltage of the stack, when current is drawn, can be expressed as

$$V_{\text{out,stack}} = N_{\text{cell}} V_{\text{cell}} = E_{\text{stack}} - V_{\text{act}} - V_{\text{ohm}} - V_{\text{conc}}, \tag{2.5}$$

where N_{cell} is the number of cells in the stack, E_{stack} is the open-circuit voltage of the stack, V_{act} is the activation voltage drop, V_{ohm} is the ohmic voltage drop, and V_{conc} is the concentration voltage drop. To develop an equivalent electrical circuit for the SOFC, the voltage drops V_{act}, V_{ohm}, and V_{conc} have to be determined.

2.1.2 Activation voltage drop

The activation voltage drop is caused by an activation energy barrier that has to be overcome before the chemical reaction occurs. The activation voltage drop of a single cell can be calculated from

$$V_{\text{act,cell}} = V_{\text{act0,cell}} + V_{\text{act1,cell}}, \tag{2.6}$$

where

$$V_{\text{act0,cell}} = \xi_0 + \xi_1 T \tag{2.7}$$

is the part of the activation voltage drop affected only by the internal temperature of the cell, and

$$V_{\text{act1,cell}} = iR_{\text{act,cell}} \tag{2.8}$$

is the part of the voltage drop affected by the current and the temperature.

2.1.3 Ohmic voltage drop

The ohmic voltage drop of the fuel cell is a consequence of the resistance of the electrolyte, electrodes, and the interconnection between the fuel cells in the stack. Wang and Nehrir (2007a) neglect the resistance of the electrodes, and thus, the total ohmic voltage drop can expressed as

$$V_{\text{ohm,cell}} = V_{\text{ohm,elecyt}} + V_{\text{ohm,interc}} = iR_{\text{ohm,cell}}, \tag{2.9}$$

where $V_{\text{ohm,elecyt}}$ is the ohmic voltage drop caused by the electrolyte, and $V_{\text{ohm,interc}}$ is the ohmic voltage drop caused by the interconnection. Further, $R_{\text{ohm,cell}}$ decreases as the temperature increases.

2.1.4 Concentration voltage drop

During the reaction process, there can be concentration gradients caused by diffusion in the flow channels. The effective partial pressures of oxygen and hydrogen are lower at the reaction site than in the electrode channels, as the effective partial pressure of the water at the reaction site is larger than in the anode channel. A reduction in the gas pressure will result in a reduction in the voltage (Larminie and Dicks, 2003). At high current densities, the slow transportation of the reactants to the reaction site is the dominant source of concentration losses. According to Wang and Nehrir (2007a), the equivalent concentration resistance can be expressed as

$$R_{\text{conc,cell}} = \frac{V_{\text{conc,cell}}}{i}, \tag{2.10}$$

where $V_{\text{conc,cell}}$ is the combined voltage drop of the anode and the cathode.

2.1.5 Double-layer charging effect

Two layers that consist of ions and electrons of different polarity are formed on the interface of the electrolyte and the electrode. This causes an effect called the double-layer charging effect. The two layers can be charged by the polarization effect, and they can store energy and act like a supercapacitor. The capacitance of a capacitor can be calculated from

$$C = \varepsilon \frac{A}{d}, \tag{2.11}$$

where ε is the electrical permittivity, A the surface area, and d the separation of the plates. The surface area of the electrodes is several thousand times larger than its length times width because the electrodes are porous and the separation is typically only a few nanometers. Therefore, the capacitance is very high, in some fuel cells of the order of a few farads (Larminie and Dicks, 2003). If the electrode were made more porous, the equivalent capacitance would also increase.

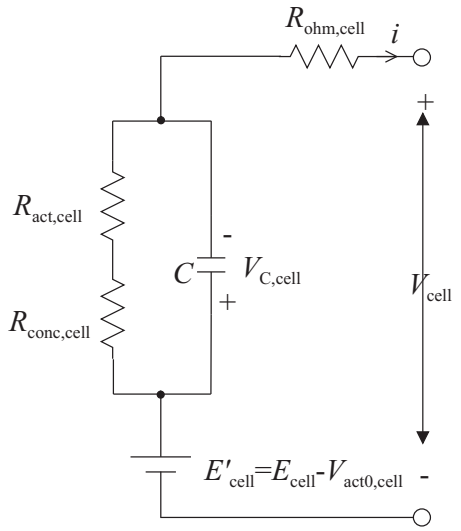

Figure 2.1. Equivalent electrical circuit of the SOFC. The equivalent circuit includes the activation voltage drop ($V_{act,cell}$), concentration losses ($R_{conc,cell}$), activation losses ($R_{act,cell}$), ohmic losses ($R_{ohm,cell}$), and the double-layer charging effect equivalent capacitor ($V_{c,cell}$) (Wang and Nehrir, 2007b)

.

According to (Wang and Nehrir, 2007b), the DLCE dominates the dynamic characteristics of the SOFC stack in the small timescale. The equivalent circuit of the DLCE used in the physically based dynamic model of the SOFC is presented in Fig. 2.1. In the figure, $R_{ohm,cell}$, $R_{act,cell}$, and $R_{conc,cell}$ are the equivalent resistances of the ohmic, activation, and concentration voltage drops, respectively, and C is the equivalent capacitance of the DLCE. The open-circuit voltage is represented as E_{cell} , and V_{act} is the activation voltage drop affected by the fuel cell operation temperature (Wang and Nehrir, 2007a). In (Fontes et al., 2007), it is suggested that in the PEMFC studied by impedance spectroscopy, the double-layer capacitor filters a majority of the high-frequency (10 kHz) ripple. The study argues that the current harmonics have no (measurable) effect on chemical reactions at high frequencies. The RC loop time constant is calculated to be 1 ms, and therefore, the capacitor has no time to charge or discharge at high frequencies.

The double-layer charging effect is modeled by using $V_{c,cell}$ to calculate the output voltage of the cell. The cell output voltage can be expressed as

$$V_{cell} = E_{cell} - V_{c,cell} - V_{act0,cell} - V_{ohm,cell}. \tag{2.12}$$

By combining Equations (2.5) and (2.12) the output impedance, and thus the output voltage, of the fuel cell stack can be calculated.

2.1.6 Development of the model

An equivalent circuit of the fuel cell is presented in Fig. 2.1, which includes the ohmic losses and the equivalent capacitance produced by the DLCE. The model can be divided into individual impedances, and the wiring inductance can be included in the model (Laffly et al., 2006). By combining the model

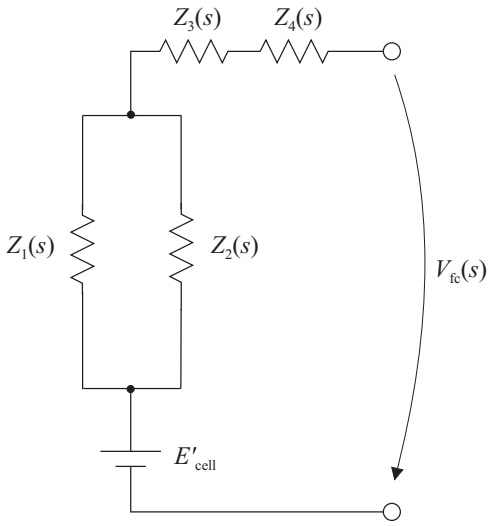

Figure 2.2. Equivalent electrical circuit of the SOFC including the cable inductance.

presented by (Wang and Nehrir, 2007a) and the cable inductance, the equivalent circuit presented in Fig. 2.2 is obtained. The corresponding equations for impedances presented in the model can be written as

$$Z_1(s) = R_{\text{act,cell}} + R_{\text{conc,cell}} \tag{2.13a}$$

$$Z_2(s) = \frac{1}{sC_{\text{dlce}}} \tag{2.13b}$$

$$Z_3(s) = R_{\text{ohm}} \tag{2.13c}$$

$$Z_4(s) = sL_{\text{cbl}} \tag{2.13d}$$

By basic algebra, the equivalent Thevenin impedance can be calculated:

$$Z_{\text{fc}}(s) = \frac{Z_1(s)Z_2(s)}{Z_1(s)+Z_2(s)} + Z_3(s) + Z_4(s). \tag{2.14}$$

By substituting Equations (2.13) into (2.14), the following transfer function for the stack impedance can be written:

$$Z_{\text{fc}}(s) = R_{\text{ohm}} + L_{\text{cbl}}s + \frac{R_{\text{act,cell}} + R_{\text{conc,cell}}}{(C_{\text{dlce}}R_{\text{act,cell}} + C_{\text{dlce}}R_{\text{conc,cell}})s + 1}. \tag{2.15}$$

Based on Equation (2.15), a Bode diagram of the fuel cell output impedance can be drawn. The example of the fuel cell output impedance of the cell used in (Fontes et al., 2007) is presented in Fig. 2.3. However, it is pointed out that this impedance should be considered as an example only, not the impedance of the stack used in the study.

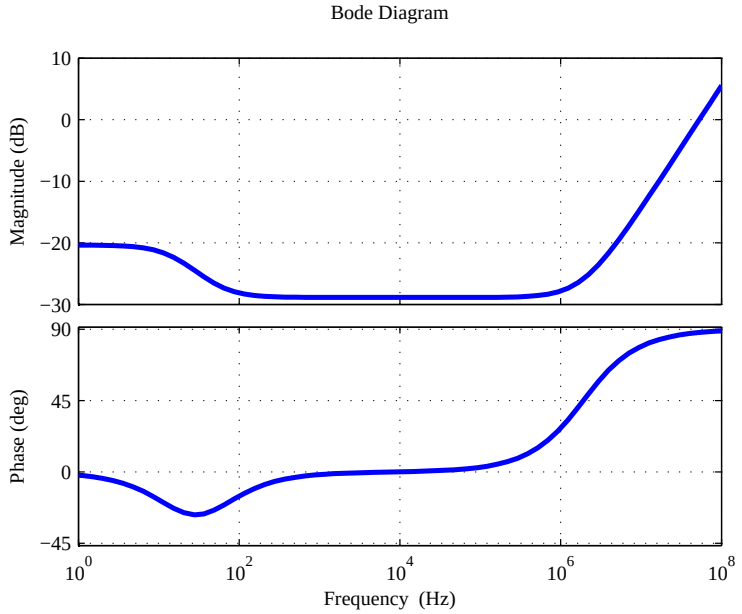

Figure 2.3. Bode diagram of the output impedance of the stack with the values presented by Fontes et al. (2007).

2.1.7 Equivalent circuit used in the thesis

Because the fuel cell equivalent parameters are not available from the manufacturer, and it is not possible to measure the equivalent capacitance of the DLCE from the stack, a steady-state model is chosen.

Pasricha et al. (2007) have reviewed multiple steady-state electrical terminal models of the PEMFC stack and verified the models against an actual stack. The best fit is provided by the simple Thevenin equivalent circuit, despite its poor predictions about the low and high currents. Because the stack parameters are not known, and the operating area for which the converter is designed is the region of ohmic losses (area 2), a Thevenin equivalent circuit is used to model the stack. Despite the lack of information, a theoretical impedance analysis is made of the stack output impedance, which can be considered as an input filter, and the DC/DC converter input impedance.

Halinen et al. (2011) have presented the performance characteristics of the SOFC unit used. The voltage-current pairs of the measurements are determined. The corresponding values are given in Table 2.1. The linear Thevenin model is acquired by applying the least squares method. By basic algebra, the following parameters for the Thevenin model can be obtained: V_{stack}=58.1 V and R_{stack}=0.0421 Ω. The measured polarization curve and the linearized model curve are plotted in Fig. 2.4.

Table 2.1. Measured data from the prototype stack and the linearized model.

Voltage [V]	Current [A]
52.5	140
51.8	148
51.0	160
50.7	176
49.8	200

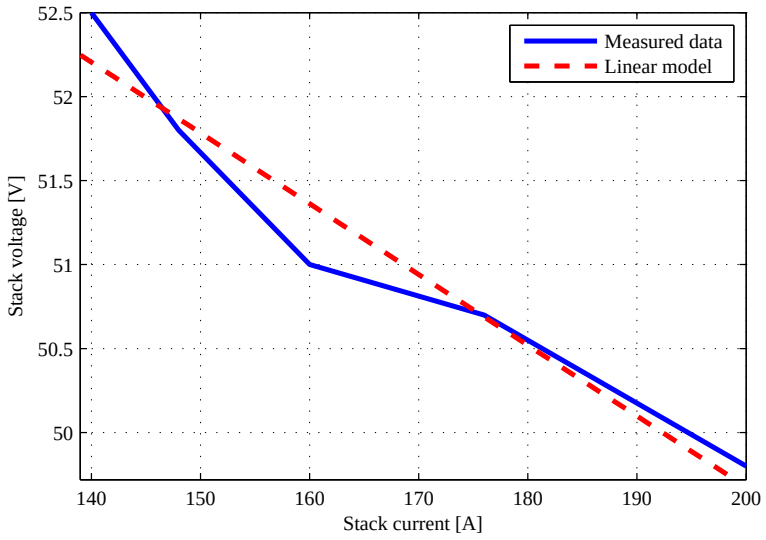

Figure 2.4. Stack data measured from the prototype cell (Halinen et al., 2011) and the linear fitting of the data.

Simplifications and limitations of the model

Because the system is presented as a Thevenin equivalent circuit, the dynamics of the system is neglected. In addition, the accuracy of the linearized model decreases when moving away from the area of the ohmic losses. Therefore, it can be stated that for a more precise analysis, a dynamic model should be used for the fuel cell plant.

2.2 DC/DC converter

According to the requirements set by the prototype plant, a literature survey was made. In the literature survey, the most promising isolated boost topologies were identified. The following topologies were simulated and small-scale (approx. 100 W) prototypes were built:

- flyback (Mohan et al., 2002),
- two-switch forward (Mohan et al., 2002),
- voltage-fed full-bridge (Mohan et al., 2002),
- current-fed full-bridge (Nymand and Andersen, 2008),
- active-clamped input current doubler–output voltage doubler (Kwon and Kwon, 2009), and
- resonant push-pull (RPP) (Kwon et al., 2009).

Based on the simulation results and the small-scale prototypes, the 10 kW full-scale prototypes were built from a current-fed full bridge with an active clamp and RPP topologies. Because of the good efficiency (approx. 95 % (Vaisanen et al., 2011)) and robustness of the full-scale prototype, the RPP converter was chosen.

The objectives of the converter modeling can be divided into three targets. The first, and the most important from the perspective of the control system, is to predict the low-frequency variations of the converter voltages and currents. These variations can be due to the line voltage, the duty cycle D, and the measurement noise. The second target is to be able to neglect the high-frequency switching ripple, and the third is to avoid the complicated switching harmonics and sidebands. An approach to reach these targets is to remove the switching harmonics by averaging all waveforms of the converter over one switching period.

In this section, the modeling of the RPP converter, with the previously described small-ripple approximation and the state-space averaging methods, is presented.

2.2.1 Resonant push-pull converter

The RPP converter provides a relatively simple boost topology to interface the SOFC. Properties that make the RPP a feasible choice for the SOFC usage are galvanic isolation, inherent boosting ability, and distinctively low switching frequency input current ripple caused by the boost inductor. The inherent boosting ability is desired because of the low output voltage of the SOFC. In addition, galvanic isolation helps to boost the voltage through the transformer and provides improved safety in the case of a malfunction. The applied RPP converter is presented in Fig. 2.5 and the parameters in Table 2.2.

To simplify the notations in the calculations, the following quantities are defined

$$R_{\mathrm{cre}} = 2R_{\mathrm{cr}} + R_{\mathrm{dc}}, \tag{2.16}$$

$$I_{\mathrm{cr}} = \frac{V_{\mathrm{cr1}} + V_{\mathrm{cr2}} - V_{\mathrm{dc}}}{R_{\mathrm{cr1}} + R_{\mathrm{cr2}} + R_{\mathrm{dc}}}, \tag{2.17}$$

$$I_{\mathrm{dc}} = I_{\mathrm{cr}} - I_{\mathrm{ac}}, \tag{2.18}$$

$$V_{\mathrm{cd}} = V_{\mathrm{dc}} - R_{\mathrm{dc}} I_{\mathrm{cr}} + R_{\mathrm{dc}} I_{\mathrm{ac}}, \tag{2.19}$$

$$V_{\mathrm{cc}} = \frac{V_{\mathrm{cc1}} + V_{\mathrm{cc2}}}{2}, \tag{2.20}$$

$$R'_{\mathrm{lk}} = R_{\mathrm{cr}} + R_{\mathrm{cc}} + R_{\mathrm{lk}}, \tag{2.21}$$

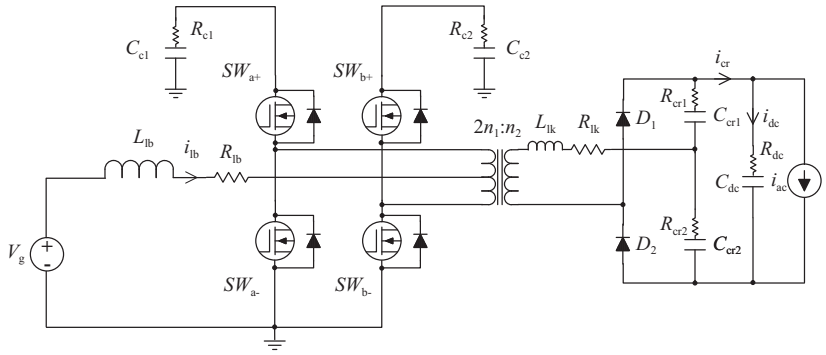

Figure 2.5. Simplified schematic of the RPP converter.

Table 2.2. Parameters of the applied RPP converter.

Parameter	Value	Description
P_{nom}	10 kW	Nominal power
V_{g}	50 V	Input voltage
L_{lb}	20 µH	Boost inductance
R_{lb}	0.47 mΩ	Series resistance of the L_{lb}
n_1	2	Primary turns of the transformer
n_2	12	Secondary turns of the transformer
F_{s}	50 kHz	Switching frequency
D	0.56	Duty cycle in the operating point
C_{c1}	80 µF	Snubber capacitor
C_{c2}	80 µF	Snubber capacitor
R_{c1}	5 mΩ	Series resistance of the snubber capacitor C_{c1}
R_{c2}	5 mΩ	Series resistance of the snubber capacitor C_{c2}
C_{cr1}	1320 nF	Resonance capacitor
C_{cr2}	1320 nF	Resonance capacitor
R_{cr1}	5 mΩ	Series resistance of the capacitor C_{cr1}
R_{cr2}	5 mΩ	Series resistance of the capacitor C_{cr2}
I_{ac}	15,2 A	Load current in the operating point
V_{dc}	660 V	DC link voltage in the operating point
C_{dc}	230 µF	DC link capacitor
R_{dc}	1.5 mΩ	Series resistance of the C_{dc}
R_{l}	43.6 Ω	Equivalent load resistance in the operating point $R_{\text{l}} = \frac{V_{\text{dc}}}{I_{\text{ac}}}$

$$D^* = (D-1), \tag{2.22}$$

and

$$D' = (1-D). \tag{2.23}$$

First, the operating periods of different modes have to be calculated. To simplify the converter, only two modes are analyzed, and it is assumed that the resonance period of the LC circuit of the converter, formed by the transformer leakage inductance and the resonant capacitors C_{cr1} and C_{cr2}, is equal to the switching period t_2. The resonance period can be defined as (Kwon et al., 2009)

$$\omega_{\mathrm{r}} = \frac{1}{\sqrt{L_{\mathrm{lk}} C_{\mathrm{cr}}}}, \tag{2.24}$$

where we can calculate the duration of the resonance period by

$$t_{\mathrm{r}} = 2\pi\sqrt{L_{\mathrm{lk}} C_{\mathrm{cr}}}, \tag{2.25}$$

where C_{cr} is the capacitance of the resonance capacitor.

After determining the resonance period, the operating periods can be defined as follows:

$$t_1 = t_4 = \begin{cases} (0.5-D)T_{\mathrm{s}}, & \text{when } D<0.5 \\ (D-0.5)T_{\mathrm{s}}, & \text{when } D\geq 0.5 \end{cases} \tag{2.26}$$

$$t_2 = t_5 = \frac{1}{2} t_{\mathrm{r}} = \pi\sqrt{L_{\mathrm{lk}} C_{\mathrm{cr}}} \tag{2.27}$$

$$t_3 = t_6 = \begin{cases} DT_{\mathrm{s}} - t_2, & \text{when } D<0.5 \\ D'T_{\mathrm{s}} - t_2, & \text{when } D\geq 0.5 \end{cases} \tag{2.28}$$

From Equations (2.26)–(2.28), we can see that the resonance condition

$$\frac{1}{2} t_{\mathrm{r}} \leq \begin{cases} DT_{\mathrm{s}}, & \text{when } D<0.5 \\ D'T_{\mathrm{s}}. & \text{when } D\geq 0.5 \end{cases} \tag{2.29}$$

must be satisfied, when operating the secondary diodes with the zero-current turn-off. It is pointed out that because of neglecting the periods t_3 and t_6, the model accuracy decreases as the operating point moves from the vicinity of the resonance condition. Because of the small-signal averaging and linearizing, this simplification can be assumed not to have a significant influence on the dynamics of the system.

Transformation ratio of the transformer can be defined as follows:

$$\mu = \begin{cases} \frac{n_1}{n_2}, & \text{when referred to a single winding} \\ \frac{2n_1}{n_2}, & \text{when referred to both windings} \end{cases} \tag{2.30}$$

Further, to simplify the analysis, the following assumptions are made:

- The operation of the converter is symmetrical, (i.e. t_1=t_4, t_2=t_5, and t_3=t_6)
- C_{c1}=C_{c2},
- C_{cr1}=C_{cr2},
- R_{cr}=R_{cr1}=R_{cr2}, and
- R_{cc}=R_{c1}=R_{c2}.

2.2.2 Large-signal model

To understand the dynamical behavior of DC/DC converters, a small-signal AC model is required for the analysis. Hence, a corresponding AC model for the RPP converter is derived in this section by applying the SSA (State Space Average) method by Middlebrook and Cuk (1977). Owing to the nature of the RPP converter, the analysis can be made in the CCM (Continuous Conduction Mode), while the DCM (Discontinuous Conduction Mode) can be neglected. The switching waveforms are not presented in this analysis, since the operating principle remains the same as presented in Kwon et al. (2009).

Because the operating mode changes at D=0.5, two separate models are needed to explain the behavior of the system. The change in the transformation ratio of the system (2.30) is observed with the coefficient 1/2, which makes it possible to use an explicitly defined transformation ratio μ. In this section, the dynamic models for $D \geq 0.5$ and $D < 0.5$ are introduced.

The SSA model is derived by the chosen differential state variables as follows:

$$L_{\mathrm{lb}} \frac{\mathrm{d}}{\mathrm{d}t} \langle I_{\mathrm{lb}} \rangle_{T_{\mathrm{s}}} = \langle V_{\mathrm{lb}} \rangle_{T_{\mathrm{s}}}, \tag{2.31}$$

$$C_{\mathrm{c1}} \frac{\mathrm{d}}{\mathrm{d}t} \langle V_{\mathrm{cc1}} \rangle_{T_{\mathrm{s}}} = \langle I_{\mathrm{cc1}} \rangle_{T_{\mathrm{s}}}, \tag{2.32}$$

$$C_{\mathrm{c2}} \frac{\mathrm{d}}{\mathrm{d}t} \langle V_{\mathrm{cc2}} \rangle_{T_{\mathrm{s}}} = \langle I_{\mathrm{cc2}} \rangle_{T_{\mathrm{s}}}, \tag{2.33}$$

$$L_{\mathrm{lk}} \frac{\mathrm{d}}{\mathrm{d}t} \langle I_{\mathrm{lk}} \rangle_{T_{\mathrm{s}}} = \langle V_{\mathrm{lk}} \rangle_{T_{\mathrm{s}}}, \tag{2.34}$$

$$C_{\mathrm{cr1}} \frac{\mathrm{d}}{\mathrm{d}t} \langle V_{\mathrm{cr1}} \rangle_{T_{\mathrm{s}}} = \langle I_{\mathrm{cr1}} \rangle_{T_{\mathrm{s}}}, \tag{2.35}$$

$$C_{\mathrm{cr2}} \frac{\mathrm{d}}{\mathrm{d}t} \langle V_{\mathrm{cr2}} \rangle_{T_{\mathrm{s}}} = \langle I_{\mathrm{cr2}} \rangle_{T_{\mathrm{s}}}, \text{ and} \tag{2.36}$$

$$C_{\mathrm{dc}} \frac{\mathrm{d}}{\mathrm{d}t} \langle V_{\mathrm{dc}} \rangle_{T_{\mathrm{s}}} = \langle i_{\mathrm{dc}} \rangle_{T_{\mathrm{s}}}, \tag{2.37}$$

where $\langle X \rangle_{T_{\mathrm{s}}}$ denotes an averaged value of the quantity X over the switching period T_{s}.

2.2.3 Boost mode

When operating at $D \geq 0.5$, the converter operates in the boost mode. This means that the h-bridge of the power state is switched in the short circuit during the operating states t_1 and t_4, and the boost inductor L_{lb} stores energy in the magnetic field and releases the energy during the states t_2 and t_3.

State 1

In the state t_1, the transistors $SW_{\mathrm{a-}}$ and $SW_{\mathrm{b-}}$ are conducting and the boost inductor L_{lb} is charging. The secondary resonance capacitors C_{cr1} and C_{cr2} are loading the output capacitor C_{dc}, which feeds the load

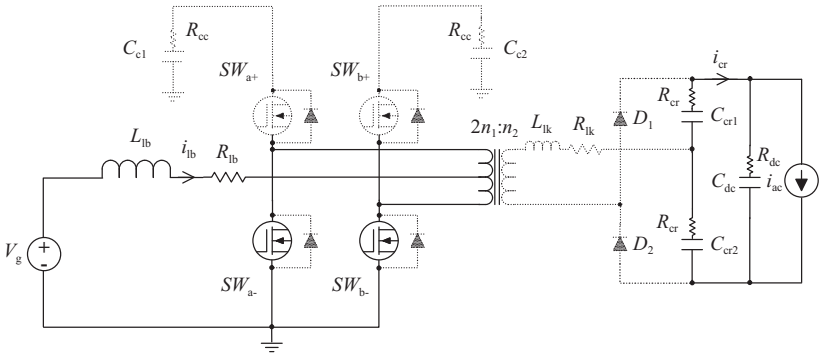

Figure 2.6. Operating mode t_1 when $D \geq 0.5$. The inactive parts of the circuit are indicated by dotted lines.

I_{ac}. The input current I_{lb} flows through the resistance R_{lb}, while the output current I_{dc} flows through the resistance R_{dc}.

The equivalent circuit diagram of the state t_1 is presented in Fig. 2.6, and the differential equations of the state can be defined as follows:

$$L_{lb}\frac{d}{dt}\langle I_{lb}\rangle_{T_s} = \langle V_g\rangle_{T_s} - R_{lb}\langle I_{lb}\rangle_{T_s} \tag{2.38}$$

$$C_{c1}\frac{d}{dt}\langle V_{cc1}\rangle_{T_s} = 0 \tag{2.39}$$

$$C_{c2}\frac{d}{dt}\langle V_{cc2}\rangle_{T_s} = 0 \tag{2.40}$$

$$L_{lk}\frac{d}{dt}\langle I_{lk}\rangle_{T_s} = 0 \tag{2.41}$$

$$C_{cr1}\frac{d}{dt}\langle V_{cr1}\rangle_{T_s} = -\langle I_{cr}\rangle_{T_s} \tag{2.42}$$

$$C_{cr2}\frac{d}{dt}\langle V_{cr2}\rangle_{T_s} = -\langle I_{cr}\rangle_{T_s} \tag{2.43}$$

$$C_{dc}\frac{d}{dt}\langle V_{dc}\rangle_{T_s} = \langle I_{cr}\rangle_{T_s} - I_{ac} \tag{2.44}$$

State 2

During the state t_2, the power is transferred from the primary to the secondary. The voltage over L_{lb} is the voltage difference between V_g and V_{cc2} with voltage losses caused by the resistors observed. The input current I_{lb} loads the capacitor C_{c2}, which feeds the capacitor C_{cr1} through the leakage inductance L_{lk}. The resonant capacitors C_{cr1} and C_{cr2} charge the DC link capacitor C_{dc}, which feeds the load I_{ac}.

The equivalent circuit diagram of the state t_2 is presented in Fig. 2.7, and the differential equations of the state can be defined as follows:

$$L_{lb}\frac{d}{dt}\langle I_{lb}\rangle_{T_s} = \langle V_g\rangle_{T_s} - (R_{lb}+R_{cc})\langle I_{lb}\rangle_{T_s} + R_{cc}\mu\langle I_{lk}\rangle_{T_s} - \frac{1}{2}\langle V_{cc2}\rangle_{T_s} \tag{2.45}$$

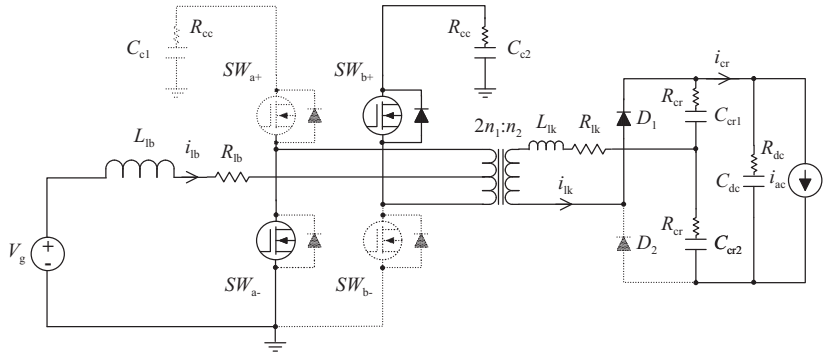

Figure 2.7. Operating mode $t_2$when $D\geq$0.5. The inactive parts of the circuit are indicated by dotted lines.

$$C_{c1}\frac{d}{dt}\langle V_{cc1}\rangle_{T_s} = 0 \tag{2.46}$$

$$C_{c2}\frac{d}{dt}\langle V_{cc2}\rangle_{T_s} = \frac{1}{2}\langle I_{lb}\rangle_{T_s} - \mu\langle I_{lk}\rangle_{T_s} \tag{2.47}$$

$$L_{lk}\frac{d}{dt}\langle I_{lk}\rangle_{T_s} = \frac{\mu}{2}V_{cc2} + \frac{R_{cc}}{\mu}\langle I_{lb}\rangle_{T_s} - (R_{cc}+R_{lk}+R_{cr})\langle I_{lk}\rangle_{T_s} + R_{cr}\langle I_{cr}\rangle_{T_s} - \langle V_{cr1}\rangle_{T_s} \tag{2.48}$$

$$C_{cr1}\frac{d}{dt}\langle V_{cr1}\rangle_{T_s} = \langle I_{lk}\rangle_{T_s} - \langle I_{cr}\rangle_{T_s} \tag{2.49}$$

$$C_{cr2}\frac{d}{dt}\langle V_{cr2}\rangle_{T_s} = -\langle I_{cr}\rangle_{T_s} \tag{2.50}$$

$$C_{dc}\frac{d}{dt}\langle V_{dc}\rangle_{T_s} = \langle I_{cr}\rangle_{T_s} - I_{ac} \tag{2.51}$$

States 4–5

The states t_4–t_6 correspond to the states t_1–t_3 with the only difference that V_{cc1} and V_{cc2}, similarly as V_{cr1} and V_{cr2} , are opposite when compared with the first states. For space saving purposes, the state equations for the states t_4–t_5 are not presented.

2.2.4 Non-overlapping mode

When operating at D<0.5, the transistors SW_{a-} and SW_{b-} do not overlap, and boosting does not occur. The state equations of the non-overlapping region are presented in the following.

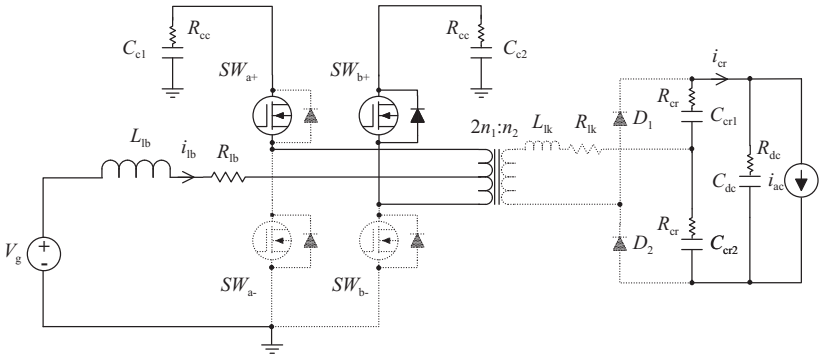

Figure 2.8. Operating mode $t_1$when D<0.5. The inactive parts of the circuit are indicated by dotted lines.

State 1

The equivalent circuit diagram of the state t_1 is presented in Fig. 2.8, and the differential equations of the state can be defined as follows:

$$L_{\mathrm{lb}}\frac{\mathrm{d}}{\mathrm{d}t}\langle I_{\mathrm{lb}}\rangle_{T_\mathrm{s}} = \langle V_\mathrm{g}\rangle_{T_\mathrm{s}} - (R_{\mathrm{lb}}+R_{\mathrm{cc}})\langle I_{\mathrm{lb}}\rangle_{T_\mathrm{s}} - \langle V_{\mathrm{cc}}\rangle_{T_\mathrm{s}} \tag{2.52}$$

$$C_{\mathrm{c1}}\frac{\mathrm{d}}{\mathrm{d}t}\langle V_{\mathrm{cc1}}\rangle_{T_\mathrm{s}} = \frac{1}{2}\langle I_{\mathrm{lb}}\rangle_{T_\mathrm{s}} \tag{2.53}$$

$$C_{\mathrm{c2}}\frac{\mathrm{d}}{\mathrm{d}t}\langle V_{\mathrm{cc2}}\rangle_{T_\mathrm{s}} = \frac{1}{2}\langle I_{\mathrm{lb}}\rangle_{T_\mathrm{s}} \tag{2.54}$$

$$L_{\mathrm{lk}}\frac{\mathrm{d}}{\mathrm{d}t}\langle I_{\mathrm{lk}}\rangle_{T_\mathrm{s}} = 0 \tag{2.55}$$

$$C_{\mathrm{cr1}}\frac{\mathrm{d}}{\mathrm{d}t}\langle V_{\mathrm{cr1}}\rangle_{T_\mathrm{s}} = -\langle I_{\mathrm{cr}}\rangle_{T_\mathrm{s}} \tag{2.56}$$

$$C_{\mathrm{cr2}}\frac{\mathrm{d}}{\mathrm{d}t}\langle V_{\mathrm{cr2}}\rangle_{T_\mathrm{s}} = -\langle I_{\mathrm{cr}}\rangle_{T_\mathrm{s}} \tag{2.57}$$

$$C_{\mathrm{dc}}\frac{\mathrm{d}}{\mathrm{d}t}\langle V_{\mathrm{dc}}\rangle_{T_\mathrm{s}} = \langle I_{\mathrm{cr}}\rangle_{T_\mathrm{s}} - I_{\mathrm{ac}} \tag{2.58}$$

State 2

When operating at D<0.5, the state t_2 is identical to the state t_2 when operating at $D\geq$0.5. To make it easier to follow the modeling procedure, the state equations are rewritten.

The equivalent circuit diagram of the state t_2 is presented in Fig. 2.9, and the differential equations of the state can be defined as follows:

$$L_{\mathrm{lb}}\frac{\mathrm{d}}{\mathrm{d}t}\langle I_{\mathrm{lb}}\rangle_{T_\mathrm{s}} = \langle V_\mathrm{g}\rangle_{T_\mathrm{s}} - \langle I_{\mathrm{lb}}\rangle_{T_\mathrm{s}}(R_{\mathrm{lb}}+R_{\mathrm{cc}}) + \mu\langle I_{\mathrm{lk}}\rangle_{T_\mathrm{s}}R_{\mathrm{cc}} - \frac{1}{2}\langle V_{\mathrm{cc2}}\rangle_{T_\mathrm{s}} \tag{2.59}$$

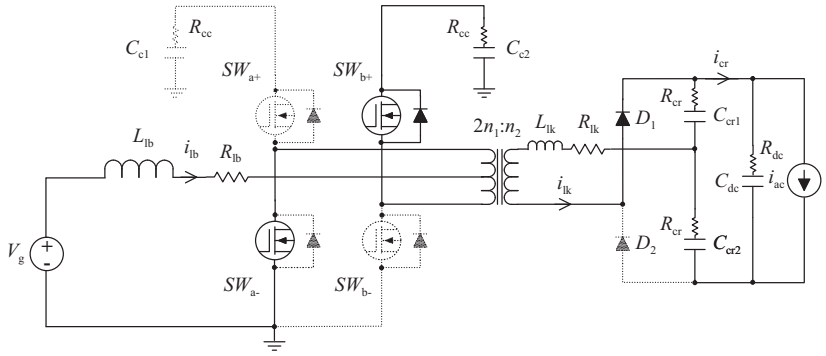

Figure 2.9. Operating mode $t_2$when D<0.5. The inactive parts of the circuit are indicated by dotted lines.

$$C_{c1}\frac{d}{dt}\langle V_{cc1}\rangle_{T_s} = 0 \tag{2.60}$$

$$C_{c2}\frac{d}{dt}\langle V_{cc2}\rangle_{T_s} = \frac{1}{2}\langle I_{lb}\rangle_{T_s} - \mu\langle I_{lk}\rangle T_s \tag{2.61}$$

$$L_{lk}\frac{d}{dt}\langle I_{lk}\rangle_{T_s} = \frac{\mu}{2}V_{cc2} + \frac{R_{cc}}{\mu}\langle I_{lb}\rangle_{T_s} - (R_{cc}+R_{lk}+R_{cr})\langle I_{lk}\rangle_{T_s} + R_{cr}\langle I_{cr}\rangle_{T_s} - \langle V_{cr1}\rangle_{T_s} \tag{2.62}$$

$$C_{cr1}\frac{d}{dt}\langle V_{cr1}\rangle_{T_s} = I_{lk} - I_{cr} \tag{2.63}$$

$$C_{cr2}\frac{d}{dt}\langle V_{cr2}\rangle_{T_s} = -I_{cr} \tag{2.64}$$

$$C_{dc}\frac{d}{dt}\langle V_{dc}\rangle_{T_s} = I_{cr} - I_{ac} \tag{2.65}$$

2.2.5 Small-signal model

The averaged system, which can be constructed from the differential equations by calculating a weighted average over the switching period T_s, is nonlinear and can be linearized by calculating the Jacobian matrix in a certain operating point as presented. By calculating the linearized set of equations formed by the Jacobian matrix, we obtain an LTI SSA model. The linearized model can be presented in the state-space by

$$\mathbf{K}\frac{d}{dt}\tilde{\mathbf{x}} = \tilde{\mathbf{A}}\tilde{\mathbf{x}} + \tilde{\mathbf{B}}\tilde{\mathbf{u}} \tag{2.66}$$

$$\tilde{\mathbf{y}} = \tilde{\mathbf{C}}\tilde{\mathbf{x}} + \tilde{\mathbf{D}}\tilde{\mathbf{u}} \tag{2.67}$$

Both the models share the matrices (2.73), (2.74), (2.75), and (2.76). When operating at $D\geq$0.5, the matrices $\tilde{\mathbf{A}}_{D\geq 0.5}$ (2.69) and $\tilde{\mathbf{B}}_{D\geq 0.5}$ (2.70) define the model. However, when operating at D<0.5, the matrices $\tilde{\mathbf{A}}_{D<0.5}$ (2.71) and $\tilde{\mathbf{B}}_{D<0.5}$ (2.72) define the model. We can also see that the rank of the model is five, although the system has seven states. It can be noticed that the states of C_{c1} and C_{c2} , and C_{cr1} and C_{cr2} can be combined. With this reduction, the rank of the model corresponds to the states of the system.

$$\mathbf{K} = \begin{bmatrix} L_{\mathrm{lb}} & 0 & 0 & 0 & 0 & 0 & 0 \\ 0 & C_{\mathrm{c1}} & 0 & 0 & 0 & 0 & 0 \\ 0 & 0 & C_{\mathrm{c2}} & 0 & 0 & 0 & 0 \\ 0 & 0 & 0 & L_{\mathrm{lk}} & 0 & 0 & 0 \\ 0 & 0 & 0 & 0 & C_{\mathrm{cr1}} & 0 & 0 \\ 0 & 0 & 0 & 0 & 0 & C_{\mathrm{cr2}} & 0 \\ 0 & 0 & 0 & 0 & 0 & 0 & C_{\mathrm{dc}} \end{bmatrix} \tag{2.68}$$

$$\tilde{\mathbf{A}}_{D\geq 0.5} = \begin{bmatrix} 2R_{\mathrm{cc}}D^* - R_{\mathrm{lb}} & \frac{D^*}{2} & \frac{D^*}{2} & -2R_{\mathrm{cc}}D^*\mu & 0 & 0 & 0 \\ \frac{D'}{2} & 0 & 0 & \mu D^* & 0 & 0 & 0 \\ \frac{D'}{2} & 0 & 0 & \mu D^* & 0 & 0 & 0 \\ -\frac{2R_{\mathrm{cc}}D^*}{\mu} & -\mu D^* & -\mu D^* & 2D^*R'_{\mathrm{lk}} & a_1 & a_1 & \frac{2R_{\mathrm{cr}}D^*}{R_{\mathrm{cre}}} \\ 0 & 0 & 0 & D' & -a_2 & -a_2 & a_2 \\ 0 & 0 & 0 & D' & -a_2 & -a_2 & a_2 \\ 0 & 0 & 0 & 0 & a_2 & a_2 & -a_2 - \frac{1}{R_{\mathrm{l}}} \end{bmatrix} \tag{2.69}$$

$$\tilde{\mathbf{B}}_{D\geq 0.5} = \begin{bmatrix} 1 & 0 & \frac{V_{\mathrm{cc1}}+V_{\mathrm{cc2}}}{2} + 2I_{\mathrm{lb}}R_{\mathrm{cc}} - 2I_{\mathrm{lk}}R_{\mathrm{cc}}\mu \\ 0 & 0 & I_{\mathrm{lk}}\mu - \frac{I_{\mathrm{lb}}}{2} \\ 0 & 0 & I_{\mathrm{lk}}\mu - \frac{I_{\mathrm{lb}}}{2} \\ 0 & 0 & b_1 \\ 0 & 0 & -I_{\mathrm{lk}} \\ 0 & 0 & -I_{\mathrm{lk}} \\ 0 & -1 & 0 \end{bmatrix} \tag{2.70}$$

$$\tilde{\mathbf{A}}_{D<0.5} = \begin{bmatrix} -R_{\mathrm{cc}} - R_{\mathrm{lb}} & \frac{D^*}{2} & \frac{D^*}{2} & 2DR_{\mathrm{cc}}\mu & 0 & 0 & 0 \\ \frac{D'}{2} & 0 & 0 & -D\mu & 0 & 0 & 0 \\ \frac{D'}{2} & 0 & 0 & -D\mu & 0 & 0 & 0 \\ \frac{2DR_{\mathrm{cc}}}{\mu} & D\mu & D\mu & -2DR'_{\mathrm{lk}} & a_1 & a_1 & -\frac{2DR_{\mathrm{cr}}}{R_{\mathrm{cre}}} \\ 0 & 0 & 0 & D & -a_2 & -a_2 & a_2 \\ 0 & 0 & 0 & D & -a_2 & -a_2 & a_2 \\ 0 & 0 & 0 & 0 & a_2 & a_2 & -a_2 - \frac{1}{R_{\mathrm{l}}} \end{bmatrix} \tag{2.71}$$

$$\tilde{\mathbf{B}}_{D<0.5} = \begin{bmatrix} 1 & 0 & \frac{V_{\mathrm{cc1}}+V_{\mathrm{cc2}}}{2} + 2I_{\mathrm{lk}}R_{\mathrm{cc}}\mu \\ 0 & 0 & -\frac{I_{\mathrm{lb}}}{2} - I_{\mathrm{lk}}\mu \\ 0 & 0 & -\frac{I_{\mathrm{lb}}}{2} - I_{\mathrm{lk}}\mu \\ 0 & 0 & b_2 \\ 0 & 0 & I_{\mathrm{lk}} \\ 0 & 0 & I_{\mathrm{lk}} \\ 0 & -1 & 0 \end{bmatrix} \tag{2.72}$$

$$\tilde{\mathbf{C}} = \begin{bmatrix} 1 & 0 & 0 & 0 & 0 & 0 & 0 \\ 0 & 0 & 0 & 0 & 0 & 0 & 1 \end{bmatrix} \tag{2.73}$$

$$\tilde{\mathbf{D}} = \begin{bmatrix} 0 & 0 \\ 0 & 0 \end{bmatrix} \tag{2.74}$$

$$\tilde{\mathbf{x}} = \begin{bmatrix} \tilde{i}_{\mathrm{lb}} & \tilde{v}_{\mathrm{cc1}} & \tilde{v}_{\mathrm{cc2}} & \tilde{i}_{\mathrm{lk}} & \tilde{v}_{\mathrm{cr1}} & \tilde{v}_{\mathrm{cr2}} & \tilde{v}_{\mathrm{dc}} \end{bmatrix}^{\mathrm{T}} \tag{2.75}$$

$$\tilde{\mathbf{u}} = \begin{bmatrix} \tilde{v}_{\mathrm{g}} & \tilde{i}_{\mathrm{ac}} & \tilde{d} \end{bmatrix}^{\mathrm{T}} \tag{2.76}$$

where

$$a_1 = -\frac{D^*(2R_{\mathrm{cr}} - R_{\mathrm{cre}})}{R_{\mathrm{cre}}}, \tag{2.77}$$

$$a_2 = \frac{1}{R_{\mathrm{cre}}}, \tag{2.78}$$

$$\begin{aligned} b_1 = {} & V_{\mathrm{cr1}} + V_{\mathrm{cr2}} - V_{\mathrm{cc1}}\mu - V_{\mathrm{cc2}}\mu - 2I_{\mathrm{lk}}R_{\mathrm{cc}} + \\ & 2I_{\mathrm{lk}}R_{\mathrm{cr}} + 2I_{\mathrm{lk}}R_{\mathrm{lk}} - \frac{2R_{\mathrm{cr}}(V_{\mathrm{cr1}} + V_{\mathrm{cr2}} - V_{\mathrm{dc}})}{R_{\mathrm{cre}}} + \frac{(2I_{\mathrm{lb}}R_{\mathrm{cc}})}{\mu}, \end{aligned} \tag{2.79}$$

$$\begin{aligned} b_2 = {} & V_{\mathrm{cc1}}\mu - V_{\mathrm{cr2}} - V_{\mathrm{cr1}} + V_{\mathrm{cc2}}\mu + 2I_{\mathrm{lk}}R_{\mathrm{cc}} - \\ & 2I_{\mathrm{lk}}R_{\mathrm{cr}} - 2I_{\mathrm{lk}}R_{\mathrm{lk}} + \frac{2R_{\mathrm{cr}}(V_{\mathrm{cr1}} + V_{\mathrm{cr2}} - V_{\mathrm{dc}})}{R_{\mathrm{cre}}} - \frac{2I_{\mathrm{lb}}R_{\mathrm{cc}})}{\mu}, \end{aligned} \tag{2.80}$$

and

$$\tilde{\mathbf{y}} = \begin{bmatrix} \tilde{i}_{\mathrm{lb}} \\ \tilde{v}_{\mathrm{dc}} \end{bmatrix}. \tag{2.81}$$

2.2.6 Frequency responses

In the following, the frequency responses of the RPP converter in the linearization point are presented. The frequency responses of the open-loop transfer function can be used to verify the model against the measurements, to design an EMI (Electromagnetic Interference) filter without interference caused by the converter, to design a control system for the converter, and to analyze how the disturbances affect the system. All frequency responses represent the behavior in the linearization point.

Figure 2.10 presents the calculated frequency response of the transfer function $\frac{\tilde{i}_{\mathrm{lb}}(s)}{\tilde{d}(s)}$. The Bode diagram presents the open-loop transfer function from the duty cycle to the input current. This open-loop transfer function determines the control design of the system when the current control is applied.

Figure 2.11 illustrates the calculated frequency response of the transfer function $\frac{\tilde{v}_{\mathrm{dc}}(s)}{\tilde{d}(s)}$. The Bode diagram shows how much the variations in the duty cycle change the DC link voltage. In a voltage regulator

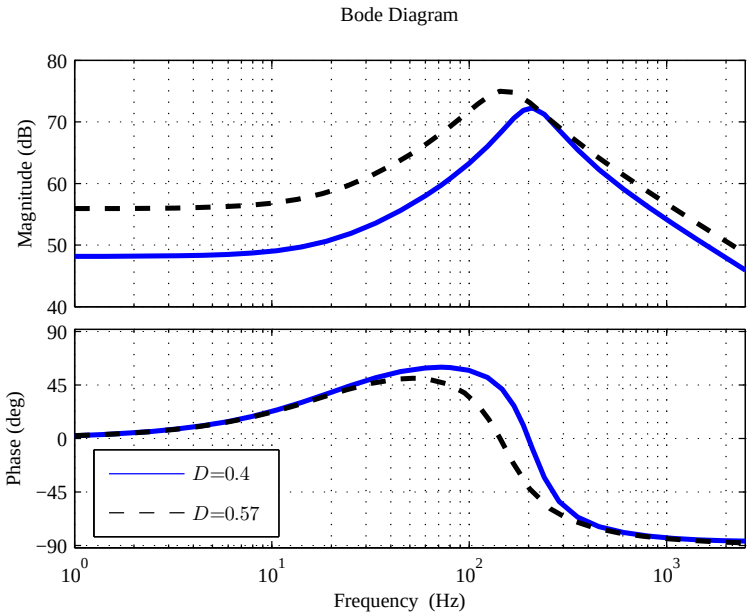

Figure 2.10. Calculated frequency responses from $\tilde{d}(s)$ to $\tilde{i}_{\mathrm{lb}}(s)$.

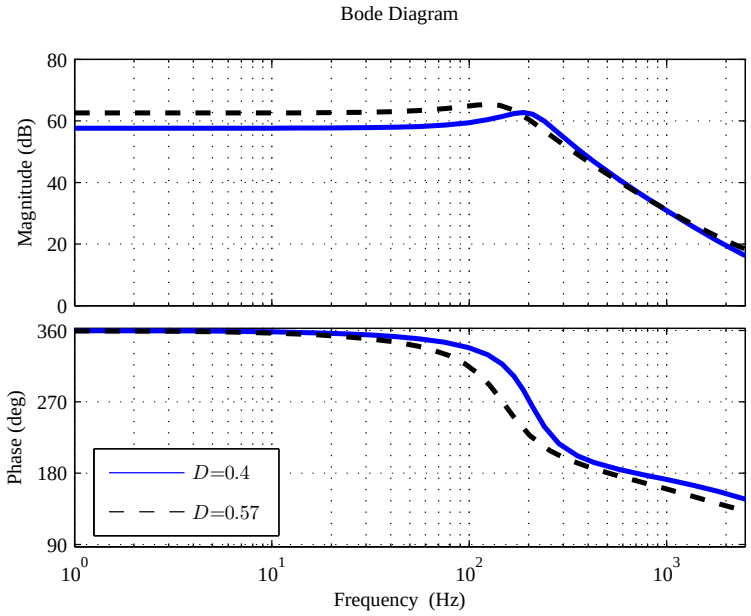

Figure 2.11. Calculated frequency responses from the $\tilde{d}(s)$ to $\tilde{v}_{\mathrm{dc}}(s)$.

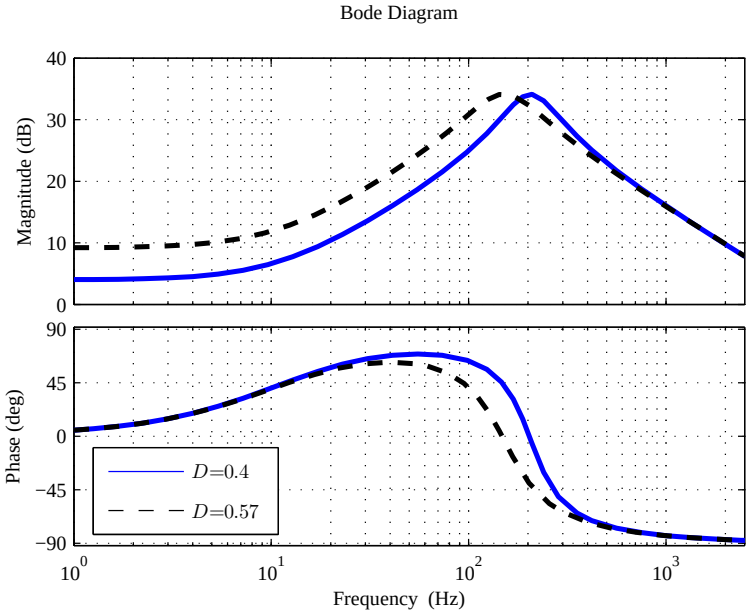

Figure 2.12. Calculated frequency responses from $\tilde{v}_g(s)$ to $\tilde{i}_{lb}(s)$.

system, this is a key component in the design of a suitable controller. However, in a current-controlled system this is not interesting if voltage regulation is not implemented in the DC/DC stage.

Figure 2.12 depicts the calculated frequency response of the transfer function $\frac{\tilde{i}_{lb}(s)}{\tilde{v}_g(s)}$. The Bode diagram shows how the variations in the input voltage affect the input current. This is also known as the converter input admittance.

Figure 2.13 presents the calculated frequency response of the transfer function $\frac{\tilde{v}_{dc}(s)}{\tilde{v}_g(s)}$. The Bode diagram illustrates how the input voltage variations affect the output voltage.

Figure 2.14 shows the calculated frequency response of the transfer function $\frac{\tilde{i}_{lb}(s)}{\tilde{i}_{ac}(s)}$. The Bode diagram demonstrates how the DC link current variations affect the input current. This frequency response is important when operating with a SOFC because of its lack of tolerance to the low-frequency current ripple.

2.2.7 Analysis

Because the system is linearized in a certain operating point, it is important to examine how the system dynamics is changed when the linearization point changes. In the following, the linearization point is varied from D=0.1 to D=0.7, and the responses are compared.

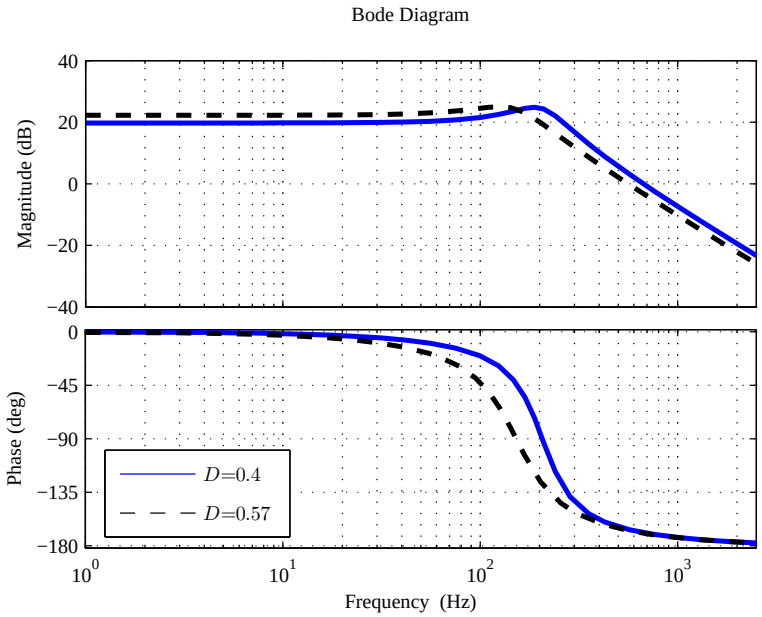

Figure 2.13. Calculated frequency responses from $\tilde{v}_g(s)$ to $\tilde{v}_{dc}(s)$.

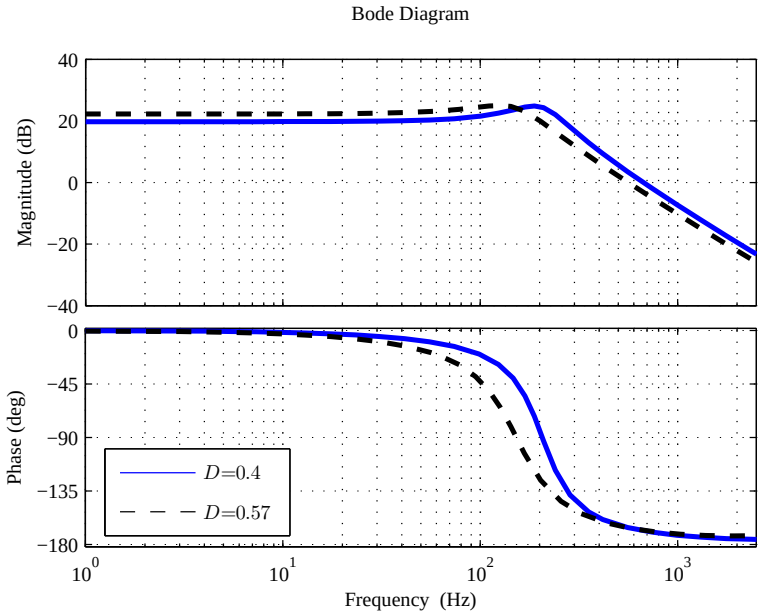

Figure 2.14. Calculated frequency responses from $\tilde{i}_{ac}(s)$ to $\tilde{i}_{lb}(s)$.

Figure 2.15 shows that when the duty cycle is increased, also the gain increases. Moreover, it can be noticed that the resonance frequency and the *Q*-value (Erickson and Maksimovic, 2001) of the system decrease when *D* increases. When designing a control system for the converter, it must be noticed that the system gain increases almost by 30 dB in D=0.7 compared with D=0.1. This gain directly affects the stability of the system, and the system must therefore be verified at the upper limit of the allowed *D*. If the grid harmonics are taken into account, we can see that at low *D* values the adequate mitigation should be ensured.

Again, from Fig. 2.16 we can see that the gain of the input current from the input voltage increases when *D* increases. Because the variation in the SOFC output voltage is slow compared with the response times of the converter, this is not a significant issue.

Figure 2.17 shows that the gain of I_{lb} from the load DC link load increases when the *D* increases. However, the magnitude of the frequency response is smaller than the magnitude of the frequency response in Fig. 2.15. In other words, the gain of the control to the input current is larger in magnitude than the disturbance.

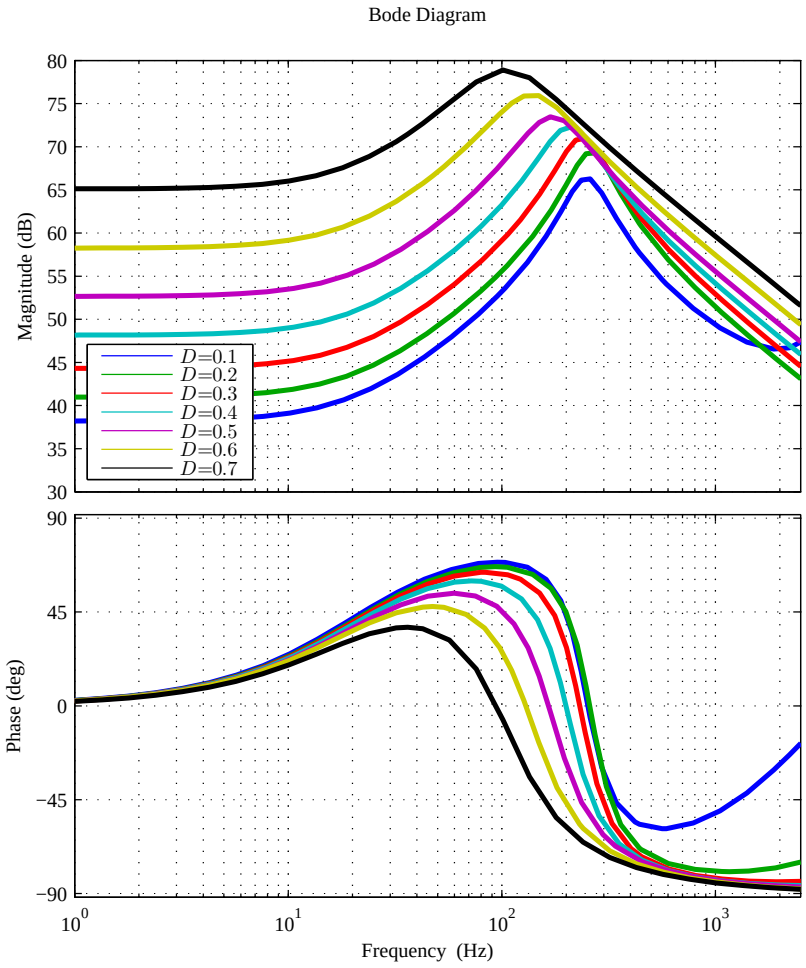

Figure 2.15. Simulated frequency responses from $\tilde{d}(s)$ to $\tilde{i}_{\mathrm{lb}}(s)$, $D = [0.1\text{–}0.7]$.

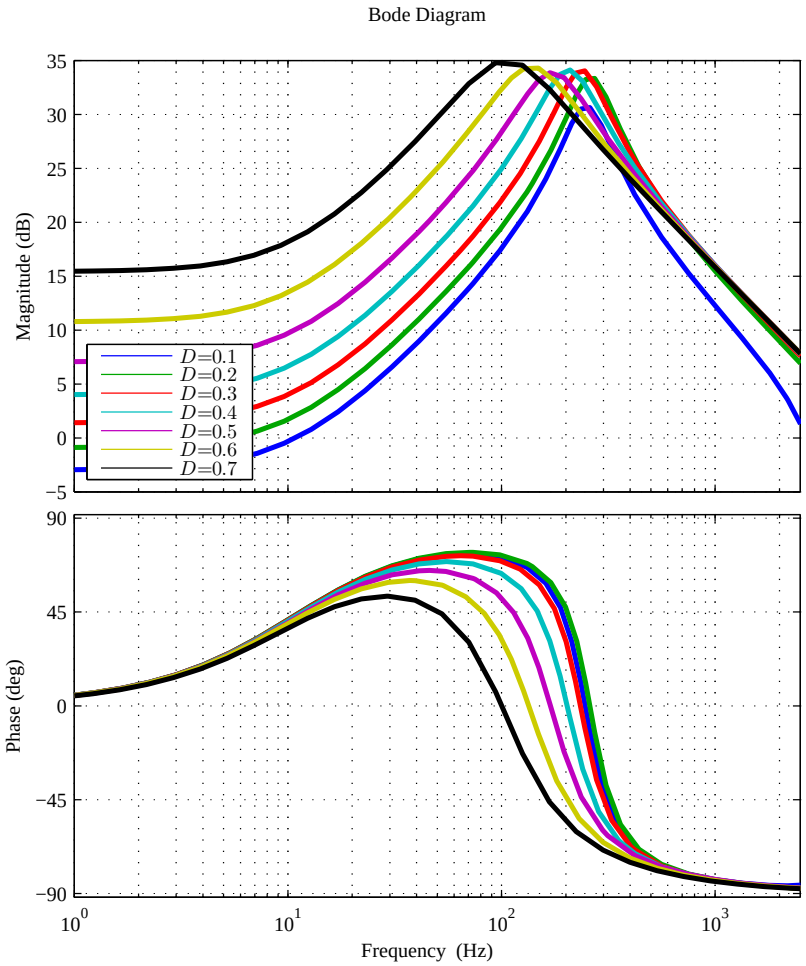

Figure 2.16. Simulated frequency responses from $\tilde{v}_{\mathrm{g}}(s)$ to $\tilde{i}_{\mathrm{lb}}(s)$, $D = [0.1\text{–}0.7]$.

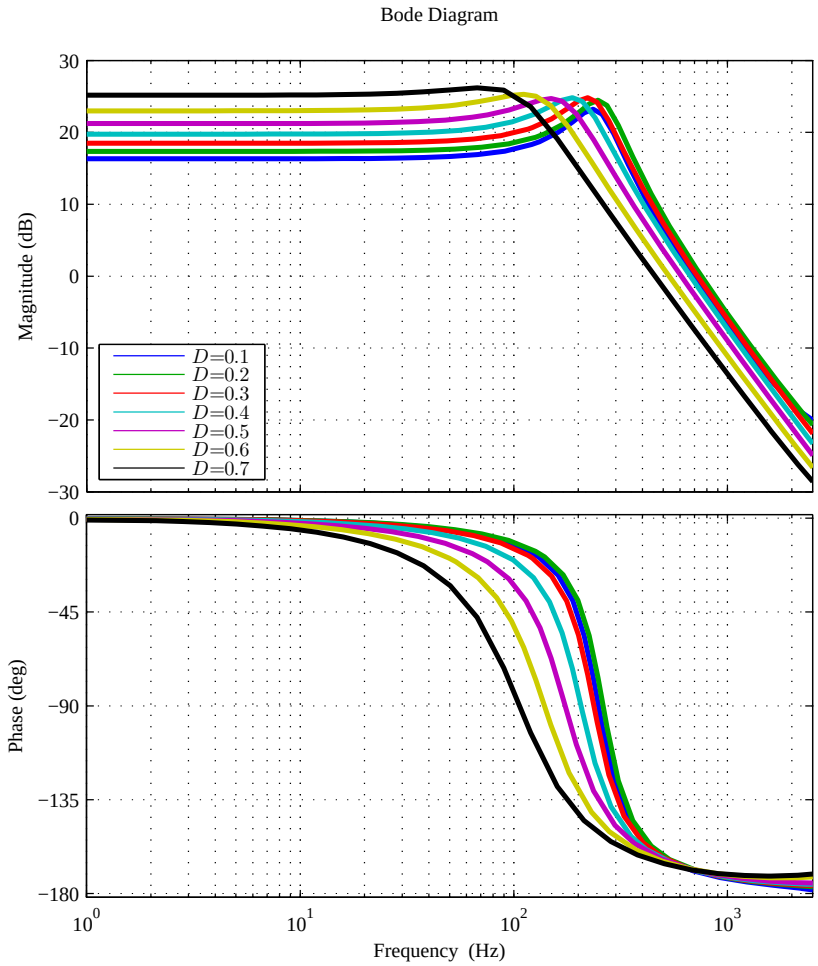

Figure 2.17. Simulated frequency responses from $\tilde{i}_{\mathrm{ac}}(s)$ to $\tilde{i}_{\mathrm{lb}}(s)$, $D = [0.1\text{–}0.7]$.

2.3 Grid converter

The grid converter is modeled and implemented, because the total dynamics of the PCU arises from the dynamics of the DC/DC converter, the grid converter, and the interaction between the converters. In this section, the model of the three-phase VSI is presented.

2.3.1 Voltage-source inverter

The modeling process of the VSI follows the state-space modeling procedure. In this prototype, an LC filter is used as the grid filter. The reason to prefer an LC filter to L- or LCL filters is practical; an L-filter with similar characteristics would be too bulky, and a suitable LCL filter was not available at the moment.

However, an LC filter can be treated as an LCL filter, where the grid-side L is the inductance formed by the grid and/or the distribution transformer. A schematic of the three-phase VSI with the grid-side inductance is presented in Fig. 2.18, where the variables are defined as follows

$$\mathbf{L_1} = \begin{bmatrix} L_{1,\mathrm{a}} & L_{1,\mathrm{b}} & L_{1,\mathrm{c}} \end{bmatrix}^{\mathrm{T}} \tag{2.82a}$$

$$\mathbf{R}_{\mathrm{L1}} = \begin{bmatrix} R_{\mathrm{L1,a}} & R_{\mathrm{L1,b}} & R_{\mathrm{L1,c}} \end{bmatrix}^{\mathrm{T}} \tag{2.82b}$$

$$\mathbf{L_2} = \begin{bmatrix} L_{2,\mathrm{a}} & L_{2,\mathrm{b}} & L_{2,\mathrm{c}} \end{bmatrix}^{\mathrm{T}} \tag{2.82c}$$

$$\mathbf{R}_{\mathrm{L2}} = \begin{bmatrix} R_{\mathrm{L2,a}} & R_{\mathrm{L2,b}} & R_{\mathrm{L2,c}} \end{bmatrix}^{\mathrm{T}} \tag{2.82d}$$

$$\mathbf{C}_{\mathrm{c}} = \begin{bmatrix} C_{\mathrm{c,a}} & C_{\mathrm{c,b}} & C_{\mathrm{c,c}} \end{bmatrix}^{\mathrm{T}} \tag{2.82e}$$

$$\mathbf{R}_{\mathrm{c}} = \begin{bmatrix} R_{\mathrm{c,a}} & R_{\mathrm{c,b}} & R_{\mathrm{c,c}} \end{bmatrix}^{\mathrm{T}} \tag{2.82f}$$

Because the grid-side L_2 is unknown, a reasonable value for the grid inductance must be approximated. The low-voltage distributed generation systems are usually connected to the distribution transformer. The distance between the fuel cell plant and the distribution transformer affects the equivalent inductance seen by the inverter. Thus, the grid-side inductance is formed by the cable inductance and the distribution

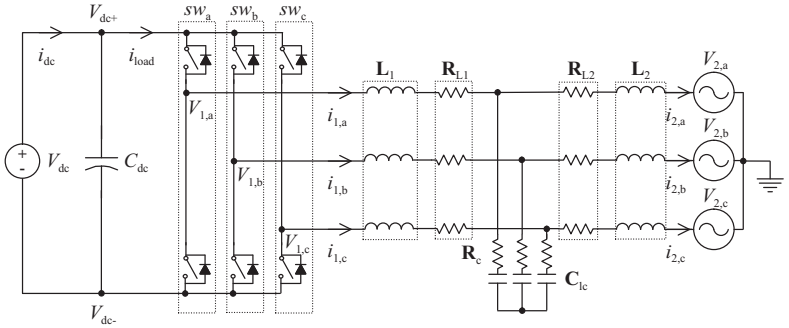

Figure 2.18. Schematic of the three-phase VSI with the LC grid filter and the grid impedance.

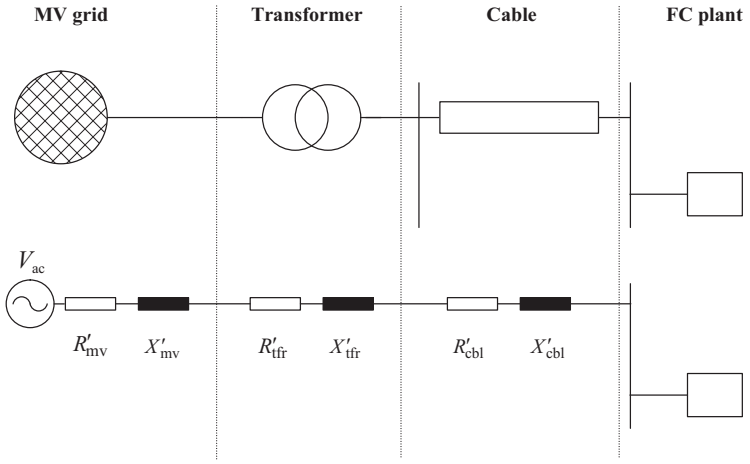

Figure 2.19. Grid equivalent circuit diagram.

Table 2.3. Typical line parameters (Engler and Soultanis, 2005).

Type of line	R' $\left[\frac{\Omega}{\text{km}}\right]$	X' $\left[\frac{\Omega}{\text{km}}\right]$	I_N [A]	$\frac{R'}{X'}$
low-voltage line	0.642	0.083	142	7.7
medium-voltage line	0.161	0.190	396	0.85
high-voltage line	0.06	0.191	580	0.31

transformer inductance, and the grid-side inductance for the LCL filter can be calculated by lumping the equivalent inductances and resistances. The equivalent grid diagram is presented in Fig. 2.19.

The inductance formed by the cables of the grid can be estimated by the average distance and the cable inductance per kilometer between the distributed resource and the distribution transformer. The typical line parameters are presented in Table 2.3. If the distance between the grid filter and the distribution transformer is approximated to 500 meters, the parameters for the cable inductance and resistance become R'_{cbl}=0.321 Ω and L'_{cbl}=0.132 mH.

The parameters for the distribution transformer can be calculated from the datasheet of the transformer. Because the exact model of the transformer cannot be known, an approximation based on a suitable model is made. An ABB CTO2000/20.5-vok distribution transformer is used in these calculations to simulate a general case for low-voltage distributed generation. The effect of the grid-side inductance will be analyzed later. If the short-circuit impedance is assumed purely inductive, the parameters for the distribution transformer are R'_{tfr}=0 Ω and L'_{tfr}=0.102 mH. The approximation of the cable inductance and the transformer inductance is assumed to be accurate enough. The parameters of the three-phase VSI and the grid-side inductance used in this doctoral thesis are presented in Table 2.4.

Table 2.4. Parameters of the three-phase VSI.

Variable	Parameter	Variable	Parameter
L_1	3.5 mH	R_C	0 Ω
C_{lc}	1.5 uF	$F_{sw,ac}$	5 kHz
V_{dc}	660 V	C_{dc}	230 μF
R_{L1}	0.44 Ω	L_2	0.234 mH
V_{grid}	230/400V	R_{L2}	0.321 Ω

2.3.2 Modeling

A single-phase VSI equivalent circuit with an LC filter and a grid impedance can be presented with the following equations

$$L_1 \frac{\mathrm{d}}{\mathrm{d}t} i_1 = v_1 - (R_C + R_{L1}) i_1 + R_C i_2 - v_C, \tag{2.83a}$$

$$L_2 \frac{\mathrm{d}}{\mathrm{d}t} i_2 = v_C + R_C i_1 - (R_C + R_{L2}) i_2 - v_2, \tag{2.83b}$$

$$C_{lc} \frac{\mathrm{d}}{\mathrm{d}t} v_C = i_c = i_1 - i_2, \tag{2.83c}$$

where L_1 is the converter-side inductance, i_1 is the converter-side current, v_1 is the converter-side voltage, R_C is the ESR (Equivalent Series Resistance) of the capacitor C_{lc}, $R_{L1}$is the series resistance of the L_1, L_2 is the grid-side inductance, R_{L2} is the series resistance of the L_2, i_2 is the grid-side current, and v_2 is the grid voltage.

The single-phase system can be extended to a three-phase system with the state equations in *abc* coordinates, where the subscripts a, b, and c denote the phase. When the grid filter and the grid parameters are assumed symmetrical, the state equations can be written as

$$L_1 \frac{\mathrm{d}}{\mathrm{d}t} \begin{bmatrix} i_{1,a} \\ i_{1,b} \\ i_{1,c} \end{bmatrix} = \begin{bmatrix} v_{1,a} \\ v_{1,b} \\ v_{1,c} \end{bmatrix} - (R_C + R_{L1}) \begin{bmatrix} i_{1,a} \\ i_{1,b} \\ i_{1,c} \end{bmatrix} + R_C \begin{bmatrix} i_{2,a} \\ i_{2,b} \\ i_{2,c} \end{bmatrix} - \begin{bmatrix} v_{C,a} \\ v_{C,b} \\ v_{C,c} \end{bmatrix} \tag{2.84a}$$

$$L_2 \frac{\mathrm{d}}{\mathrm{d}t} \begin{bmatrix} i_{2,a} \\ i_{2,b} \\ i_{2,c} \end{bmatrix} = \begin{bmatrix} v_{C,a} \\ v_{C,b} \\ v_{C,c} \end{bmatrix} + R_C \begin{bmatrix} i_{1,a} \\ i_{1,b} \\ i_{1,c} \end{bmatrix} - (R_C + R_{L2}) \begin{bmatrix} i_{2,a} \\ i_{2,b} \\ i_{2,c} \end{bmatrix} - \begin{bmatrix} v_{2,a} \\ v_{2,b} \\ v_{2,c} \end{bmatrix} \tag{2.84b}$$

$$C_{lc} \frac{\mathrm{d}}{\mathrm{d}t} \begin{bmatrix} v_{C,a} \\ v_{C,b} \\ v_{C,c} \end{bmatrix} = \begin{bmatrix} i_{1,a} \\ i_{1,b} \\ i_{1,c} \end{bmatrix} - \begin{bmatrix} i_{2,a} \\ i_{2,b} \\ i_{2,c} \end{bmatrix} \tag{2.84c}$$

Equations in (2.84) can be transformed into the stationary $\alpha\beta$ domain. The system equations in the $\alpha\beta$ domain can be written as

$$L_1 \frac{\mathrm{d}}{\mathrm{d}t} \mathbf{i}_{1,\alpha\beta} = \mathbf{v}_{1,\alpha\beta} - \mathbf{v}_{C,\alpha\beta} - (R_C + R_{L1}) \mathbf{i}_{1,\alpha\beta} + R_C \mathbf{i}_{2,\alpha\beta} \tag{2.85a}$$

$$L_2 \frac{\mathrm{d}}{\mathrm{d}t}\mathbf{i}_{2,\alpha\beta} = \mathbf{v}_{\mathrm{C},\alpha\beta} - \mathbf{v}_{2,\alpha\beta} - (R_\mathrm{C} + R_{\mathrm{L}2})\mathbf{i}_{2,\alpha\beta} + R_\mathrm{C}\mathbf{i}_{1,\alpha\beta} \tag{2.85b}$$

$$C_\mathrm{lc} \frac{\mathrm{d}}{\mathrm{d}t}\mathbf{v}_{\mathrm{C},\alpha\beta} = \mathbf{i}_{1,\alpha\beta} - \mathbf{i}_{2,\alpha\beta} \tag{2.85c}$$

The stationary $\alpha\beta$ frame system can mapped into the synchronous reference dq frame by substituting $\mathbf{x}_{\alpha\beta\gamma} = \mathbf{T}_{\mathrm{dq0}}^{-1}\mathbf{x}_{\mathrm{dq0}}$. The equations in (2.85) can be written in the dq coordinates with

$$L_1 \frac{\mathrm{d}}{\mathrm{d}t}\mathbf{i}_{1,\mathrm{dq}} = \begin{bmatrix} -(R_\mathrm{C}+R_{\mathrm{L}1}) & \omega L_1 \\ -\omega L_1 & -(R_\mathrm{C}+R_{\mathrm{L}1}) \end{bmatrix} \mathbf{i}_{1,\mathrm{dq}} + \mathbf{v}_{1,\mathrm{dq}} - \mathbf{v}_{\mathrm{C,dq}} + R_\mathrm{C}\mathbf{i}_{2,\mathrm{dq}} \tag{2.86a}$$

$$L_2 \frac{\mathrm{d}}{\mathrm{d}t}\mathbf{i}_{2,\mathrm{dq}} = \begin{bmatrix} -(R_\mathrm{C}+R_{\mathrm{L}2}) & \omega L_2 \\ -\omega L_2 & -(R_\mathrm{C}+R_{\mathrm{L}2}) \end{bmatrix} \mathbf{i}_{2,\mathrm{dq}} + \mathbf{v}_{\mathrm{C,dq}} - \mathbf{v}_{2,\mathrm{dq}} + R_\mathrm{C}\mathbf{i}_{1,\mathrm{dq}} \tag{2.86b}$$

$$C_\mathrm{lc} \frac{\mathrm{d}}{\mathrm{d}t}\mathbf{v}_{\mathrm{C,dq}} = \begin{bmatrix} 0 & \omega C_\mathrm{lc} \\ -\omega C_\mathrm{lc} & 0 \end{bmatrix} \mathbf{v}_{\mathrm{C,dq}} + \mathbf{i}_{1,\mathrm{dq}} - \mathbf{i}_{2,\mathrm{dq}} \tag{2.86c}$$

A set of equations (2.86) can be written in the matrix form

$$\frac{\mathrm{d}}{\mathrm{d}t}\begin{bmatrix} i_{1,\mathrm{d}} \\ i_{1,\mathrm{q}} \\ i_{2,\mathrm{d}} \\ i_{2,\mathrm{q}} \\ v_{\mathrm{C,d}} \\ v_{\mathrm{C,q}} \end{bmatrix} = \begin{bmatrix} -\frac{(R_\mathrm{C}+R_{\mathrm{L}1})}{L_1} & \omega & \frac{R_\mathrm{C}}{L_1} & 0 & -\frac{1}{L_1} & 0 \\ -\omega & -\frac{(R_\mathrm{C}+R_{\mathrm{L}1})}{L_1} & 0 & \frac{R_\mathrm{C}}{L_1} & 0 & -\frac{1}{L_1} \\ \frac{R_\mathrm{C}}{L_2} & 0 & -\frac{(R_\mathrm{C}+R_{\mathrm{L}2})}{L_2} & \omega & \frac{1}{L_2} & 0 \\ 0 & \frac{R_\mathrm{C}}{L_2} & -\omega & -\frac{(R_\mathrm{C}+R_{\mathrm{L}2})}{L_2} & 0 & \frac{1}{L_2} \\ \frac{1}{C_\mathrm{lc}} & 0 & -\frac{1}{C_\mathrm{lc}} & 0 & 0 & \omega \\ 0 & \frac{1}{C_\mathrm{lc}} & 0 & -\frac{1}{C_\mathrm{lc}} & -\omega & 0 \end{bmatrix} \begin{bmatrix} i_{1,\mathrm{d}} \\ i_{1,\mathrm{q}} \\ i_{2,\mathrm{d}} \\ i_{2,\mathrm{q}} \\ v_{\mathrm{C,d}} \\ v_{\mathrm{C,q}} \end{bmatrix} + \begin{bmatrix} \frac{1}{L_1} & 0 & 0 & 0 \\ 0 & \frac{1}{L_1} & 0 & 0 \\ 0 & 0 & -\frac{1}{L_2} & 0 \\ 0 & 0 & 0 & -\frac{1}{L_2} \\ 0 & 0 & 0 & 0 \\ 0 & 0 & 0 & 0 \end{bmatrix} \begin{bmatrix} v_{1,\mathrm{d}} \\ v_{1,\mathrm{q}} \\ v_{2,\mathrm{d}} \\ v_{2,\mathrm{q}} \end{bmatrix} \tag{2.87}$$

To obtain a complete model, also the DC link has to be modeled. The converter-side voltages $v_{1,\mathrm{d}}$ and $v_{1,\mathrm{q}}$ can be presented with the switching vector and the DC link voltage by

$$v_{1,\mathrm{d}} = sw_\mathrm{d} V_\mathrm{dc}, \tag{2.88a}$$

$$v_{1,\mathrm{q}} = sw_\mathrm{q} V_\mathrm{dc}, \tag{2.88b}$$

where the switching vector $\mathbf{sw}_{\mathrm{dq}}$ can be defined in synchronous coordinates by

$$\mathbf{sw}_{\mathrm{dq}} = sw_\mathrm{d} + jsw_\mathrm{q} = \frac{2}{3}(a^0 sw_\mathrm{a} + a^1 sw_\mathrm{b} + a^2 sw_\mathrm{c}). \tag{2.89}$$

The switching variable *sw* can be defined as

$$sw_{k|k=a,b,c} = \begin{cases} 1/2, & \text{when connected to the positive potential} \\ -1/2, & \text{when connected to the negative potential} \end{cases} \tag{2.90}$$

The DC link voltage equation can be defined by

$$C_{\mathrm{dc}}\frac{\mathrm{d}}{\mathrm{d}t}V_{\mathrm{dc}} = i_{\mathrm{dc}} - i_{\mathrm{load}}, \tag{2.91}$$

where i_{dc} is the current fed to the DC link capacitor by the DC/DC converter, and i_{load} is the DC link current drawn by the grid converter. If the grid converter is assumed ideal, the load current i_{load} can be written as

$$i_{\mathrm{load}} = sw_{\mathrm{a}}i_{\mathrm{a}} + sw_{\mathrm{b}}i_{\mathrm{c}} + sw_{\mathrm{c}}i_{\mathrm{c}} = \frac{3}{2}(sw_{\mathrm{d}}i_{1,\mathrm{d}} + sw_{\mathrm{q}}i_{1,\mathrm{q}}). \tag{2.92}$$

By substituting Equation (2.88) to (2.87) and Equation (2.92) to (2.91), the large-signal model of the three-phase VSI with the LC filter and the grid impedance can be written as

$$\frac{\mathrm{d}}{\mathrm{d}t}\begin{bmatrix} i_{1,\mathrm{d}} \\ i_{1,\mathrm{q}} \\ i_{2,\mathrm{d}} \\ i_{2,\mathrm{q}} \\ v_{\mathrm{C,d}} \\ v_{\mathrm{C,q}} \\ V_{\mathrm{dc}} \end{bmatrix} = \begin{bmatrix} -\frac{(R_{\mathrm{C}}+R_{\mathrm{L1}})}{L_1} & \omega & \frac{R_{\mathrm{C}}}{L_1} & 0 & -\frac{1}{L_1} & 0 & \frac{sw_{\mathrm{d}}}{L_1} \\ -\omega & -\frac{(R_{\mathrm{C}}+R_{\mathrm{L1}})}{L_1} & 0 & \frac{R_{\mathrm{C}}}{L_1} & 0 & -\frac{1}{L_1} & \frac{sw_{\mathrm{q}}}{L_1} \\ \frac{R_{\mathrm{C}}}{L_2} & 0 & -\frac{(R_{\mathrm{C}}+R_{\mathrm{L2}})}{L_2} & \omega & \frac{1}{L_2} & 0 & 0 \\ 0 & \frac{R_{\mathrm{C}}}{L_2} & -\omega & -\frac{(R_{\mathrm{C}}+R_{\mathrm{L2}})}{L_2} & 0 & \frac{1}{L_2} & 0 \\ \frac{1}{C_{\mathrm{lc}}} & 0 & -\frac{1}{C_{\mathrm{lc}}} & 0 & 0 & \omega & 0 \\ 0 & \frac{1}{C_{\mathrm{lc}}} & 0 & -\frac{1}{C_{\mathrm{lc}}} & -\omega & 0 & 0 \\ -\frac{sw_{\mathrm{d}}}{C_{\mathrm{dc}}} & -\frac{sw_{\mathrm{q}}}{C_{\mathrm{dc}}} & 0 & 0 & 0 & 0 & 0 \end{bmatrix}\begin{bmatrix} i_{1,\mathrm{d}} \\ i_{1,\mathrm{q}} \\ i_{2,\mathrm{d}} \\ i_{2,\mathrm{q}} \\ v_{\mathrm{C,d}} \\ v_{\mathrm{C,q}} \\ V_{\mathrm{dc}} \end{bmatrix} + \begin{bmatrix} 0 & 0 & 0 \\ 0 & 0 & 0 \\ -\frac{1}{L_2} & 0 & 0 \\ 0 & -\frac{1}{L_2} & 0 \\ 0 & 0 & 0 \\ 0 & 0 & 0 \\ 0 & 0 & \frac{1}{C_{\mathrm{dc}}} \end{bmatrix}\begin{bmatrix} v_{2,\mathrm{d}} \\ v_{2,\mathrm{q}} \\ i_{\mathrm{dc}} \end{bmatrix}. \tag{2.93}$$

2.3.3 Model analysis

The model presented in Equation (2.93) includes the grid-side impedance formed by the cables and the distribution transformer. Because of the approximation of the grid-side impedance, the effects of a change in the impedance must be observed. The admittances of the filter when varying the grid-side impendance are presented in Fig. 2.20. The figure shows that the resonance frequency decreases when the grid-side inductance increases. In addition, it can be noticed that the magnitude of the resonance peak increases, and as a result of the change in the resonance frequency, the -180 °phase shift frequency decreases. These observations have to be taken into account in the control design, or the grid-side inductance must be measured by the control system (Liserre et al., 2007).

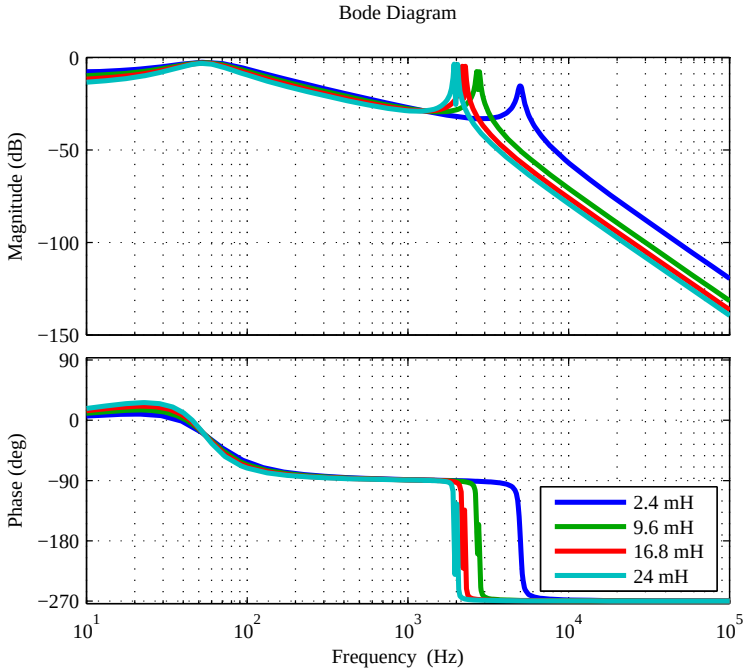

Figure 2.20. Effects of the line impedance and the distribution transformer on the open-loop admittance.

Chapter 3

Design and implementation of the control system

The design of the control system is based on the demands placed by the fuel cell, plant controller, converter topology, and the grid. In this chapter, the limitations are converted into control system requirements, the control board used in the work is introduced, and the design of the control system is carried out. The design process described is not tied to the prototype plant, and it can be used also in other fuel-cell-based systems. At the end of the chapter, the implementation of the control algorithms in the control platform is discussed.

3.1 Converting demands into control system requirements

The operation boundaries of the PCU are given in the introductory chapter, where the limitations set by the fuel cell, the grid, and the converter topologies are reviewed. To obtain the requirements for the control system, the limitations must be derived from the physical characteristics.

Because of the nature of the prototype system, the requirements may be exaggerated; however, there is no specific information available of the characteristics of the SOFC used in the project. The protection of the PCU is not tied to the control design, and therefore, it is defined and explained in Subsection 3.5.2.

3.1.1 DC/DC converter

It has been stated above that overcurrent is hazardous to the fuel cell, and it leads to the degradation of the electrodes. This in turn results in a decrease in the fuel cell's capability to produce electricity. Therefore, it is justified to choose the output current of the fuel cell as the primary control variable for the DC/DC converter. There are several control methods for the current mode control. Lim et al. (2005) compared different current mode control (CMC) schemes for asymmetrically driven PWM DC/DC converters. The

compared schemes were peak current control (PCC), charge control (CC), and average current control (ACC). The result of the study was that the ACC was found to provide superior closed-loop performance. Consequently, the ACC is a good starting point to control the inner loop of the DC/DC converter in fuel cell applications, where the performance of the current regulation is highly important and the ability to control the cell current is necessary. The choice of current as the primary reference variable for the DC/DC converter sets limits on the converter topology. In practice, this means that the input current must be controllable in the chosen topology.

The lack of overloading tolerance also sets a requirement for no overshoot of the control system. This means that the dynamics of the control system must be designed so that an overshoot does not occur, but the dynamics of the system is as fast as possible. The step response overshoot can be mitigated by filtering the reference value, although the system is underdamped. This filtering makes it possible to increase the bandwidth without a significant overshoot. Therefore, a sufficiently fast controller is important in abnormal operating conditions, where it restricts the current drawn from the stack.

The current ripple requirement for the fuel cell must also be considered when designing a control system for the DC/DC converter of the fuel cell PCU. Because the switching frequency ripple does not have a significant effect on the fuel cell, the attention is directed to the low-frequency current ripple. For the PCC it is stated that it is not able to operate at the duty cycle values of $D > 0.5$, and it suffers from the low-frequency variation of the input current. Therefore, it is not suitable for controlling the input current of the PCU. Liu and Lai (2007) investigated an active control method, which uses a current-loop control to mitigate the effects of the inverter-related low-frequency ripple current (second harmonic) seen by the fuel cell stack. The system is proven to be feasible for fuel cell power conditioning systems. In the study, a single-phase inverter was investigated, but the principle is applicable also to three-phase systems. The existence of the second harmonic in a three-phase VSI is presented for example in (Hwang et al., 2007), and it originates from the grid unbalance.

The feasible operation area for the fuel cell can be determined from the characteristics of the fuel cell and the DC link. The lowest input voltage is defined by the maximum fuel utilization ratio and the corresponding stack output voltage. For example, if the fuel utilization ratio u is limited to $u = 0.8$, the minimum operation voltage at which the operation must be guaranteed can be found from a certain point of the V-I curve of the chosen fuel cell. The maximum input voltage is determined by the output voltage range of the fuel cell stack. The ideal voltage corresponds to the open-circuit voltage, and the fuel utilization ratio is close to $u = 0$. The maximum operation voltage at which stability has to be attained is consequently the open-circuit voltage of the stack.

The main control variable of the SOFC plant under study is the output current of the stack (Halinen et al., 2011), which is used to control the auxiliary systems such as blowers and heaters. Thus, the input current I_{lb} of the converter is an obvious choice for the control variable. To be precise, the converter must operate in the current-controlled mode.

The SOFC plant is usually ramped to the nominal point at a rate of a couple of amperes per minute (Halinen et al., 2011). The ramp sets the requirement of the response to the unit-ramp reference for the control system. A similar ramp occurs also in shutdown, when the plant is run down at a constant rate.

For the DC/DC converter, the following requirements can be set related to the fuel cell and the grid interface:

- the DC/DC converter has to be current controlled,

- no input current steady-state error is allowed,
- there should be a small or no overshoot, and
- sufficient V_{dc} to I_{lb} ripple mitigation has to be ensured at low frequencies.

3.1.2 Grid converter

The major impact of the grid converter from the viewpoint of the fuel cell is its tendency to generate low-frequency harmonics to the DC link. The harmonics are mostly multiples of the grid frequency, which is due to the operation principle of the grid converter. Hence, when considering the fuel cell, the main task in the control of the grid converter is to minimize the low-frequency harmonics seen by the fuel cell stack. Instead, from the perspective of the utility grid, a self-explanatory task of the control system is to meet the requirements set by the grid standards and grid codes.

Acharya et al. (2003) compared Sinusoidal Pulse Width Modulation (SPWM) and Space Vector Pulse Width Modulation (SVPWM) in fuel cell applications with a VSI. The SVPWM provides improved DC link utilization over the traditional SPWM; however, the microcrack rate may rise when using the SVPWM. Furthermore, the SVPWM improves the DC link utilization, which allows to use lower DC link voltages, or increases the available control reserve. Although the SVPWM provides improved performance over the SPWM, the enhanced performance causes higher localized current densities and fuel flow rates. Both of these effects are harmful to the fuel cell and can cause degradation of the fuel cell stack.

Despite the fact that the better utilization of the DC link voltage can cause problems for the fuel cell, the SVPWM provides superior controllability over the traditional SPWM. If the SVPWM is connected to the vector control system, it is possible to control the active and reactive part of the power flow separately. The basic principle of the SVPWM makes it suitable for vector control. Therefore, it is justified to use the SVPWM.

For the grid converter, the following requirements can be set:

- compliance with the grid codes and
- minimum interference with the DC/DC stage.

3.1.3 PCU

The control loops of the DC/DC and grid converters require reference values for proper operation. These values are fed by the outer loop control, which controls the behavior of the PCU system. In this section, the commonly used control methods for PCUs in fuel cell systems are reviewed.

Wang et al. (2004) propose a control system where the DC/DC converter is controlled by measuring the load voltage and current at which the load power is calculated. The battery charges and discharges based on the decision made by the measurement of the battery voltage and current. The sum of the load power and the battery power is the power demand from the stack. The voltage of the DC link is regulated by

controlling the output current of the stack. The demand for the output current of the stack is calculated from the power demand and the measured stack voltage. The calculated power is compared with the maximum output current of the stack at the operating point, and if the current is equal to or greater than the maximum current available, the output power of the PCU is adjusted to the maximum value of the power available. If the current demand is smaller than the maximum available current, the reference output power for the fuel cell is set to the sum of the load current and the battery current. A performance analysis of the control system is not made.

Wang and Nehrir (2007b) suggest a control scheme where the DC/DC converter regulates the voltage of the DC link within 5% of its nominal value. The grid converter is controlled by a two-loop current control scheme (Kazmierkowski and Malesani, 1998). The DC/DC converter is controlled by a single voltage loop, which is not able to directly control the input current of the converter, and which is therefore sensitive to overloading and low-frequency current ripple. The modulation scheme of the inverter is suggested to be an SPWM, the performance of which is sluggish compared with the SVPWM. The performance of the control system is evaluated by linear and nonlinear simulation studies.

Park et al. (2008) present a frequency domain compensation scheme and implement the control system with the DSP. The basic idea is to control the DC link voltage and use a QPR (quasi-proportional resonant) controller in the current loop to obtain a high gain at the fundamental frequency. The admittance compensator is adapted to cancel the grid-voltage-induced negative power flow.

Lee et al. (2006) divide the control system into a DC/DC control and a grid converter control. The main target for the controller of the DC/DC converter is to stabilize the DC link voltage. This is achieved by a PI controller. A current control loop is implemented, as recommended by the authors, to improve the performance of the control system. The current reference for the controllers is limited by the plant controller. The grid converter is controlled by a PI-based closed loop control. Because of the configuration of two half-bridge inverters, the control system for voltage balancing is also implemented.

To mitigate the ripple component seen by the fuel cell stack, Kwon et al. (2009) propose a control system with active input current ripple reduction. The reduction technique does not require additional components and could be used as a part of control systems.

Based on the above, we may conclude that the DC/DC controller regulates the DC link voltage in cooperation with the plant controller. The control system of the grid converter assumes a stiff DC link, which is kept within the desired voltage range. Usually, the vector control and the SVPWM are not applied, which is explained by the use of single-phase inverters.

From another point of view, usually in distributed generation, the grid-side controller regulates the voltage of the DC link and maintains the power balance of the system (Timbus et al., 2009). Because in an SOFC plant, the system is usually kept in a desired operating point and no fast response is needed, this control principle could also be applied to fuel cell systems.

A fuel cell sets limitations on the DC/DC converter and the grid converter. The most important single requirement is to operate with the desired current reference. Considering this requirement, a DC link voltage control based on the control of the DC/DC converter is impractical, or even hazardous. At the same time, the usual distributed generation control scheme (Timbus et al., 2009) provides an opportunity to accurately control the stack current, while the DC link voltage controller controls the power fed to the grid.

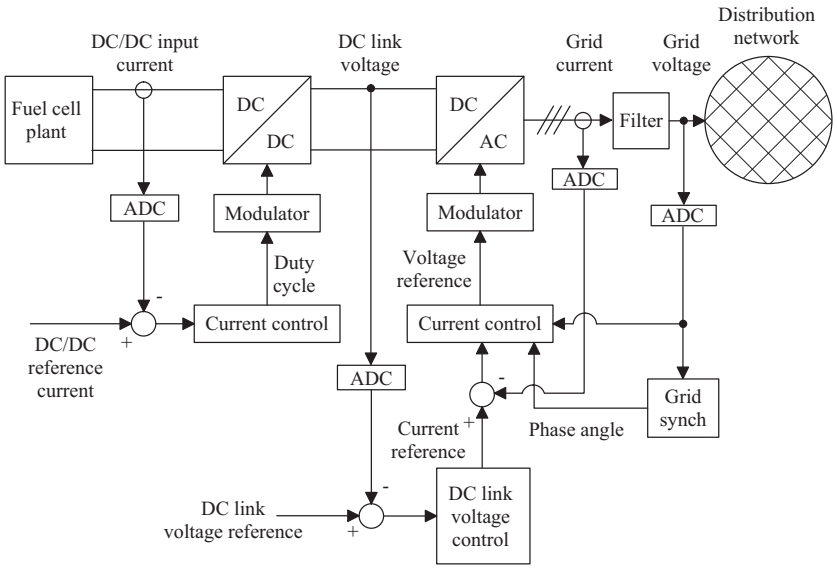

Figure 3.1. Schematic of the PCU under study. ADC refers to the sensor, the sensing network, and the ADCs. Filter is the grid filter, and the distribution network is a three-phase 230/400 V 50 Hz electrical grid.

Based on the previous analysis, the target set for the PCU controller can be to keep the DC link voltage stable. A schematic of the PCU and the proposed control system is presented in Fig. 3.1. In the proposed control system, the DC/DC stage is current controlled, the grid converter is current vector controlled, and the outer loop controls the DC link voltage, and thus, maintains the power balance of the system.

3.2 Control board

Before the control system can be designed, the designer must have an understanding about the control hardware used. In this project, an EDC-AMB (Electronics Design Center - Active Magnetic Bearing) control board (Fig. 3.2) is applied with custom-made connection boards and software.

The connection boards include A/D converters, dSpace connectors, an interface to the PLC used in the automation of the SOFC plant, optical transmitters, and an optical receiver.

The OS (Operating System) used in the control board is μC/OS-II with the Open Source Framework (OSFW) (Salli, 2009). Basically, the only function of the OSFW is to implement the link with the memory mappings of the EMIF (External Memory Interface) without a need for redefinitions. All other software, the FPGA design, and additional hardware are custom made for the project.

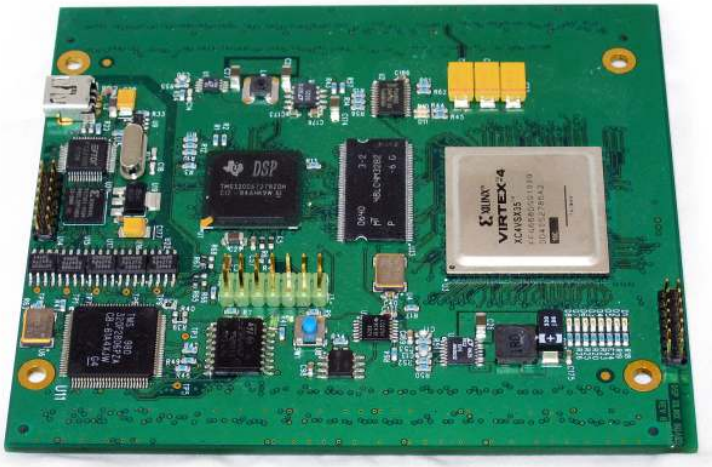

Figure 3.2. Active Magnetic Bearing control board by Electronics Design Center (EDC-AMB board). The board includes a Virtex-4 FPGA, a Texas Instruments TI TMS320C6727b processor, and 128 MB RAM (Random Access Memory). The board is used as the embedded platform in this doctoral thesis.

Table 3.1. Specifications of the control board hardware.

DSP	DSP clk	OS	FPGA	FPGA clk	ADC
TI TMS320C6727b	300 MHz	µC/OS-II	Xilinx XC4VSX35	50 MHz	LTC2341

3.3 Control system design for the RPP converter

The control design for the RPP converter is carried out according to the requirements described above. As the main control variable in the fuel cell plant is usually the current drawn from the stack, the current control is chosen as the control principle of the converter. The block diagram of the control system is presented in Fig. 3.3, and the specifications of the control board hardware are presented in Table 3.1.

In Figs. 3.3 and 3.4, $I_{\mathrm{ref}}(z)$ is the discrete reference value of the input current $G_{\mathrm{c}}(z)$ is the discrete current controller, qPWM is the PWM quantizer, which maps the values with the accuracy of the LSB, T_{s1} is the PWM sample time, and $G_{\mathrm{ci}}(s)$ is the converter transfer function. The feedback path includes several items, which are required when modifying the sensor information into a readable form. The gain R_{sens} converts the current signal of the LEM LF-205-S into voltage, $H(s)$ is the anti-aliasing (AA) filter, K_{oa} is the amplifier gain to rescale the voltage suitable for the ADC (LTC2351), T_{s2} is the controller sample time, qADC is the ADC quantizer, and K_{inv} is a gain to convert the output value of the ADC back into the actual input current.

The design process is carried out by observing the current loop gain as described in (Erickson and Maksimovic, 2001), which is modified to fit the digital control system applied in (Al-Atrash and Batarseh, 2007)

$$T(s) = \frac{K_{\mathrm{sens}} R_{\mathrm{sens}} H(s) K_{\mathrm{oa}} K_{\mathrm{adc}} K_{\mathrm{inv}} G_{\mathrm{c}}(s) G_{\mathrm{ci}}(s)}{V_{\mathrm{m}}}, \tag{3.1}$$

where K_{sens} is the current sensor gain, R_{sens} is the current sensing precision resistor, K_{oa} is the gain of the operational amplifier, K_{adc} is the ADC gain, V_{m} is the peak-to-peak amplitude of the modulator sawtooth waveform, and

$$G_{\mathrm{ci}}(s) = \frac{\tilde{i}_{\mathrm{lb}}(s)}{\tilde{d}(s)}. \tag{3.2}$$

The quantization effects are neglected at this point of design. The V_{m} can be omitted because in the digital PWM implementation, the duty cycle from the control system is converted directly to the corresponding compare value.

In this case, the AA filter is a first-order RC filter with a bandwidth of 2500 Hz. The filter can be expressed

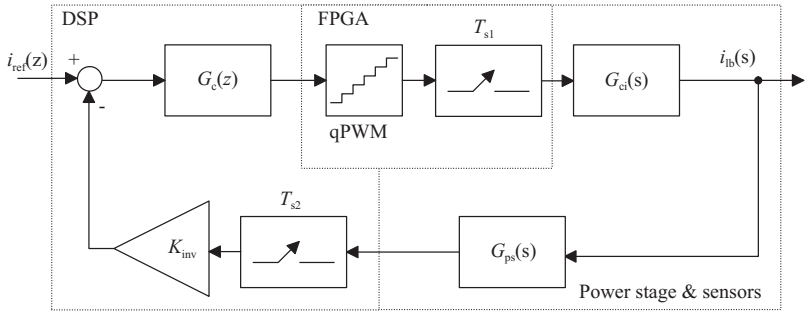

Figure 3.3. Block diagram of the RPP converter with the current control. The control diagram is divided into the DSP, FPGA, and the power stage and sensors according to the hardware. The ADCs are modeled as a series connection of the ideal sample and hold circuit and the quantization block. The PWM blocks behave as DA converters, which maps the discrete $D(z)$ signal into the continuous time signal of the switch states.

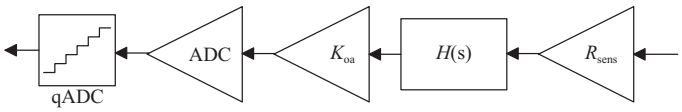

Figure 3.4. Block diagram of the feedback path of the power stage and the sensors $G_{ps}(s)$. R_{sens} is the sensing resistor of the secondary current of the current transducer, $H(s)$ is the anti-aliasing filter, K_{oa} is the amplifier gain, and qADC is the ideal quantizer of the ADC.

Table 3.2. Sampling regions of the prototype system.

$1/T_{s1}$	$1/T_{s2}$
5 kHz	50 kHz

by

$$H(s) = \frac{1}{1+\frac{s}{\omega_0}}, \tag{3.3}$$

where ω_0 is the desired crossover frequency in rad/sec. The inverse sensor gain can be defined as

$$K_{inv} = \frac{1}{K_{sens}R_{sens}K_{oa}K_{adc}}. \tag{3.4}$$

The inverse sensor gain is used to scale the values of the sensing network back to the measured quantities. Based on above, the open loop transfer function (3.1) can be written as

$$T(s) = G_c(s)H(s)G_{ci}(s). \tag{3.5}$$

3.3.1 Sampling

Owing to the multiprocessor implementation of the control system, the control system includes multiple sampling regions. The fastest sampling region is the DPWM and the ADC. The second sampling region is the controller. The protection functions of the system are implemented in the controller because of the easy implementation and modification of the C-code in the DSP. The protection delay is therefore a multiple of T_{s1}. Because of the multiple sampling regions, the computations of the DPWM and the ADC do not produce as significant a delay as in (Maksimovic and Zane, 2007), where the controller is updated once in the sampling period.

If the DSP is fast enough to update the controller during the period T_{s1}, the maximum delay in the control loop caused by the PWM sampling is T_{s2}. The modulator delay can be modeled by Equation (1.21) where τ is the sampling period of the DPWM (T_{s2}). The sampling regions of the applied control system are presented in Table 3.2. By substituting Equation (1.21) to (3.5), we obtain the loop gain

$$T(s) = G_c(s)T_{delay}(s)H(s)G_{ci}(s), \tag{3.6}$$

which observes the delay caused by the digital modulator.

3.3.2 Controller

In (Choi et al., 2008), the performance of the PCC, CC, and the ACC are reviewed, and the ACC is found to provide the best performance. It is also able to operate at $D > 0.5$. Combined with the unavoidable presence of the AA filter, the ACC controller is chosen. The controller transfer function can be written as in (Sun and Bass, 1999):

$$G_c(s) = \frac{K_c(1+s/\omega_z)}{s(1+s/\omega_p)}, \tag{3.7}$$

where K_c is the gain, -ω_p is the controller pole, and -ω_z is the controller zero.

Because of the digital implementation, the AA filter is included in the loop gain (3.6). If we examine the controller transfer function (3.7), the AA filter transfer function (3.3), and the loop gain (3.1), we notice that we are able to achieve the high-frequency pole with the AA filter. As a result of the AA filter in the loop, a modified controller transfer function becomes

$$G_c(s) = \frac{K_c(1+s/\omega_z)}{s} \tag{3.8}$$

and the loop gain (3.6) remains unaltered.

If the AA filter and the discretization time are assumed fixed, this modification leads to a situation where there are a two degrees of freedom when designing the controller. The gain margin is tied to the Q-value (Erickson and Maksimovic, 2001), and therefore, it provides a suitable tool for the control design. In this application, it is desired to have sufficient attenuation at the low frequencies and to have a small overshoot or no overshoot at all. To achieve the desired characteristics, the zero ω_z has to be set to one-third of the resonance frequency to increase the gain margin, and K_c has to be altered to achieve the sufficient attenuation at the low frequencies (Liu and Lai, 2007).

3.3.3 Effects of quantization

Quantization has an influence on the control system such that there are only certain possible values in the feedforward and feedback paths. The system presented in Fig. 3.3 contains two quantization blocks. The first is in the feedforward path, and it is a quantization of the DPWM. In other words, the DPWM can only have D of a multiple of the LSB.

The integer range of the period is tied to the programmable switching frequency

$$period = \frac{F_{fpga}}{F_{sw}} = 1000 \tag{3.9}$$

and as the switching waveform is sawtooth, the control range of D is half of the period (3.9).

The quantization step is the value of the LSB. Because the maximum value of the D is 1.0, which is mapped as a counter value $period/2$, and the waveform is sawtooth, the quantization step of the DPWM is

$$\Delta D_{DPWM} = \frac{range}{period/2} = \frac{1.0}{period/2} = 0.002. \tag{3.10}$$

Thus, the control system is able to change D in steps of 0.002. The principle of the determination of the quantization step is presented in Fig. 3.5.

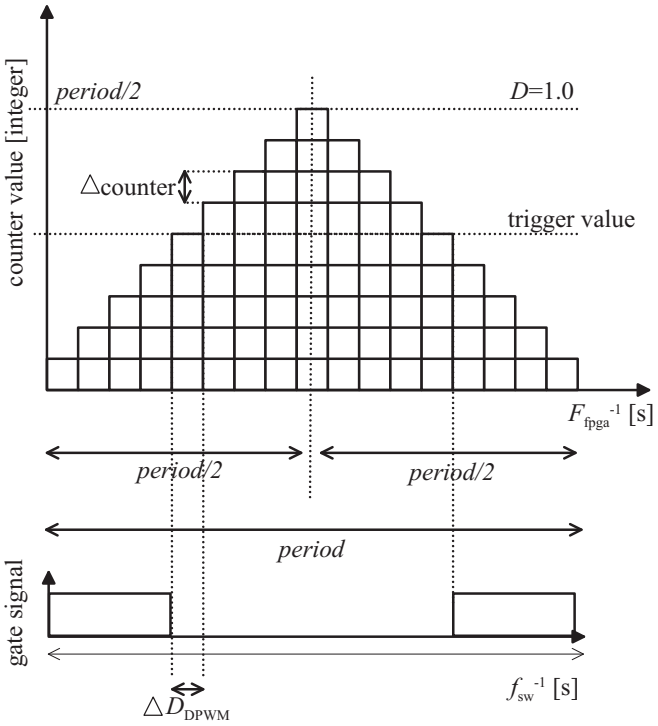

Figure 3.5. Determination of the quantization step with the implemented digital pulse width modulator. The counter waveform is a sawtooth waveform, and the maximum value of the counter is half of the period length in integers. The frequency of the counter is the frequency of the FPGA, and the switching frequency of the modulator is $period \times F_{\mathrm{fpga}}^{-1}$.

Similarly, the LSB value of the ADC is

$$\Delta_{\mathrm{ADC}} = \frac{250\mathrm{A}}{2^{14}}, \tag{3.11}$$

which means that the output current is mapped into the multiples of (3.11). In practice, the LC is not present, if the value of the zero-error (3.11) maps into the exact bin of (3.10), when switching between adjacent bins of D does not occur. The equation shows that the system applies a 14-bit A/D conversion. If the bit count of the ADC is decreased, for example to lower the costs, the LC phenomena are less likely to occur because of the more coarse measuring range.

Peterchev and Sanders (2003) suggest three conditions to avoid the LC in digitally controlled converters. The first condition states that the resolution of the DPWM must be greater than the resolution of the ADC. A one bit difference is considered sufficient to guarantee that the quantized value of the D falls into the zero-error bin. From Equations (3.10) and (3.11) we can see that the condition is not met, and the system is likely to suffer from the LC.

When operating with a SOFC, the possibility of LC must be considered to ensure that the current ripple limits are met. The possible LC component of the input current ripple can be calculated by applying the DC model of the system. The deriving of the DC model is presented in the Appendix A. The LC ripple component can be estimated by (3.10) and the steady-state input current from

$$I_{\mathrm{lb}} = \frac{V_{\mathrm{g}}}{\frac{R_{\mathrm{l}}}{M(D)^2}}. \tag{3.12}$$

The ripple component is caused by the switching of the two adjacent quantization steps, and therefore, the approximation of the LC component can be calculated by

$$\Delta I_{\mathrm{lb,lc}} = \left| I_{\mathrm{lb}}(D + \Delta D_{\mathrm{DPWM}}) - I_{\mathrm{lb}}(D - \Delta D_{\mathrm{DPWM}}) \right|. \tag{3.13}$$

Equation (3.13) can be used to evaluate the total low-frequency ripple component with the switching ripple. Due to the fact that the operating point cannot be predicted accurately, the equations should be used as a suggestion or a coarse approximation. In this thesis, the equation is applied together with the switching frequency component to approximate the total ripple component seen by the stack.

3.3.4 Digital implementation

If Equation (3.8) is compared with the interacting form of the PID (Proportional Integral Derivative) controller (Åström and Wittenmark, 1997)

$$G_{\mathrm{pid}}(s) = K(1 + \frac{1}{sT_{\mathrm{i}}})(1 + sT_{\mathrm{d}}), \tag{3.14}$$

and T_{d} is set to zero, the following equation can be written

$$\frac{K_{\mathrm{c}}(1 + s/\omega_{\mathrm{z}})}{s} = K(1 + \frac{1}{sT_{\mathrm{i}}}) \Leftrightarrow \tag{3.15a}$$

$$K_{\mathrm{c}} + K_{\mathrm{c}}\frac{s}{\omega_{\mathrm{z}}} = Ks + Ks\frac{1}{sT_{\mathrm{i}}} \Leftrightarrow \tag{3.15b}$$

$$K_{\mathrm{c}} + K_{\mathrm{c}}\frac{1}{\omega_{\mathrm{z}}}s = \frac{K}{T_{\mathrm{i}}} + Ks. \tag{3.15c}$$

Based on Equation (3.15c), we may state that the controller can be implemented with the commonly used PID controller by choosing the parameters as follows:

$$K = \frac{K_c}{\omega_z}, \text{ and} \tag{3.16a}$$

$$T_i = \frac{K}{K_c} = \frac{K_c}{\omega_z} \cdot \frac{1}{K_c} = \frac{1}{\omega_z}, \tag{3.16b}$$

which leads to the following coefficients for the parallel form PID controller

$$K_p = K, \tag{3.17a}$$

$$K_i = \frac{K}{T_i}, \text{ and} \tag{3.17b}$$

$$K_d = KT_d. \tag{3.17c}$$

Based on the above, the general digital PID controller can be used to implement the ACC control of the RPP converter, and anti-windup can be implemented by the zero injecting method when the output is saturated.

3.3.5 Tuning

The target for the controller tuning was to achieve adequate mitigation of the low frequencies and a small or no overshoot for the system. Based on the targets established, the suitable parameters for the controller were found by a trial-and-error method. Based on the previous statements, the following parameters were selected for the controller:

$$K_c = 0.3780 \tag{3.18a}$$

$$\omega_z = 414.7, \tag{3.18b}$$

which leads to the following parameters for the PID implementation of the current controller:

$$K = 0.0009115 \tag{3.19a}$$

$$K_i = 0.3780 \tag{3.19b}$$

$$K_d = 0 \tag{3.19c}$$

The gain and phase margins given by the parameters presented in Equation (3.19) with the linearized models described by Equations (2.66–2.76) are presented in Table 3.3. From the phase margins, we can see that a significant overshoot should not occur based on the relation between the phase margin and the Q-value (Erickson and Maksimovic, 2001).

With the loop gains defined by Equation (3.6) and by varying D =[0.1–0.7], we get the Bode plot presented in Fig. 3.6 and the corresponding step responses presented in Fig. 3.7. Figure 3.6 shows that the system remains stable when D increases, although the phase and gain margins decrease. The upper limit of the examination can be limited to D=0.7 because the upper limit of saturation is set to D=0.7 by the controller software. This limitation is caused by the limitations of the converter hardware. In addition, it can be noticed that the loop gain at 100 Hz is poor, and may cause problems when operating with the grid converter, because the fuel cell stack does not tolerate the low-frequency current ripple. The loop gains at 100 Hz are presented in Table 3.4.

Table 3.3. Phase and gain margins of the loop gains of the linearized model of the RPP converter with the PID controller. Fig. 3.6 shows that when D increases from 0.1 to 0.7, the gain and phase margins decrease. We can also see that at low values of D, the attenuation at the 100 Hz is low. This can cause problems when operating with the grid converter, because the fuel cell stack has a poor tolerance to the low-frequency current ripple.

Parameter	D=0.4	D=0.57
Gain margin	26.8 dB (at 4580 Hz)	22.7 dB (at 4270 Hz)
Phase margin	81.3 ° (at 500 Hz)	74.8 ° (at 625 Hz)

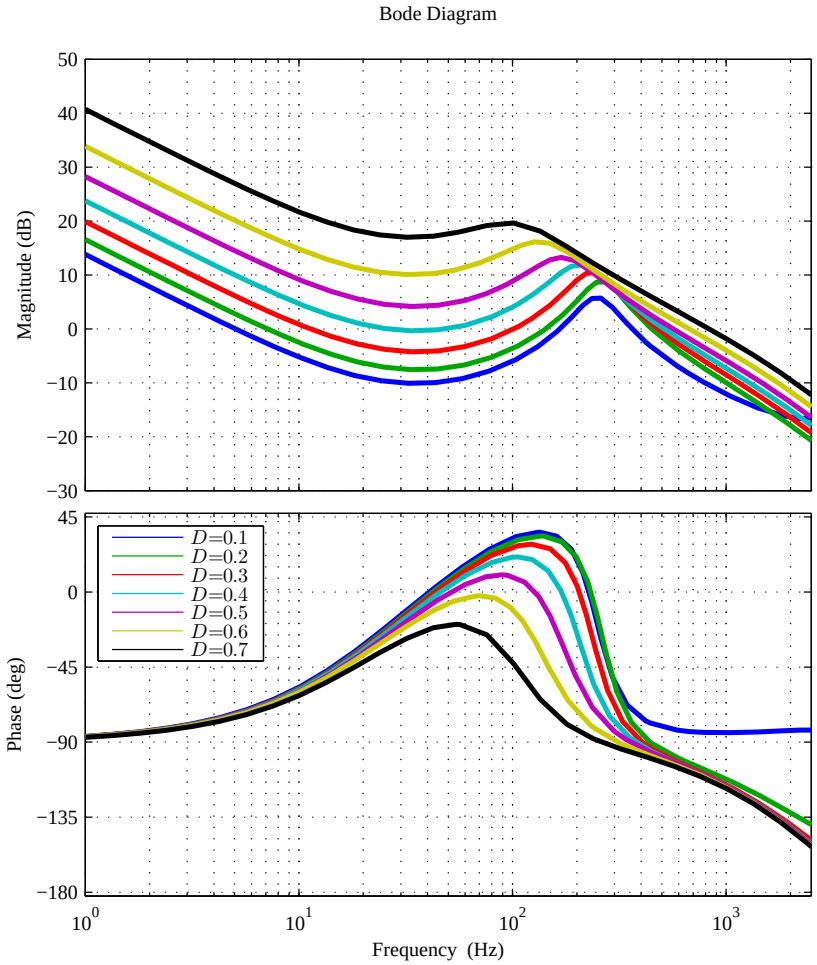

Figure 3.6. Loop gains (3.6) of the RPP converter with the PID controller when D is varied. The figure shows that when increasing D, the loop gain increases and the quality factor (Q-value) decreases.

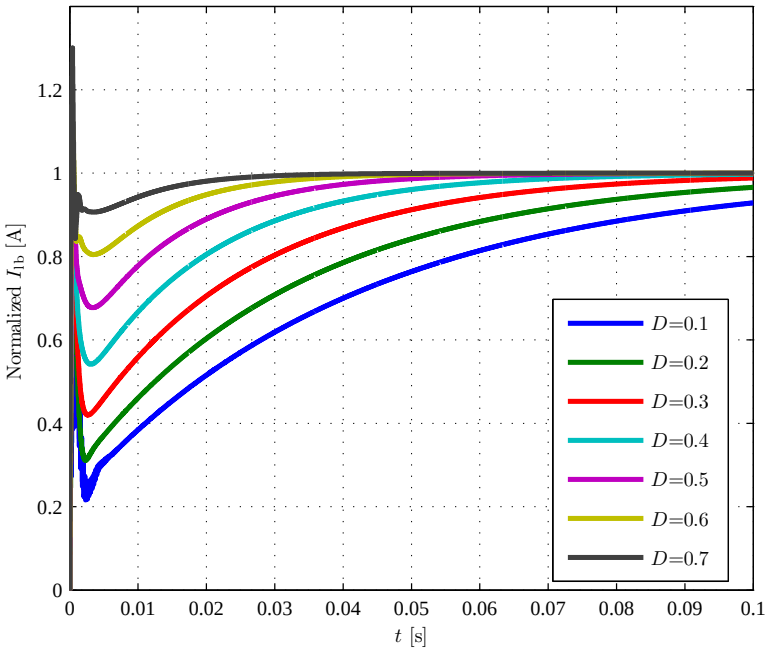

Figure 3.7. Normalized current step responses of the RPP converter with the PID controller when D is varied. The figure shows that when increasing D, the rise-time decreases and the overshoot increases. It can be stated that there is no overshoot visible up to D=0.5.

Table 3.4. Loop gains at 100 Hz with the PID controller. The table shows that the loop gain is poor at 100 Hz, and therefore, the attenuation of the 100 Hz ripple caused by the grid converter is poor. Because the fuel cell stack has no tolerance to the low-frequency ripple current, the poor attenuation can cause problems when operating with the grid converter.

D	Loop gain at 100 Hz [dB]
0.1	-5.9
0.2	-3.6
0.3	-0.1
0.4	4.0
0.5	8.9
0.6	14.8
0.7	19.6

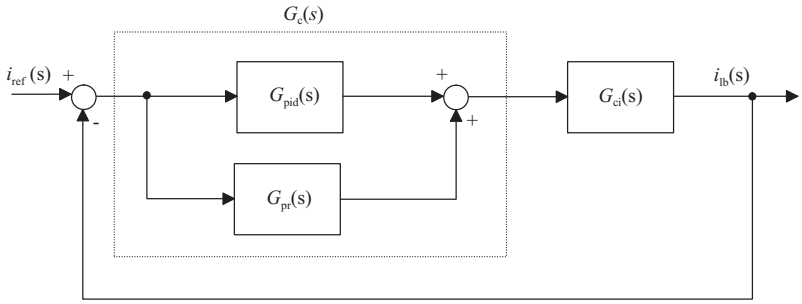

Figure 3.8. Parallel configuration of the PID controller and the P+R controller to improve the 100 Hz mitigation caused by the grid converter with an unbalanced grid.

3.3.6 P+R controller

From Fig. 3.6 we can see that the loop gain is low at the low frequencies, and the gain at the 100 Hz is below 20 dB in all cases. To improve the 100 Hz mitigation, the P+R (Proportional + Resonant) controller with a nonideal integrator and a grouped K_p term (Teodorescu et al., 2011)

$$G_{pr}(s) = K_p + \frac{2K_i\omega_c s}{s^2 + 2\omega_c s + \omega_m^2} \tag{3.20}$$

is added in parallel to the PID controller. The controller is presented in Fig. 3.8. In Equation (3.20), K_p is the proportional gain, K_i can be used to control the gain, ω_c is a parameter that can be used to widen the bandwidth of the controller, and ω_m is the frequency of the gain peak.

The overall controller transfer function becomes

$$G_c(s) = G_{pid}(s) + G_{pr}(s). \tag{3.21}$$

By substituting Equation (3.21) with the following parameters

$$K_p = 0.001 \tag{3.22a}$$

$$K_i = 0.01 \tag{3.22b}$$

$$\omega_c = 2\pi \cdot 10 \tag{3.22c}$$

$$\omega_m = 2\pi \cdot 100 \tag{3.22d}$$

to Equation (3.6), we can draw a similar Bode plot with the varying D as in Fig. 3.6. The Bode plot is presented in Fig. 3.9 and the step response in Fig. 3.10. The figure shows that the gain of the 100 Hz has increased approximately by 20 dB, which increases the mitigation of the harmful low-frequency ripple seen by the SOFC stack.

As a result of the modification to the controller, the gain and phase margins have to be recalculated to make sure that the system remains stable. The gain and phase margins of the system with the PID and P+R controllers are presented in Table 3.5. The table shows that the gain and phase margins decrease compared with the system without a P+R controller. Figure 3.11 shows the step response from 0 to 100 A with a disturbance of 10 A at 100 Hz. In the figure we can see that the P+R controller mitigates the harmful 100 Hz component.

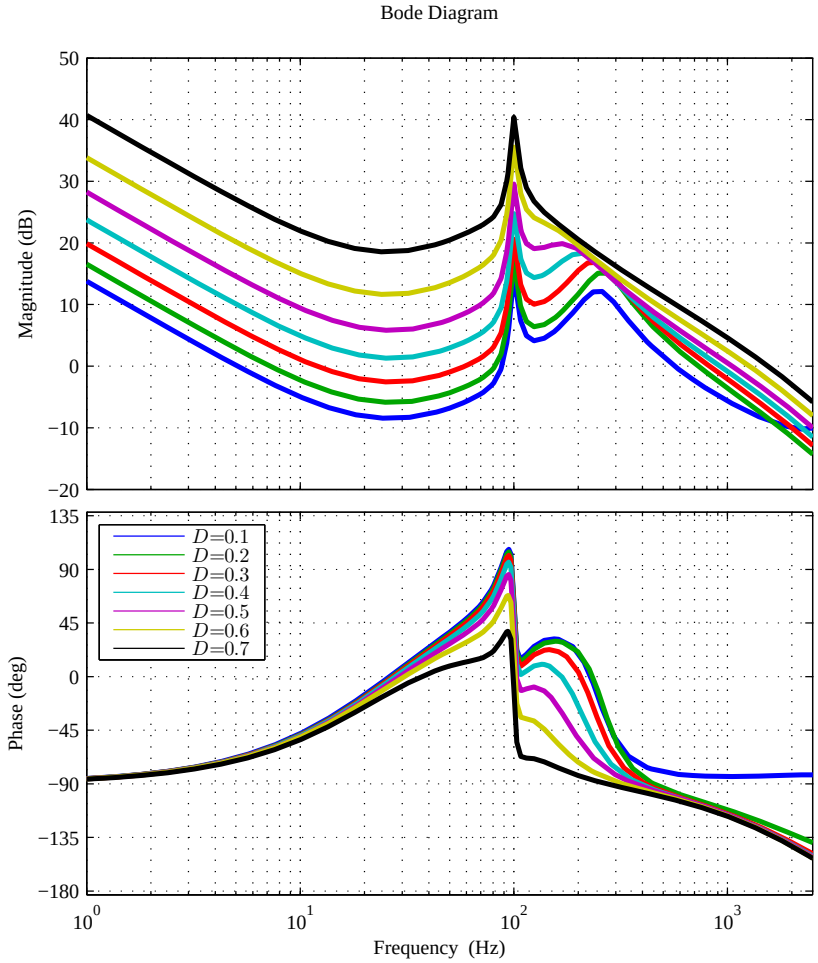

Figure 3.9. Loop gains (3.6) of the RPP converter with the PID and P+R controllers.

Table 3.5. Phase and gain margins of the loop gains of the linearized model of the RPP converter with the PID+PR controller.

Parameter	D=0.4	D=0.57
Gain margin	19.9 dB (at 4500 Hz)	16.3 dB (at 4280 Hz)
Phase margin	66.5 ° (at 920 Hz)	58.3 ° (at 1180 Hz)

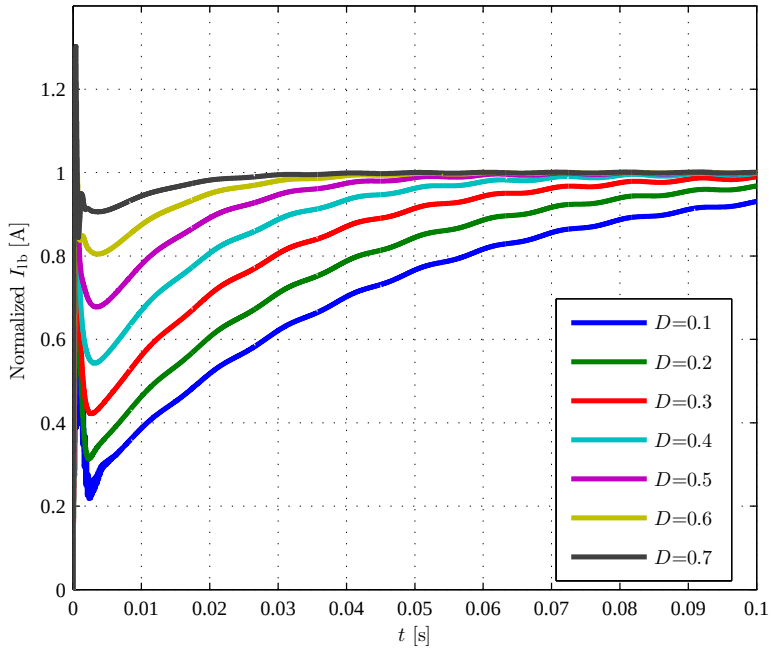

Figure 3.10. Normalized current step responses of the RPP converter with the PID and P+R-controllers with the varying *D*. By comparing the figure with Fig. 3.7, we can see that when a P+R controller is added in parallel to the PID controller, a ripple component is induced. However, the ripple component is small and decreases when *D* increases.

Table 3.6. Loop gains at 100 Hz with the parallel connection of the PID controller and the P+R controller. By comparing the loop gains of the PID controller presented in Table 3.4, we can see that the 100 Hz attenuation is increased approximately by 20 dB in the entire operation range. This increase in the loop gain improves the low-frequency ripple component attenuation when operating with the grid converter. Without using the P+R controller, a similar result would be achieved by increasing the DC link capacitor, which would increase the total cost of the converter.

D	Loop gain at 100 Hz [dB]
0.1	14.7
0.2	17.1
0.3	20.6
0.4	24.8
0.5	29.6
0.6	35.6
0.7	40.4

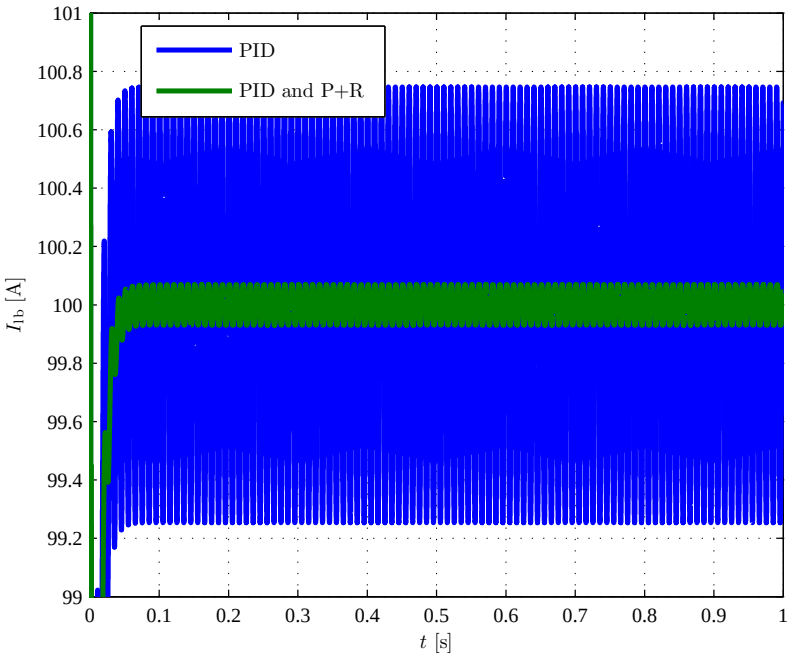

Figure 3.11. Mitigation of the 100 Hz disturbance with the PID and parallel connection of the PID and P+R controllers. The step is 0 to 100 A with a 10 A disturbance signal at 100 Hz. In the figure we can see that the designed P+R controller mitigates the harmful 100 Hz component.

Hence, the gain and phase margins are decreased, but the mitigation of the harmful low-frequency ripple is increased, from which we may conclude that the proposed method can be justified. On the other hand, it should be considered whether it is possible to design a single controller with adequate attenuation of the second harmonic if a smaller phase margin is allowed.

3.3.7 Conclusions on the RPP controller design

Considering the requirements set for the control design, we may conclude that these requirements were met. The designed current-controlled control system has no steady-state error and no significant overshoot. After adding the R+P controller in parallel to the traditional PID controller, the mitigation of the second harmonic of the grid interface was improved. An alternative method to improve the second harmonic mitigation is to increase the capacitance of the DC link capacitor. Increasing the capacitance of the DC link capacitor, however, increases the total costs of the PCU. By a proper control design, and from the viewpoint of the second harmonic mitigation, a smaller DC link capacitor can be used. Nevertheless, the parallel P+R controller decreases the phase margin, and it would be interesting to study the overall benefits of the P+R controller in more detail.

3.4 Control system design for the grid converter

The design of the control system for a grid converter is not as straightforward as for a DC/DC converter. This is explained by the fact that the grid converter interfaces with the distribution network, and therefore, has to be synchronized with the grid. The reason to design and implement a grid converter is that the grid converter forms an essential part of the PCU interfacing with the SOFC, and has thus an effect on the system behavior seen by the fuel cell stack. In this section, the grid synchronization, the current controller, and the DC link voltage controller are designed.

3.4.1 Grid synchronization

The grid synchronization is necessary when operating a grid-tied converter. The grid synchronization is used to extract the phase angle of the grid, and to monitor the grid frequency in the case of abnormal operation. The phase information is used to synchronize the switching of the power devices, to calculate and control the power flow, or to transform the feedback into a suitable form.

The simplest way to extract the phase angle is to calculate an *arctan* function from the $\alpha\beta$ coordinates, but this is very vulnerable to grid disturbances. Therefore, a Phase-Locked Loop (PLL) is generally used to synchronize the converter to the grid.

Plenty of different PLL algorithms are available with different benefits and drawbacks. Timbus et al. (2005) have reviewed the synchronization methods for a distributed power generation system, and provide a comparative analysis of the PLL algorithms. The comparison is presented in Table 3.7.

Timbus et al. (2005) suggest that if the algorithm is used only to synchronize the control variables to the grid, slow dynamics can be used. If the PLL algorithm is used to monitor a utility grid, fast dynamics is

Table 3.7. Comparison of the synchronization algorithms (Timbus et al., 2005).

Algorithm	Strong points	Weak points
dqFilter (with DSC)[a]	simplicity	frequency shift variations
$\alpha\beta$Filter	simplicity	unbalanced grid
dqPLL	works for every grid type, provides ride-through capability	slow dynamics
adaptivePLL	estimates amplitude, frequency, and phase angle	complex structure

[a] Delay Signal Cancellation (DSC)

needed. Because the grid faults are beyond the scope of this study, and the speed of the DSP is not an issue, a dqPLL algorithm is chosen.

Kaura and Blasko (1997) suggest a dqPLL algorithm for utility applications, and present the PLL system as a pure control problem. This approach provides a straightforward method for the tuning of the dqPLL. A control diagram for dqPLL is presented in Fig. 3.12.

The basic principle of the dqPLL is that the phase voltages are transformed into $\alpha\beta$ scoordinates, which are then transformed into synchronous dq coordinates with respect to the estimated phase angle θ^*. The estimated phase angle θ^* is obtained by integrating the estimated grid frequency ω^*. The feed-forward term ω_{ff} can be used to feed the assumed grid frequency to the system, and possibly to decrease the time of obtaining the grid synchronization. This improvement requires valid presumption. Because the time of obtaining the grid synchronization is not important in this application, the feedforward term is not used.

The algorithm uses a PI controller to obtain an angular frequency ω^*. The estimate of the phase angle θ^* is used to calculate a feedback signal from the vector $\mathbf{v}_{2,\alpha\beta}$. The algorithm provides a lock to the arbitrary phase angle θ^* with respect to the phase angle θ of the grid.

The error $\Delta\theta^*$ between the phase angle θ and the estimated phase angle θ^* is a function of $V = |v_{\text{d,e}}^{\text{ref}}|$. By modifying the variables of (Kaura and Blasko, 1997), the error can be defined by

$$\begin{bmatrix} v_{2,\text{d}} \\ v_{2,\text{q}} \end{bmatrix} = V \begin{bmatrix} \cos(\theta^* - \theta) \\ \sin(\theta^* - \theta) \end{bmatrix} = \begin{bmatrix} \cos(\Delta\theta) \\ \sin(\Delta\theta) \end{bmatrix}. \tag{3.23}$$

From Equation (3.23) we can see that by setting the reference $v_{\text{d,e}}^{\text{ref}}$ to zero, the lock to the utility can be obtained without a need for the magnitude knowledge of the utility voltage.

Based on the assumption that $\sin(\Delta\theta)$ behaves linearly for small values of the $\Delta\theta$ term, the dqPLL can be approximated by a linear system, where the grid voltage V appears as a gain when the plant is an integrator. The schematic of the dqPll is presented in Fig. 3.13.

Tuning of the PLL

By approximating the system with the linear model presented in Fig. 3.13, the dqPLL can be approached as a gain determination problem (Kaura and Blasko, 1997). By observing the discretization delay, the

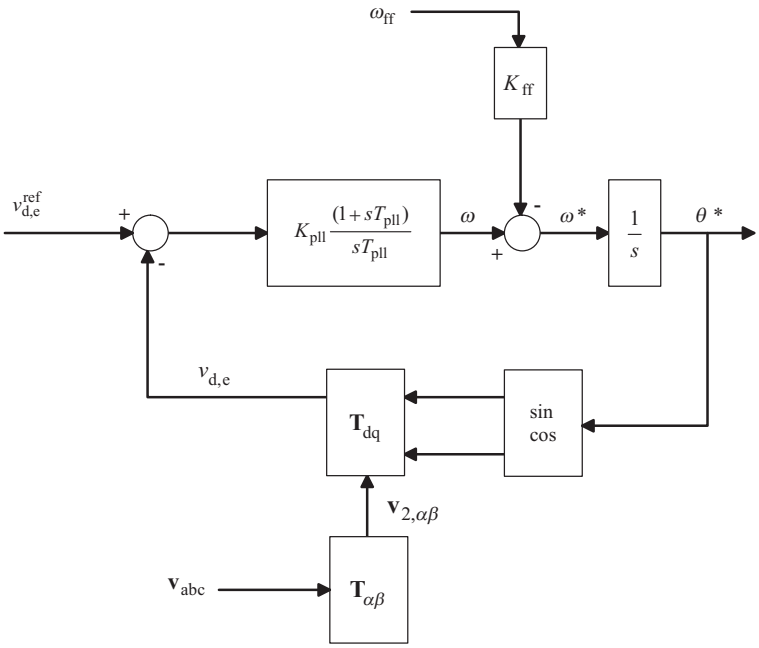

Figure 3.12. Control diagram of the dqPLL (Kaura and Blasko, 1997; Timbus et al., 2005).

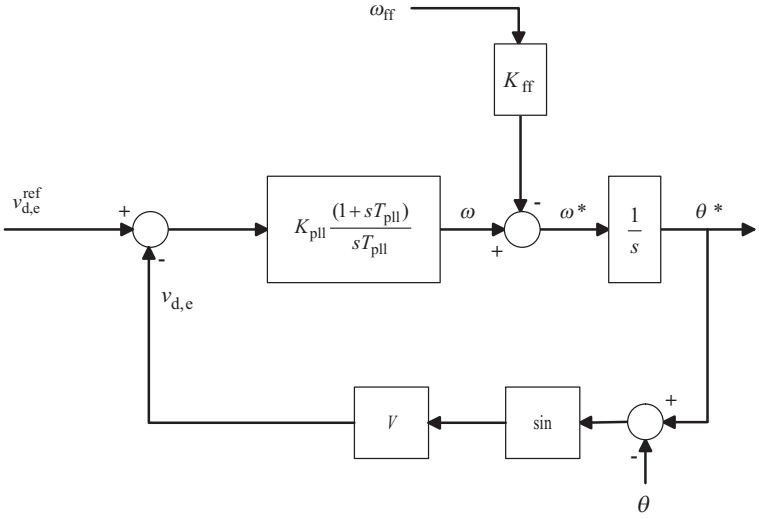

Figure 3.13. Simplified model of the dqPLL (Kaura and Blasko, 1997).

Table 3.8. Parameters of the dqPLL used in the prototype.

α	ω_c	ξ	K_{pll}	T_{pll}
14	56.8 Hz	6.5	1.0989	0.0392

system can be modeled as a first-order lag and integrator:

$$G_{pll,plant} = \left(\frac{1}{1+sT_{s1}}\right)\left(\frac{V}{s}\right), \tag{3.24}$$

where T_{s1} is the sampling period of the DSP presented in Table 3.1. From Fig. 3.13, the open-loop transfer function can be written as

$$G_{pll,ol} = \underbrace{\left(K_{pll}\frac{1+sT_{pll}}{sT_{pll}}\right)}_{\text{PI-controller}}\underbrace{\left(\frac{1}{1+sT_{s1}}\right)}_{\text{lag}}\underbrace{\left(\frac{V}{s}\right)}_{\text{integrator}}, \tag{3.25}$$

where K_{pll} and T_{pll} are the parameters of the PI controller. According to Kaura and Blasko (1997), the control problem is similar to a current-controlled speed loop of a drive system.

The parameters for the PI controller can be determined by the symmetrical optimum method (Leonhard, 2001). By defining the normalizing factor α, it is possible to determine the relation between α, the crossover frequency ω_c, K_{pll}, and T_{pll}

$$\omega_c = \frac{1}{\alpha T_{s1}} \tag{3.26a}$$

$$T_{pll} = \alpha^2 T_{s1} \tag{3.26b}$$

$$K_{pll} = \left(\frac{1}{\alpha}\right)\left(\frac{1}{VT_{s1}}\right) \tag{3.26c}$$

By substituting Equations (3.26a), (3.26b), and (3.26c) to (3.25), it can be noticed that the damping factor ξ and the normalizing factor α have a relation

$$\xi = \frac{\alpha - 1}{2} \tag{3.27}$$

We can see that by modifying the α-parameter, the system bandwidth ω_c and the damping factor ξ can be controlled. By substituting the sampling period T_{s1} from Table 3.1 to Equations (3.26a) and (3.27), the relation can be plotted in Fig. 3.14. By setting $\alpha = 14$, the parameters presented in Table 3.8 can be obtained.

Discrete implementation

To implement the dqPLL with the DSP, the system has to be discretized. The discretization is carried out with a bilinear transform, because it maintains the system stability. By substituting Equation (1.19) into the controller part of Equation (3.25), the controller can be written as

$$G_{pll}(z) = 1 + \frac{T_{s1}(z+1)}{2T_{pll}(z-1)}. \tag{3.28}$$

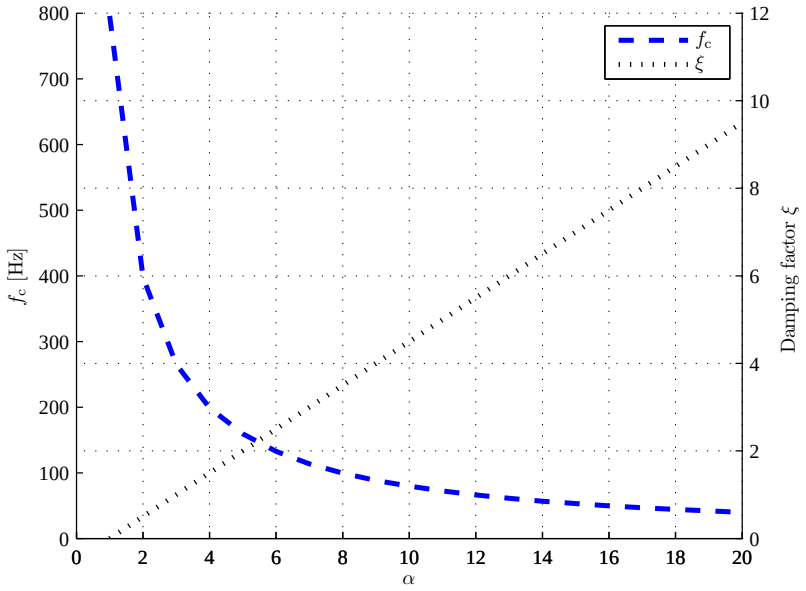

Figure 3.14. Relation between the normalizing factor α, the damping factor ξ , and the crossover frequency ω_c.

and the integrator as

$$G_i(z) = \frac{T_{s1}V(z+1)}{2(z-1)}. \tag{3.29}$$

3.4.2 Current control

Harnefors and Nee (1998) have introduced an internal model control (IMC) based method for the AC machine current control. The method operates in the synchronous reference frame with PI controllers. The parameters for the PI controllers are expressed directly in certain machine parameters and in the desired closed-loop bandwidth. This makes the control design quite a straightforward process, and the IMC is considered a robust control method (Harnefors and Nee, 1998).

The IMC-based method can be applied to control a three-phase VSI converter. Because in this doctoral thesis the current control of the three-phase VSI is not the major research topic, the usage of the IMC method can be justified by its easy control design to obtain the desired bandwidth without additional design efforts. Nevertheless, the IMC method needs grid-voltage feed forward and cross-coupling terms. Next, the IMC-based control design method is introduced in brief based on Harnefors and Nee (1998).

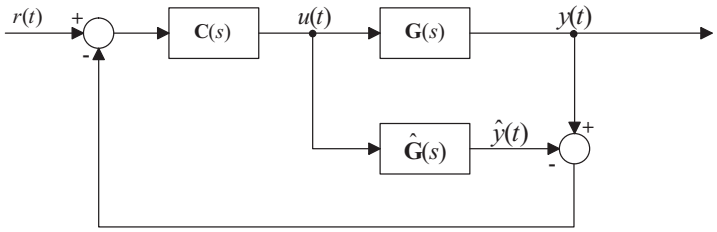

Figure 3.15. Structure of the IMC controller.

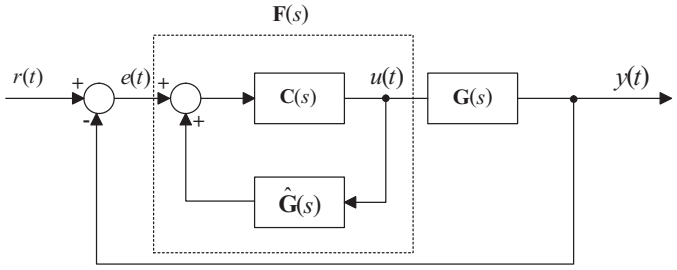

Figure 3.16. Schematic of the IMC controller considered as a special case of the classic controller.

IMC control

The schematic of IMC controller, originally developed for chemical engineering applications, is presented in Fig. 3.15.

The IMC method applies an internal process model $\hat{\mathbf{G}}(s)$ in parallel to the actual process $\mathbf{G}(s)$. The control block in the closed loop is $\mathbf{C}(s)$, which is called the IMC controller. $\mathbf{G}(s)$, $\hat{\mathbf{G}}(s)$, and $\mathbf{C}(s)$ are all transfer function matrices because of the plant is a MIMO system (multiple-in, multiple-out). The IMC method has a couple of noteworthy characteristics:

1. IMC can be considered a special case of the classical control structure presented in Fig. 3.16. The controller $\mathbf{F}(s)$ has a relation to the internal model $\hat{\mathbf{G}}(s)$, which can be expressed as

$$\mathbf{F}(s) = \left[\mathbf{I} - \mathbf{C}(s)\hat{\mathbf{G}}(s)\right]^{-1}\mathbf{C}(s), \tag{3.30}$$

where $\mathbf{I}$ is the identity matrix. Thus, the control signal can be written as

$$\mathbf{U}(s) = \mathbf{F}(s)(\mathbf{R}(s) - \mathbf{Y}(s)). \tag{3.31}$$

To obtain the integral action and zero steady-state error,

$$\mathbf{I} - \mathbf{C}(0)\hat{\mathbf{G}}(0) = 0 \tag{3.32}$$

has to be true. Therefore,

$$\mathbf{C}(0)\hat{\mathbf{G}}(0) = \mathbf{I}. \tag{3.33}$$

2. It can be noticed that if the internal model is perfect, that is, $\hat{\mathbf{G}}(s)$=$\mathbf{G}(s)$, the feedback signal in Fig. 3.15 becomes zero and the closed-loop system can be presented by

$$\mathbf{G}_{\mathrm{c}}(s) = \mathbf{G}(s)\mathbf{C}(s). \tag{3.34}$$

Thus, the system can be considered stable if and only if $\mathbf{G}(s)$ and $\mathbf{C}(s)$ are stable. This means that we have found all the stabilizing controllers $\mathbf{F}(s)$ for the stable plant $\mathbf{G}(s)$. In this case, it would be tempting to apply inverse dynamics and set $\mathbf{C}(s) = \mathbf{G}(s)^{-1}$, which would lead to $\mathbf{G}_{\mathrm{c}}(s)$=$\mathbf{I}$. In this case, all the system dynamics would be canceled and the plant output would instantly follow the reference.

It is obvious that the system described above cannot be implemented for the following reasons:

(a) If the plant $\mathbf{G}(s)$ is a nonminimum phase system, that is, $\mathbf{G}(s)$ has zeros in the right half plane (RHP), $\mathbf{G}(s)^{-1}$ becomes unstable.

(b) $\mathbf{G}(s)^{-1}$ is rarely proper, that is, the degree of the numerator is higher than the degree of the denominator, and $\mathbf{G}(s)^{-1}$ cannot be implemented.

(c) If the plant dynamics is canceled, the control signals need to have a large magnitude.

(d) The method is vulnerable to modeling errors.

Nevertheless, the idea can be implemented with a few modifications. First, $\mathbf{G}(s)$ has to be factored

$$\mathbf{G}(s) = \mathbf{G}_{\mathrm{A}}(s)\mathbf{G}_{\mathrm{M}}(s), \tag{3.35}$$

where $\mathbf{G}_{\mathrm{A}}(s)$ is the allpass portion of $\mathbf{G}(s)$, which includes all the RHP zeros and delays. After factorizing the plant transfer function matrix, the controller can be defined as

$$\mathbf{C}(s) = \mathbf{G}_{\mathrm{M}}(s)^{-1}, \tag{3.36}$$

This factorization solves only the first problem of the above list. Therefore, the controller has to be detuned with the low-pass filter

$$\mathbf{C}(s) = \mathbf{G}_{\mathrm{M}}(s)^{-1}\mathbf{L}(s), \tag{3.37}$$

where

$$\mathbf{L}(s) = diag\left[\frac{\alpha_1^n}{(s+\alpha_1)^n}, \frac{\alpha_2^n}{(s+\alpha_2)^n}, \cdots, \frac{\alpha_{ny}^n}{(s+\alpha_{ny})^n}\right], \tag{3.38}$$

where the integer n has to be chosen large enough to make $\mathbf{C}(s)$ appropriate. Now, the closed-loop system can be made arbitrarily robust by decreasing α_i.

Controller design

Harnefors and Nee (1998) used the IMC method to design a current controller for the PMSM (Permanent Magnet Synchronous Machine). With the following assumptions, the suggested method can be used to design a current controller for a VSI with an LCL grid filter:

- LCL filter behaves in the controller bandwidth like a L-type filter, and
- the filter resonance frequency is not in the vicinity of the switching frequency and the sidebands of the switching frequency.

The inductance used in the control design is the converter-side inductance of the LC filter L_1, because the grid-side inductance L_2 is formed by the grid configuration. Because the L-filter approximation of the LCL filter does not include RHP (Right Half Plane) zeros and behaves like a first-order system at high frequencies, we can write

$$\mathbf{C}(s) = \mathbf{G}(s)^{-1}\mathbf{L}(s), \tag{3.39}$$

where all diagonal elements for $\mathbf{L}(s)$ can be chosen equal

$$\mathbf{L}(s) = \frac{\alpha}{s+\alpha}\mathbf{I}, \tag{3.40}$$

which means that $n = 1$ in Equation (3.38).

This is the benefit of using the IMC method. A control problem including the PI controllers with two parameters per controller simplifies into a form where the only design parameter is the desired controller bandwidth α.

If an assumption is made that $\mathbf{G}(s)$=$\hat{\mathbf{G}}(s)$, the equivalent classical controller presented in Fig. 3.16 can be written as

$$\begin{aligned}\mathbf{F}(s) &= \mathbf{C}(s)\left[\mathbf{I} - \mathbf{C}(s)\mathbf{G}(s)\right]^{-1} = \left[\mathbf{G}(s)^{-1}\frac{\alpha}{s+\alpha}\mathbf{I}\right]\left[\mathbf{I} - \mathbf{G}(s)^{-1}\frac{\alpha}{s+\alpha}\mathbf{I}\mathbf{G}(s)\right]^{-1} \\ &= \left[\mathbf{I} - \frac{\alpha}{s+\alpha}\mathbf{I}\right]^{-1}\mathbf{G}(s)^{-1}\frac{\alpha}{s+\alpha} \\ &= \frac{\alpha}{s}\mathbf{G}(s)^{-1}\end{aligned} \tag{3.41}$$

If the LCL filter is approximated with the L-filter presented in Equation (1.16), and the grid-side voltages are neglected, the plant transfer function matrix $\mathbf{G}(s)$ can be written as

$$\mathbf{G}(s) = \frac{1}{(R_{\mathrm{L}1} + L_1 s)^2 + \omega^2 L_1^2}\begin{bmatrix} R_{\mathrm{L}1} + L_1 s & \omega L_1 \\ -\omega L_1 & R_{\mathrm{L}1} + L_1 s \end{bmatrix}, \tag{3.42}$$

and thus, the inverse transfer function matrix yields

$$\mathbf{G}(s)^{-1} = \begin{bmatrix} sL_1 + R_{\mathrm{L}1} & -\omega L_1 \\ \omega L_1 & sL_1 + R_{\mathrm{L}1} \end{bmatrix}. \tag{3.43}$$

By substituting Equation (3.43) to (3.41) we obtain

$$\mathbf{F}(s) = \frac{\alpha}{s}\mathbf{G}(s)^{-1} = \alpha\begin{bmatrix} L_1\left(1 + \frac{R_{\mathrm{L}1}}{sL_1}\right) & -\frac{L_1\omega}{s} \\ \frac{L_1\omega}{s} & L_1\left(1 + \frac{R_{\mathrm{L}1}}{sL_1}\right) \end{bmatrix}. \tag{3.44}$$

If Equation (3.44) is compared with the diagonal form of the PI controller

$$\mathbf{F}_{\mathrm{pi}}(s) = \begin{bmatrix} K\left(1 + \frac{1}{sT_{\mathrm{i}}}\right) & 0 \\ 0 & K\left(1 + \frac{1}{sT_{\mathrm{i}}}\right) \end{bmatrix}, \tag{3.45}$$

we obtain

$$K = \alpha L_1, \tag{3.46a}$$

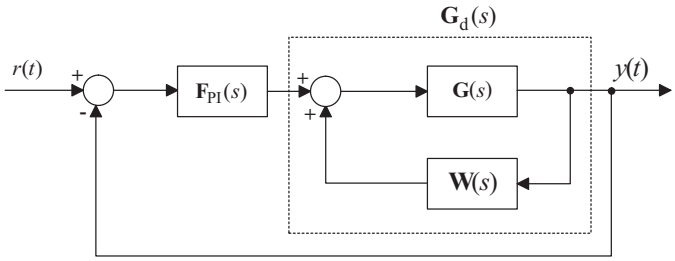

Figure 3.17. DIMC method to decouple the dynamics of the d- and q-axes. The decoupling is made by the 'inner feedback loop', where the decoupling matrix **W** is used to decouple the axis. This modification makes it possible to use the standard PI controller.

$$T_\mathrm{i} = \frac{L_1}{R_{\mathrm{L}1}} \Leftrightarrow \tag{3.46b}$$

$$K_\mathrm{i} = \alpha R_{\mathrm{L}1}. \tag{3.46c}$$

Harnefors and Nee (1998) propose the Decoupling and Diagonal IMC (DIMC) method to decouple the dynamics of the d- and q-axes. This decoupling is made by introducing an 'inner feedback loop', shown in Fig. 3.17. The inverse transfer function matrix $\mathbf{G}(s)^{-1}$ (3.43) can be divided into diagonal and antidiagonal parts, which yields

$$\mathbf{G}(s)^{-1} = \underbrace{\begin{bmatrix} sL_1 + R_{\mathrm{L}1} & 0 \\ 0 & sL_1 + R_{\mathrm{L}1} \end{bmatrix}}_{\mathbf{D}(s)} + \underbrace{\begin{bmatrix} 0 & -\omega L_1 \\ \omega L_1 & 0 \end{bmatrix}}_{\mathbf{W}}. \tag{3.47}$$

By introducing the decoupling terms in the 'inner feedback loop', and taking into account the definition of the diagonal and antidiagonal parts, the plant $\mathbf{G}_\mathrm{d}(s)$ can be written as

$$\begin{aligned} \mathbf{G}_\mathrm{d}(s) &= \mathbf{G}(s)\left[\mathbf{I} - \mathbf{G}(s)\mathbf{W}\right]^{-1} = \left[\mathbf{G}(s)^{-1} - \mathbf{W}\right]^{-1} \\ &= \mathbf{D}(s)^{-1} = \begin{bmatrix} \frac{1}{L_1 s + R_{\mathrm{L}1}} & 0 \\ 0 & \frac{1}{L_1 s + R_{\mathrm{L}1}} \end{bmatrix}. \end{aligned} \tag{3.48}$$

This modification makes it possible to use a standard PI controller in the outer feedback loop in the method for parameter selection as in the case of the IMC method (3.46)).

Digital implementation

As presented above, the IMC method is generally considered stable. However, the $\mathbf{F}_\mathrm{pi}(s)$ part of the controller can induce ripple to the response. In particular, in digital systems, digital delays constitute an important factor in the control loop, and thereby affect the controller design.

The DSVPWM (Digital Space Vector Pulse Width Modulation) worst-case delay is approximated by

$$\mathbf{G}_\mathrm{dsvpwm}(s) = e^{-s\tau}\mathbf{I}, \tag{3.49}$$

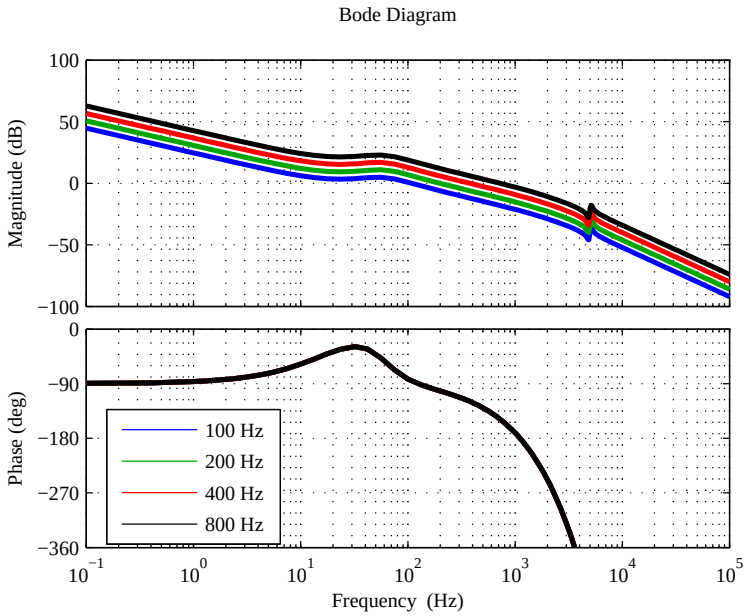

Figure 3.18. Sweep of the d-axis of the IMC controller. The figure shows that the phase and gain margins decrease when the bandwidth increases. The problem with this decrease arises when the model differs from the plant, and the PI controller has to drive the model error to zero.

where τ is the switching period of the DSVPWM modulator.

In addition, an AA filter must be taken into account when operating in the discrete domain. An AA filter can be presented as in the DC/DC stage (3.3), but for the sake of convenience, the AA filter is expressed here in a matrix form. The AA filter can be written as

$$\mathbf{H}(s) = \frac{K_\mathrm{s}}{1+\frac{s}{\omega_0}}\mathbf{I}, \tag{3.50}$$

where ω_0 is the desired crossover frequency in rad/sec and K_s is the sensing gain. In this case, we may set K_s=1 because the feedback signal is scaled back to real values.

From Fig. 3.17 and Equations (3.49) and (3.50), the loop gain can be written as

$$\mathbf{T}_\mathrm{gd}(s) = \mathbf{F}_\mathrm{pi}(s)\mathbf{G}_\mathrm{dsvpwm}(s)\mathbf{G}_\mathrm{d}(s)\mathbf{H}(s). \tag{3.51}$$

Current loop bandwidth selection

The function of the PI controller is to drive the model error to the zero. From Equation (3.51) it is possible to plot the Bode diagrams for the controller. The Bode diagrams of Equation (3.51) are plotted in Fig. 3.18.

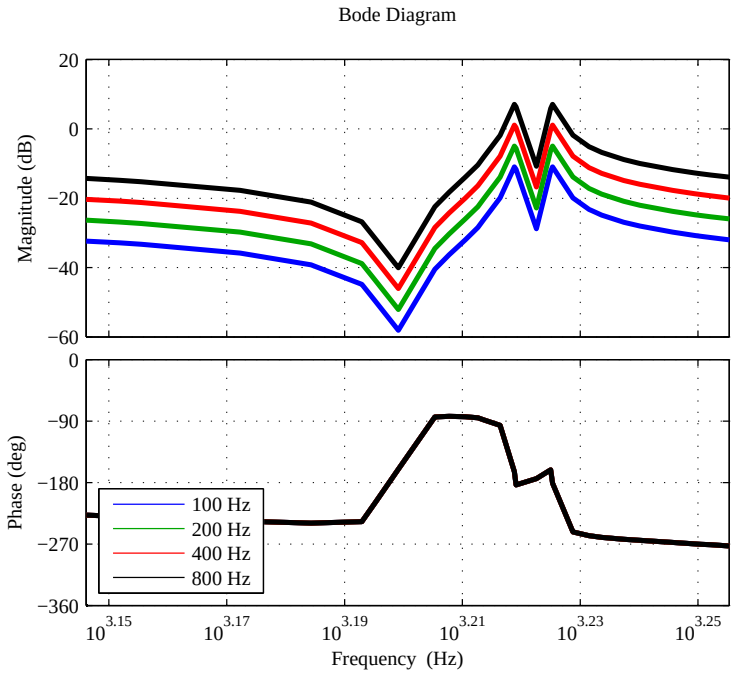

Figure 3.19. Loop gains of the d-axis of the discrete IMC controller with L_2=0.936 mH, with the part of the most interest emphasized. The figure shows that the gain at the resonance frequency (approx. 1700 Hz) increases over 0 dB, and it would be considered unstable in terms of traditional control design.

If the grid inductance L_2 is increased to 0.936 mH and the grid resistance R_{L2} is decreased to 0.1605 Ω, and the Bode sweeps are replotted (Fig. 3.19), it can be noticed that the gain peak of the 800 Hz loop gain is over 0 dB, and the frequency is below the Nyquist frequency. This leads to the conclusion that the system would be considered unstable in the conventional methods.

Based on the analysis made on Fig. 3.19, the step responses with the corresponding controller bandwidths are presented in Fig. 3.20. In the figure, an increase in the ripple component at 800 Hz can be detected. Based on the previous analysis, the bandwidth for the IMC controller is set to 400 Hz, which provides an acceptable compromise between the stability and the performance. When compared with the suggestions made in (Harnefors and Nee, 1998), the chosen bandwidth satisfies the proposed criteria related both to the switching and sampling frequencies. The parameters for the IMC controller are presented in Table 3.9.

Table 3.9. Parameters of the loop gain of the IMC controller. The bandwidth is set to 400 Hz, where the proportional gain and the integral gain are calculated using the corresponding equations (3.46).

α	K_p	K_i
$2\pi 400$	17.6	2211.7

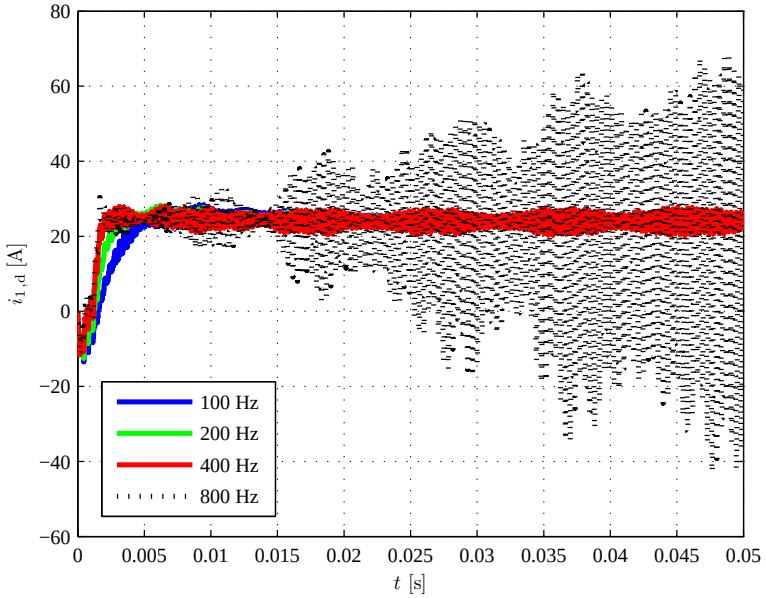

Figure 3.20. Step responses of the simulation model with varying bandwidths and L_2=0.936 mH. The step responses show a ripple component of the 800 Hz controller, which was suggested to be unstable in Fig.3.19.

The digitalization of the controller is straightforward due to the fact that the controller is a general PID controller. Therefore, a general PID implementation can be used.

Limiting the reference voltage vector and anti-windup

The reference voltage of the grid converter that exceeds the voltage capability of the converter has to be limited. Ottersten and Svensson (2002) have reviewed several methods to limit the reference voltage vector. It is stated that the Space Vector Limit method (SVL) is suitable to be used with the SVPWM. Because of its suitability, the SVL method is chosen to limit the reference vector. However, the anti-windup method is not in the focus of this study, and therefore, a detailed analysis is not provided here.

3.4.3 DC link voltage controller

The DC link voltage control diagram consists of a series of transfer functions. $G_{\mathrm{pi}}(s)$ is the DC link voltage controller, $G_{\mathrm{cc}}(s)$ is the line converter current controller, where the closed-loop system is lumped into a single transfer function, and $G_{\mathrm{IdVdc}}(s)$ is the transfer function from the d-component of the converter current to the DC link voltage (Teodorescu et al., 2011). The DC link voltage control diagram is presented in Fig. 3.21.

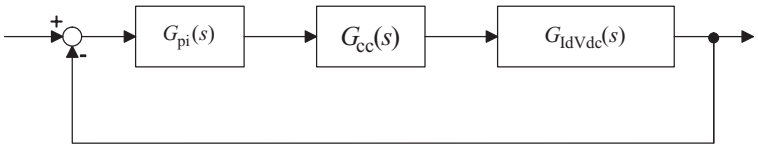

Figure 3.21. DC link voltage control diagram. The IMC-based current controller is approximated with the first-order lag, and the DC link equivalent resistance is calculated with the corresponding value of the 100 A operating point of the DC/DC converter.

The DC link can be modeled by applying the energy of the DC link capacitor. The power balance of the capacitor can be written as

$$\frac{3}{2}\left(v_{1,\mathrm{d}}i_{1,\mathrm{d}}+v_{1,\mathrm{q}}i_{1,\mathrm{q}}\right)=-V_{\mathrm{dc}}C_{\mathrm{dc}}\frac{\mathrm{d}}{\mathrm{d}t}V_{\mathrm{dc}}+V_{\mathrm{dc}}i_{\mathrm{dc}}. \tag{3.52}$$

The next step is to perturb Equation (3.52), taking into account that the product of two perturbations is ≈ 0, and the derivative of the steady-state value is 0. Noticing that in the steady state

$$\frac{3}{2}\left(v_{1,\mathrm{d}}i_{1,\mathrm{d}}+v_{1,\mathrm{q}}i_{1,\mathrm{q}}\right)=V_{\mathrm{dc}}i_{\mathrm{dc}}, \tag{3.53}$$

the equation can be written as:

$$\frac{3}{2}\left(v_{1,\mathrm{d}}\tilde{i}_{1,\mathrm{d}}+\tilde{v}_{1,\mathrm{d}}i_{1,\mathrm{d}}+v_{1,\mathrm{q}}\tilde{i}_{1,\mathrm{q}}+\tilde{v}_{1,\mathrm{q}}i_{1,\mathrm{q}}\right)=-V_{\mathrm{dc}}C_{\mathrm{dc}}\frac{\mathrm{d}}{\mathrm{d}t}\tilde{v}_{\mathrm{dc}}+V_{\mathrm{dc}}\tilde{i}_{\mathrm{dc}}+\tilde{v}_{\mathrm{dc}}i_{\mathrm{dc}}. \tag{3.54}$$

By defining the steady-state equivalent resistance

$$R_{\mathrm{dc,eq}}=\frac{V_{\mathrm{dc}}}{i_{\mathrm{dc}}}, \tag{3.55}$$

and by approximating $V_{\mathrm{dc}}\approx\sqrt{3}v_{1,\mathrm{d}}$, we can derive the transfer function from (3.54)

$$G_{\mathrm{IdVdc}}(s)=\frac{\tilde{v}_{\mathrm{dc}}(s)}{\tilde{i}_{1,\mathrm{d}}(s)}=\frac{\sqrt{3}}{2}\frac{R_{\mathrm{dc,eq}}}{R_{\mathrm{dc,eq}}C_{\mathrm{dc}}s-1}. \tag{3.56}$$

The PI controller is chosen as the voltage controller. The PI controller can be written as

$$G_{\mathrm{pi}}(s)=K_{\mathrm{p}}\left(\frac{1+T_{\mathrm{i}}s}{T_{\mathrm{i}}s}\right). \tag{3.57}$$

The IMC controller of the grid converter is approximated with the first-order lag

$$G_{\mathrm{cc}}(s)=\frac{1}{1+s\tau_{\mathrm{cc}}}, \tag{3.58}$$

where

$$\tau_{\mathrm{cc}}=\frac{1}{2\pi f_{\mathrm{cc}}}=\frac{1}{\alpha}. \tag{3.59}$$

From Equations (3.56), (3.57), and (3.58), we get the open-loop transfer function

$$G_{\mathrm{ol}}(s)=\frac{\sqrt{3}K_{\mathrm{p}}R_{\mathrm{dc,eq}}(1+T_{\mathrm{i}}s)}{2T_{\mathrm{i}}s(1+\tau_{\mathrm{cc}})R_{\mathrm{dc,eq}}C_{\mathrm{dc}}s-2T_{\mathrm{i}}s(1+\tau_{\mathrm{cc}})}. \tag{3.60}$$

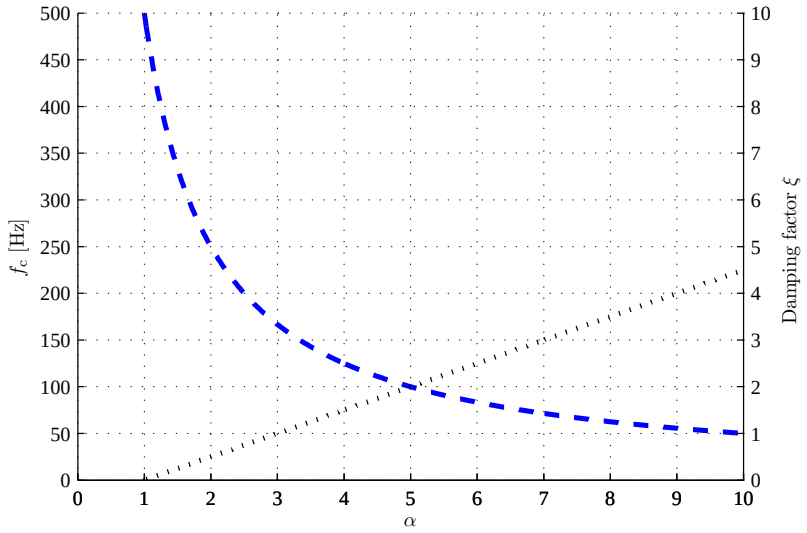

Figure 3.22. Bandwidth (f_c) and damping factor (ξ) of the DC link voltage controller as a function of normalizing factor α with the equivalent resistance set to the corresponding value of the operating point of 100 A.

Because $R_{dc,eq}C_{dc} >> \tau_{cc}$, the second term of the denominator can be neglected, which leads to

$$G_{ol}(s) \approx \frac{\sqrt{3}K_p(1+T_i s)}{2T_i s(1+\tau_{cc})C_{dc}s}. \tag{3.61}$$

If we compare (3.61) with (3.25), we notice a similarity between the two plants. Based on this and the fact that a symmetrical optimum is commonly used to tune the transfer functions containing two integrators, with the controller included, we use the same tuning method as with the PLL. For the sake of convenience, equations for the controller parameters are presented:

$$\omega_c = \frac{1}{\alpha\tau_{cc}}, \tag{3.62a}$$

$$T_i = \alpha^2\tau_{cc}, \tag{3.62b}$$

$$K_p = \left(\frac{1}{\alpha}\right)\left(\frac{1}{\frac{\sqrt{3}}{2C_{dc}}\tau_{cc}}\right). \tag{3.62c}$$

Similarly as in the tuning of the PLL, the DC link controller bandwidth and the damping factor can be presented as a function of α, presented in Fig. 3.22. We can see that the controller is unstable when $\alpha < 1$, critically damped $\alpha = 1$, underdamped when $1 < \alpha < 3$, and overdamped when $\alpha \geq 3$.

Because the system is designed for distributed generation, there are no significant dynamical requirements for the voltage controller, and the area of $\alpha \geq 3$ is of the most interest. Moreover, because the DC link fluctuation should not be seen at the cell, a significantly lower bandwidth compared with the DC/DC current controller is desired (Liu and Lai, 2007). This justifies the large α, and thus, the low bandwidth.

The digital delay is neglected in the DC link voltage controller design. This can be explained by the fact that the calculation and modulator delays are lumped in $G_{cc}(s)$. Thus, the delays of the digital controller do not affect the voltage controller design (Buso and Mattavelli, 2006). Nevertheless, the limit cycling phenomena can still be present if the conditions described above are not met.

3.4.4 Conclusion on the grid converter control system design

As stated above, an in-depth analysis of the grid converter control design was not in the focus of this study. However, the grid converter was built and the control system was designed because the grid converter and the DC link voltage controller constitute an essential part of the PCU dynamics. In the control design of the grid converter, it was noticed that the grid-side inductance can cause instability in the converter, or the switching frequency of the converter can be in the resonance frequency of the combination of the filter and grid. Based on these observations, a more comprehensive analysis of the grid converter would be interesting with the following suggestions for study:

- mitigating the grid current harmonics with the repetitive-based voltage controller (Buso and Mattavelli, 2006),
- grid-side inductance detection, and
- IMC controller stability analysis based on Youla parametrization.

3.5 Practical considerations

When operating with an actual plant, some practical considerations are required. Considering the fuel cell plant, the output current of the plant should not be allowed to change rapidly. To avoid unwanted current spikes caused by the operating environment, a reference current filtering must be added. In addition, the PCU should be able to protect itself in the case of abnormal operation. In the following, the current reference filter and the safety functions are introduced in practice.

3.5.1 Reference current filtering

In a fuel cell plant there can be several sources of EMI. Because disturbances may be included in the reference signal, which should accurately follow the plant controller reference, current setpoint filtering is needed. Because the change in the current of the fuel cell plant is of the order of a couple of amperes per minute, harsh filtering can be used.

A low-pass IIR (Infinite Impulse Response) filter is a commonly used filter and suitable for this case. The reasons for choosing the IIR filter are its easy implementation and the fact that it provides a clear connection between the response and the setup variable. Further, the presented method needs only two memory blocks, and therefore, it provides a suitable method to be used in embedded systems with a restricted memory space.

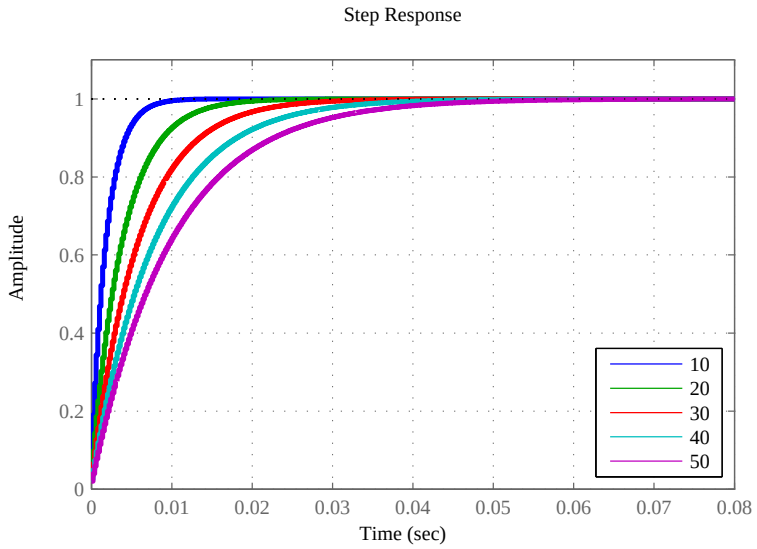

Figure 3.23. Step responses of the low-pass IIR filter (3.63) with a varying time constant (N) with a sampling time of T_s=0.20 ms.

A discrete transfer function for the IIR filter can be written as

$$F_{\text{lp}}(z) = \frac{1}{N-(N-1)z^{-1}}, \tag{3.63}$$

where N is the time constant of the low-pass filter. Step responses of the low-pass filter with a varying N are presented in Fig. 3.23.

3.5.2 Safety functions

The implementation of the control system usually includes a function to protect the converter, and in some cases, an FC stack. The purpose of the safety functions is to prevent the converter from operating in such a region where the malfunction or breakdown is likely. In addition, the line between safe and potentially hazardous operation is not clear-cut. Therefore, some operating regions are safe in a certain period, whereas in some regions, immediate shutdown is required.

When operating with a fuel cell plant, the basic principle of safety functions is that the converter protects only itself, and the BoP protects the stack. Consequently, the following safety functions were implemented in the system:

- stack overvoltage,
- stack overcurrent,
- DC link overvoltage,

- DC link undervoltage, and
- DC link overcurrent.

The requirement for different response times was met with an error-specific counter, the resolution of which is $1/T_{s1}$ [s]. In other words, the response time is nT_{s1}, where $n \in N$.

Chapter 4

Experimental results

4.1 Description of the experiments

Simulations are carried out to ensure that the control design process is successful; in other words, their purpose is to detect possible problems in the process. The basis for the simulation cases can be derived from the requirements of the fuel cell stack, the grid, the steady-state operating of the PCU, and protection of the PCU itself.

A fuel cell plant is a slow process compared with the PCU, and the most important target for the PCU is to maintain the current setpoint submitted by the plant controller. For this reason, the obvious variable to observe is the input current of the PCU.

Based on the brief review of the grid standards, the response to abnormal grid conditions is always to disconnect the plant from the grid. According to this response requirement, a PCU should not exceed the current reference at the moment when the disconnecting occurs. In practice, when disconnecting takes place, the fuel cell plant is not able to continue its normal operation, and it should be driven down safely.

Because the fuel cell stack is sensitive to the low-frequency current component, it was stated that the control system should not generate low-frequency components. Because the control system is digital, and an option to limit the cycling phenomena is recognized, the limit cycling should be observed in the steady-state simulations. Even though a limit cycling may occur, the current ripple should remain within the specifications.

The last source of simulation cases is the necessity to protect the PCU itself. Even though the fuel cell plant should operate safely, it is possible to drift to the unwanted operating point. Usually, when the limits of the safe operating are exceeded, a risk to physical breakdown is significant. Because the PCU must be driven down in a controlled manner, the plant current reference is larger than the input current of the PCU, but this is still a better alternative than a PCU failure and an uncontrolled input current.

Based on the above, the following cases are measured, and when practical, simulated with the designed system:

- Model verification when possible,
- LF ripple mitigation,
- Steady-state limit cycling,
- Disconnection from the grid,
- Fuel cell emergency shutdown, and
- DC/DC converter overcurrent protection

The objectives for the experiments are to ensure that

- an overcurrent situation does not occur in abnormal conditions,
- the PCU remains stable in abnormal conditions, and
- the PCU is able to protect itself.

An accurate correspondence between the model and the measurements is not in the main focus of this work because linearized models are used in the simulations. The moment of fault is more interesting for the reason that a harmful overloading situation is more likely to take place at the moment when an abnormal condition starts.

4.2 Description of the simulation model

The model was implemented in a Matlab/Simulink® environment. The two models for the RPP were used in the simulations. The model of the RPP converter was constructed using the LTI state-space model, and the switching model based on equations described in Section 2.2. The switching model was used to predict the RPP converter operation without a grid converter, while the state-space model, linearized to D=0.4, was used with the grid converter.

The grid filter is presented by a state-space model presented in Section 2.3. A space-vector pulse width modulator is used with the symmetrical modulation scheme (Neacsu, 2006), which means that switching effects are present. The dead-time effect of the grid converter was neglected because it would increase the calculation time, and because the accuracy of the grid converter is assumed adequate for the control design without the dead times.

The digitalization effects are modeled by applying the presented methods. A limit cycling effect is modeled by using the same integer values of the switching counters and the control signals as in the actual implementation with the corresponding quantizers. In addition, the sampling effects are achieved with a sample and hold block, which is synchronized to the beginning of the switching period. This leads to operation where the control value cannot be updated during the switching cycle.

The developed models are presented in Appendix B.

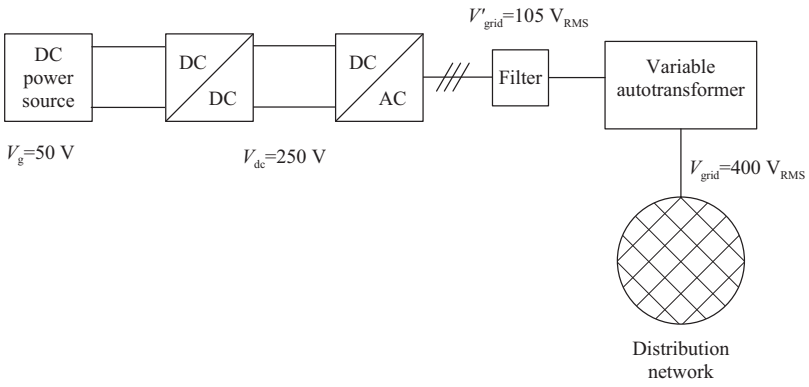

Figure 4.1. Test setup used in the measurements. The DC power source is connected to the DC/DC converter. The DC/DC converter is connected to the grid converter via a DC link. The grid converter is connected to the grid filter, which is connected to a variable autotransformer. The variable autotransformer is used to step down the grid voltage because of the problems with the VSI hardware.

4.3 Description of the measurements

The measurements of the PCU are implemented with the following operating parameters: V_{dc}=250 V, V_g=50 V, I_{lb}=20 A, and V'_{grid}=105 V, the DC link overvoltage trigger=340 V, the DC link breaker on trigger=350 V, and the DC link breaker off trigger=330 V. The reason for the use of the lower voltages and the power level of 1 kW is the problems related to the single switching leg of the VSI. The switching leg fails to operate when the grid voltage rises high enough. At lower power levels, the switching leg does not conduct as much current as the other two legs during the grid period. The reason for this is still under research, but because the control system is not dependent on the power level, and it should operate adequately in all states, the measurements were conducted with the given parameters.

The RPP converter was modified by paralleling two transformers. Modification was made because of the temperature problems with high currents. However, the parallel configuration of transformers does not affect the operation principle of the converter, and a change in the equivalent leakage inductance can be detected in the component values.

The grid voltage was stepped down with a variable autotransformer, which increased the resistance and inductance of the grid. The measurement setup is depicted in Fig. 4.1, and the equipment used in the laboratory setup are presented in Table 4.1. A photo of the test setup is presented in Appendix C. The RPP converter prototype is presented in Fig. 4.2 and the VSI prototype in Fig. 4.3.

Table 4.1. Equipment used in the experimental tests

Equipment	Model
DC power supply	Sorensen SGA60/250C
Oscilloscope	LeCroy LC574A digital Oscilloscope
Current probe(s)	LeCroy AP015
	Fluke 80i-110s
Differential probe	Tektronix P5205
Frequency Response Analyzer (FRA)	Venable Instruments 3120
Multimeter(s)	Fluke 187 true rms digital multimeter

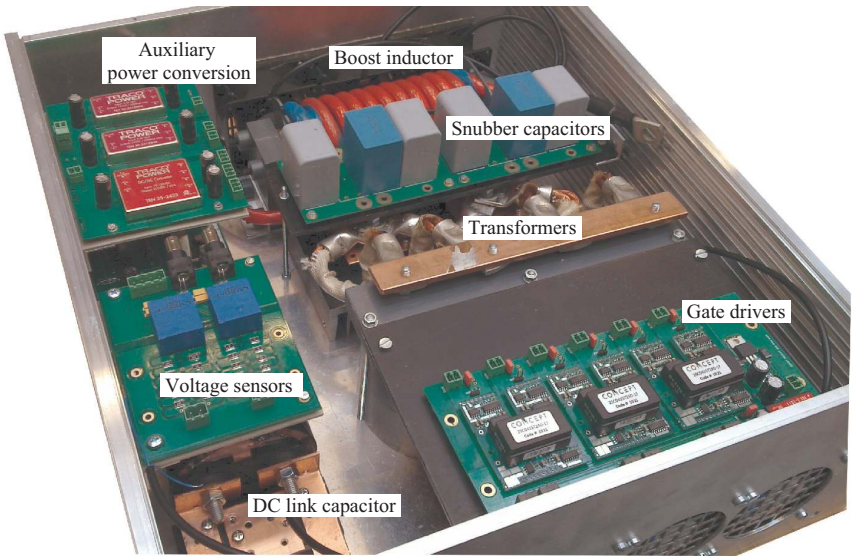

Figure 4.2. DC/DC converter prototype. In the figure, the RPP converter prototype is illustrated without cables. The key components of the converter are indicated in the figure. The DC link capacitor was removed for PCU measurements.

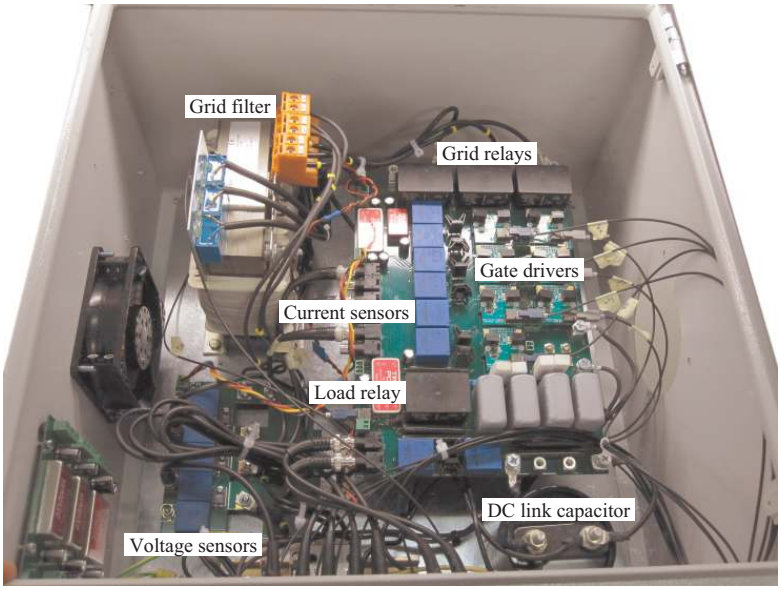

Figure 4.3. VSI developed in the study. The key components of the converter are indicated in the figure.

4.4 Results

The results of the simulations and measurements described above are presented in the following sections. Based on experiments, a summary of the results is presented at the end of the chapter.

4.4.1 Model verification

Because the model is always a simplification of a physical system, the model must be verified against an actual prototype. However, a measurement is also only a prediction of the measured quantity. For this reason, the measured data include some uncertainty. In the following, the models of the DC/DC converter and the grid converter are verified against actual prototypes.

The DC/DC converter is verified in the steady state by measuring the D-I_{lb} and D-V_{dc} curves and comparing the results with the predicted values by the steady-state model. The predicted and measured D-I_{lb} curves are presented in Fig. 4.4a and D-V_{dc} curves in Fig. 4.4b. The duty cycle is captured by the dSpace ControlDesk®, which is a graphics interface between the PC and the dSpace realtime controller. The dSpace is used only as a data capturing device, when the control algorithms are located in the DSP and FPGA. The captured duty cycle does not notice the safety times for the switching leg. By observing the delays, the effective duty cycles were calculated by Equation $D = D_{\mathrm{meas}} - (25/500) = D_{\mathrm{meas}} - 0.05$. The values used in the calculation are based on the actual implementation of the modulator.

The measured values of Fig. 4.4 show that the difference between the model and the measurements starts to increase below D=0.3. A possible reason for this difference is the simplification of the model, where

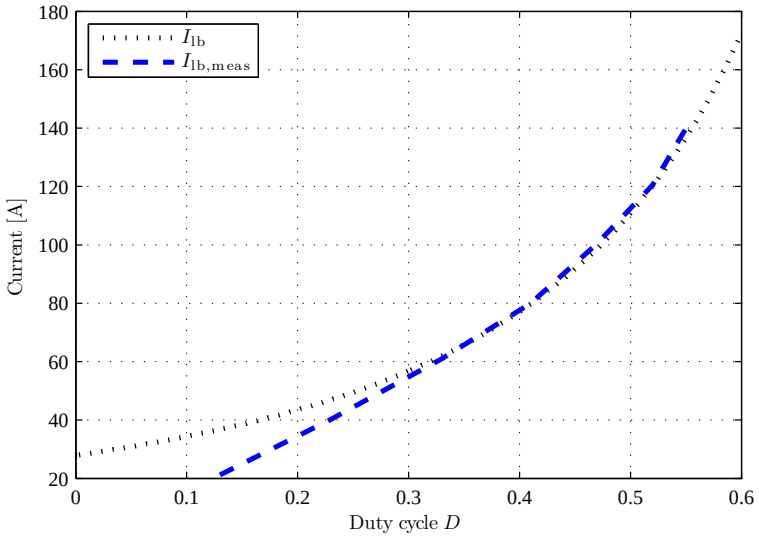

(a) Predicted and measured D-I_{lb} curves.

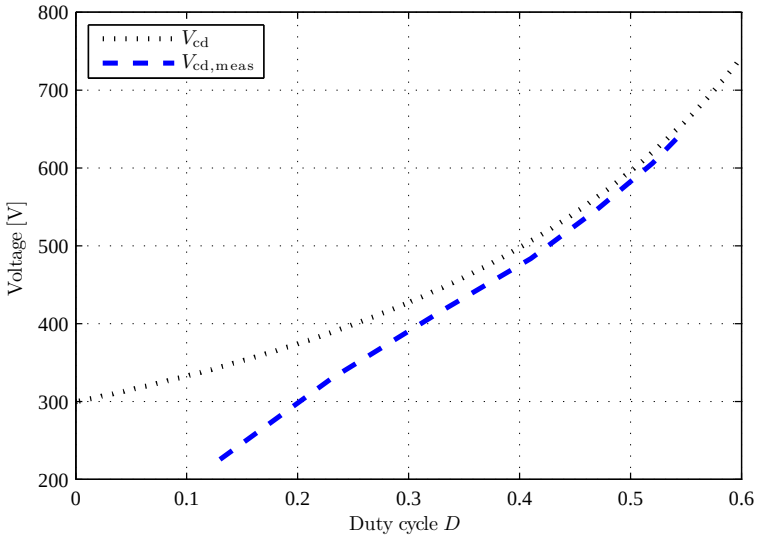

(b) Predicted and measured D-V_{dc} curves.

Figure 4.4. Predicted and measured steady-state operating values. The measured values show that the difference between the model and the measurements starts to increase below D=0.3. A possible reason for this difference is the simplification of the model, where the states t_2 and t_4 are assumed to be equal to the resonance time.

the states t_2 and t_4 are assumed to be equal to the resonance time. Another probable explanation for the difference is the larger proportional influence of the nonidealities at the lower power levels. The total difference is a plausible combination of the both.

The control design of the DC/DC converter is verified with the 0-100 A step response measurement with the PID and also a parallel connection of the PID (Fig. 4.5a) and P+R (Fig.4.5b) controllers. The rise time of the closed-loop plant can be defined for both controllers from the figures.

Based on the rise time of 10–90 %, the bandwidth of the PID controller can be approximated to 600 Hz, while the bandwidth of the parallel connection of the PID and P+R controllers can be approximated to 620 Hz. When observing the specifications of the Sorensen SGA60/250C DC power supply, it can be noticed that the specified typical DC current slew rate is 45 A/ms with a resistive load. Based on this observation, and by the measured step responses, it can be stated that the limiting factor is the slew rate of the DC power supply.

It can be suggested that a FRA should be used to verify the model of the DC/DC converter. However, with the FRA, a suitable current injection point is required, which is problematic when operating with a digital control system of the kind used in this study. Hence, a topic of further studies could be to survey suitable measurement methods for the presented converter with the FRA.

The simulated and measured filter frequency responses are presented in Fig. 4.6. The figure shows that the model-based filter frequency response accurately follows the measured frequency response. Based on this observation, the LC filter model used can be assumed to approximate the actual filter with satisfactory accuracy.

4.4.2 LF ripple mitigation

The LF ripple mitigation was a simulation process implemented by letting the startup transients to settle down and by observing the DC link voltage and the DC/DC converter current. The measurement was carried out by a corresponding method, but the stability of the converter temperature was not observed because it was assumed to be insignificant compared with the measured phenomenon.

Because of the switching frequency ripple, the digital lowpass filtering is made for the DC/DC converter input current I_{lb}. The filtered input current shows more clearly the low-frequency component of the current. The 20th-order lowpass FIR filter was used with a cutoff frequency of 1000 Hz, which is also the suggested boundary cutoff frequency of the harmful and nonharmful ripple components. The simulation is achieved by adding an unbalance to the grid by setting the phase voltages as 95 %, 100 %, and 110 % of the nominal values. The precise modeling of the harmonic content of the laboratory grid was not possible because the harmonic content changed constantly.

The simulated and measured steady-state current ripple with the PID controller is presented in Fig. 4.7, and with the PID and P+R controllers in Fig. 4.8.

Figure 4.7 shows that the amplitude of the DC link voltage fluctuation is larger than in simulations. The amplitude of the LF ripple component was also smaller than in the simulations, which was expected because of the smaller fluctuation of the DC link. The possible reason for the difference of the DC link fluctuation can be the usage of the linearized model or the nonidealities of the system.

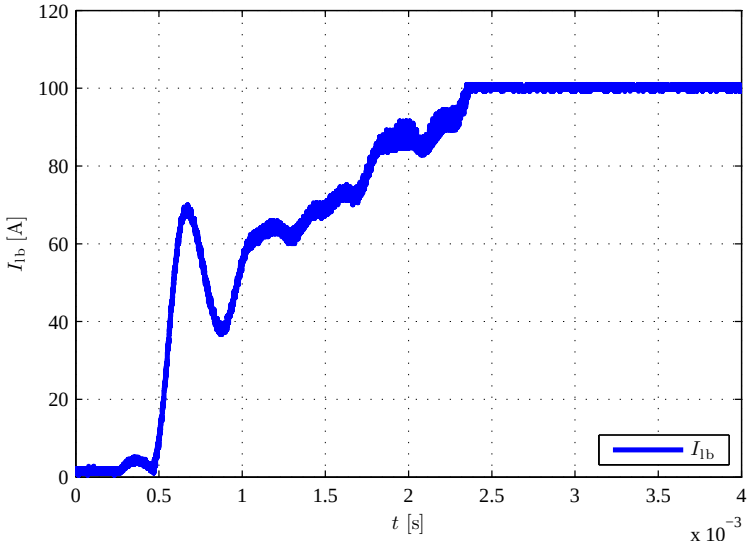

(a) PID controller

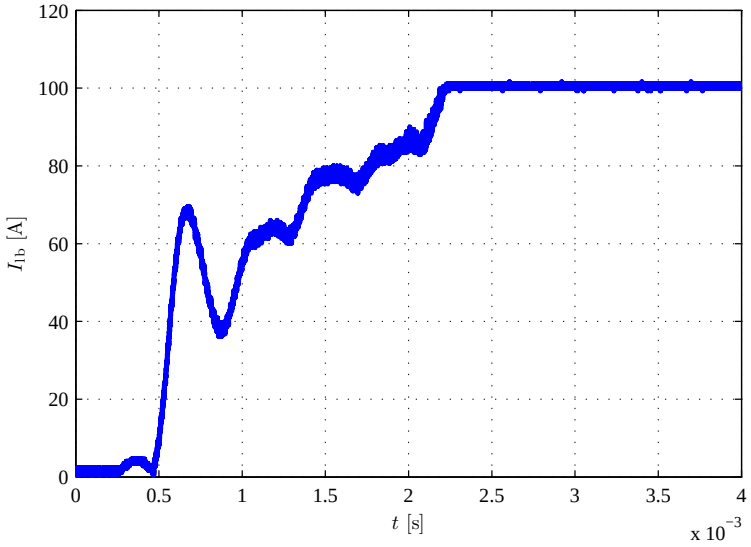

(b) Parallel connection of the PID and P+R controllers

Figure 4.5. DC/DC converter 0-100A step response with a parallel connection of the PID and P+R controllers. The step responses show that the slew rate of the DC power supply limits the step response. Based on the measurement, we may conclude that the system remains stable; however, it is emphasized that the measurement only represents the step response of the system.

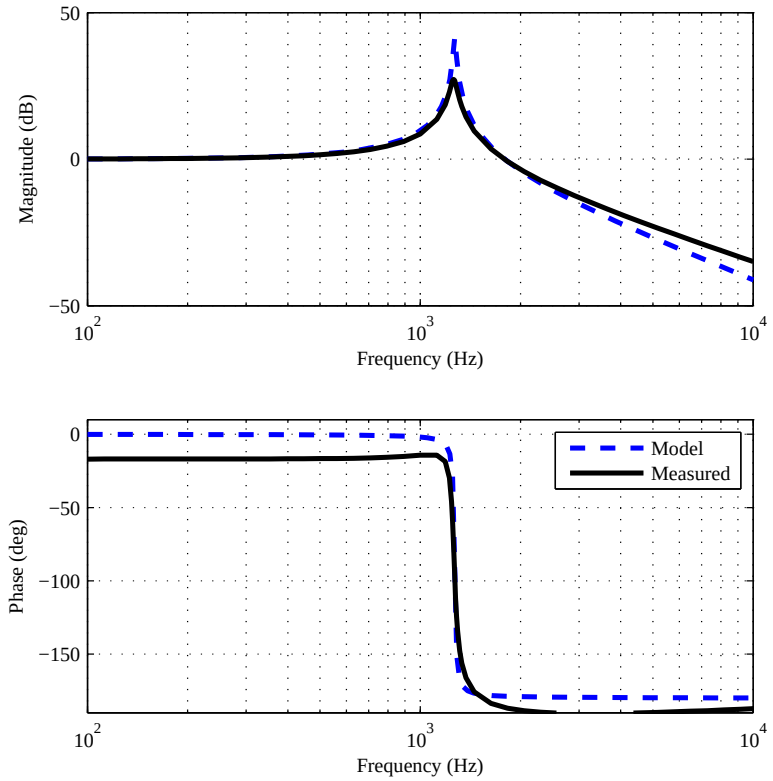

Figure 4.6. Measured and simulated frequency responses from the input voltage to the output voltage.

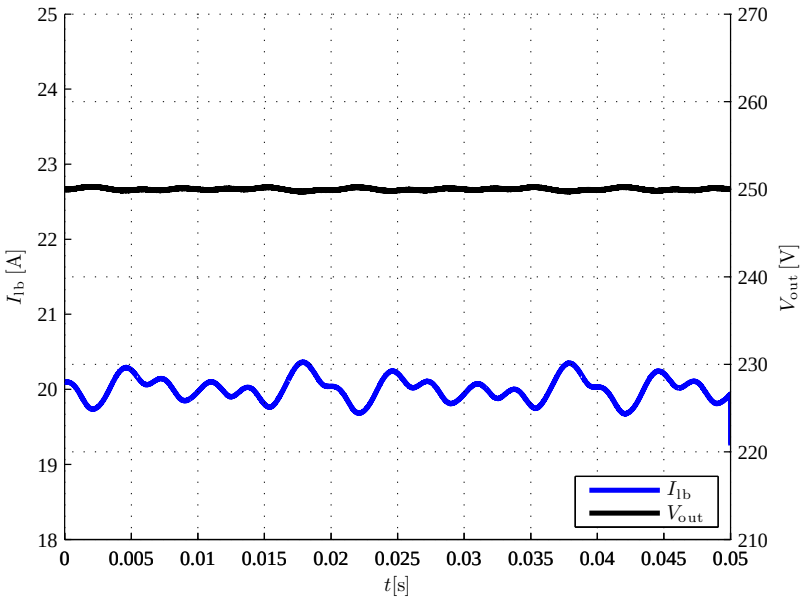

(a) Simulated

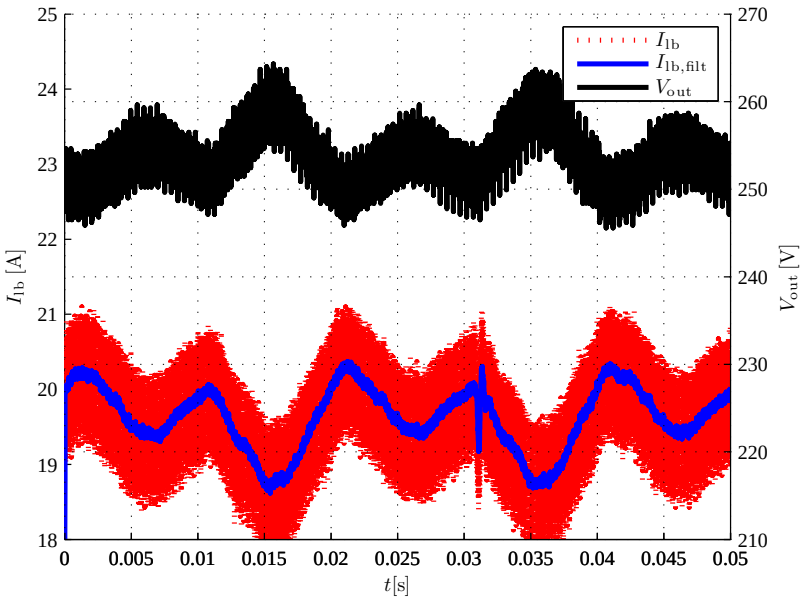

(b) Measured

Figure 4.7. LF input current ripple with the PID controller.

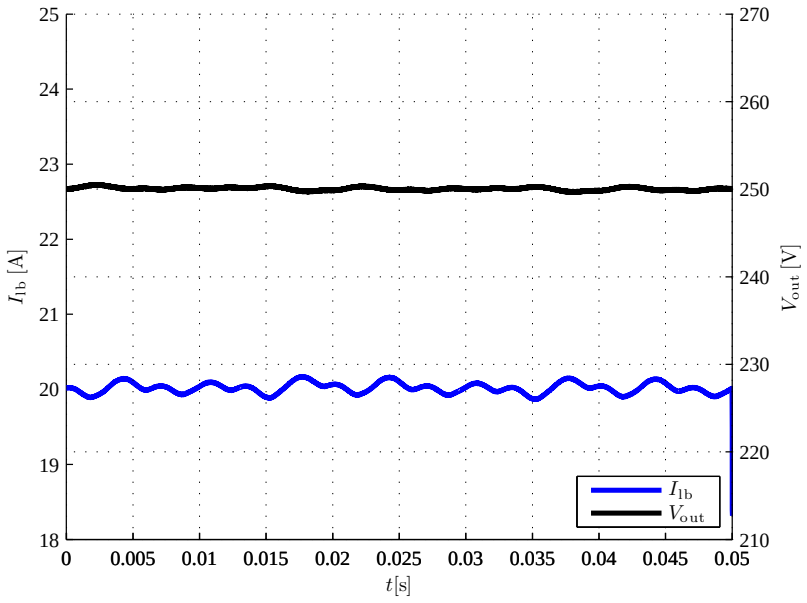

(a) Simulated

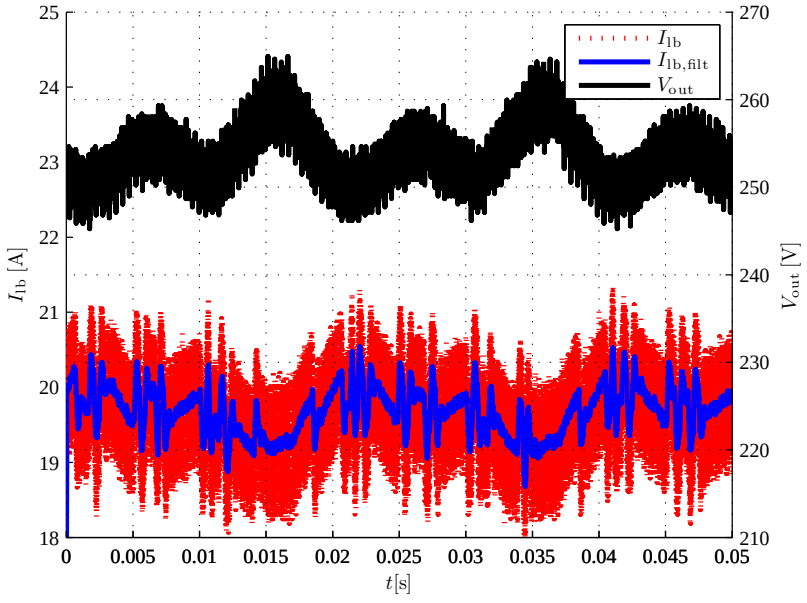

(b) Measured

Figure 4.8. LF input current ripple with a parallel connection of the PID and P+R controllers.

Figure 4.8 shows that the simulation and measurement results of the DC/DC converter input current ripple decrease as assumed. An unpredictable phenomenon is the increase in the high frequency ripple component. The origins of the HF component and methods to avoid it are suggested to be topics for further study.

4.4.3 Steady-state limit cycling

Limit cycling is an inherent property of the digital control systems, but it can be avoided as described in Section 1.7. From the viewpoint of the PCU, the LC raises some interesting questions. Does the LC of the DC/DC converter lead to an LC at the PCU level, or is it important at all? The case is divided into two subcases: a DC/DC converter with a resistive load and a PCU with a series connection of the DC/DC and grid converters. The target of the experiment is to verify the existence of LC and investigate its significance in the resistive load and the PCU.

The existence of limit cycling is verified by the measurements and the simulations with a resistive load $R_\mathrm{l} = 61.4\Omega$, V_g=50 V, and I_lb=100 A. The simulations and the corresponding measurements are presented in Fig. 4.9. The simulation results presented in Fig.4.9a suggest that limit cycling may occur, but because of the simulation accuracy, this cannot be confirmed with certainty. When observing the measurement results in Fig. 4.9b, it can be concluded that the phenomenon occurs. The measured amplitude of the limit cycling component is approximately 1–2 A. Equation (3.12) predicts the LC component to be approximately 1 A.

When observing the measurements of the LF ripple mitigation (Fig. 4.7 and Fig. 4.8), we can see that there is no clear indication of LC, or it is not significant. Therefore, it is suggested that LC is not significant when operating with a grid converter; however, further research is required on the topic.

As an answer to the research question whether LC occurs, we may conclude that the measurements support the theoretical results of LC with a resistive load. When operating with a PCU, the measurements are in good agreement with the hypothesis that LC is not significant when operating with a grid converter.

4.4.4 Disconnection from the grid

Disconnection from the grid is important because of the grid standards. From the perspective of the SOFC, the overcurrent situation may not occur, and therefore it is important to analyze the grid disconnection case. The research question in the grid disconnection case is 'does the PCU protect the fuel cell stack when the grid is disconnected unintendendly'.

The measurements were carried out by disconnecting the PCU from the grid through the main switch, while the simulation of the grid disconnection case was implemented as follows:

- Wait for the startup transients to mitigate,
- force the grid converter d-axis current reference to 0 A,
- wait for the protection scheme to trigger, and

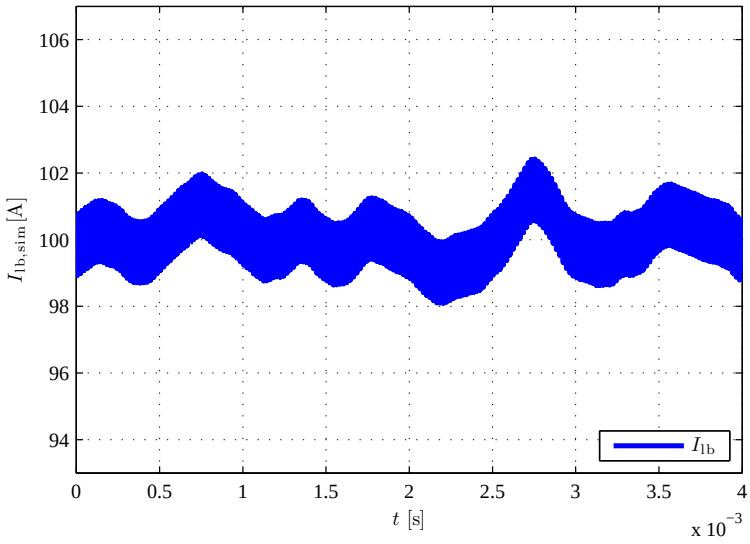

(a) Simulated

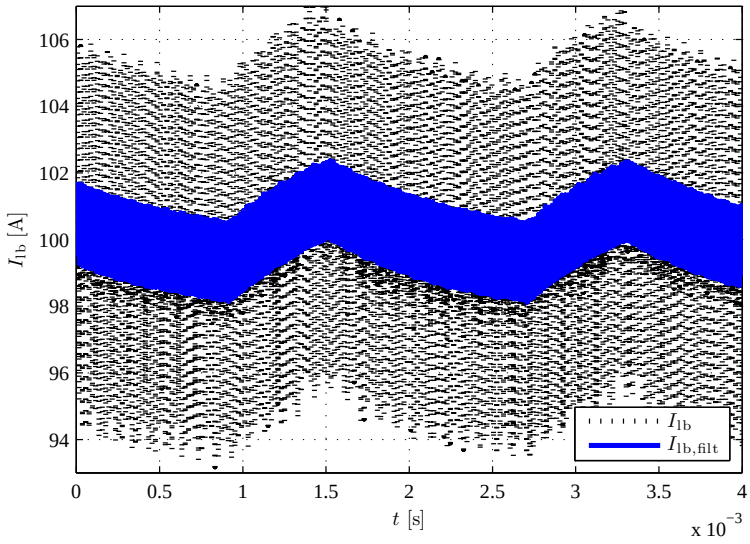

(b) Measured

Figure 4.9. LC effect in the input current of the DC/DC converter. The simulation results (a) suggest that LC may occur, but because of the simulation accuracy, it is not possible to draw this conclusion without doubt. On the other hand, the measurement (b) clearly indicates the occurrence of LC.

- observe the DC/DC input current.

The simulation results for the grid disconnection case are presented in Fig. 4.10a and for the corresponding measurements in Fig. 4.10b. In the measurements, the first safety function that was triggered was the 'grid frequency low' trigger, which leads to the shutdown process. Because the DC link breaker trigger level was set to 350 V, the DC link breaker was not triggered. The DC link voltage started to decrease immediately after the shutdown because of the discharge resistors.

The DC link voltage in the simulation was not as high as in the measurements. A possible reason for this difference is the implementation of the shutdown process. While in the simulation case the current controller of the DC/DC converter controlled the current $I_{\mathrm{lb}}$to zero, in the measurements the control system was bypassed, and the controller duty cycle was ramped to zero in the open loop. The simulation case was implemented in this way because the duty cycle of the linearized model does not follow the actual duty cycle values, and the moment before triggering of the shutdown process is the point of interest. With more complex simulation arrangements, the accuracy of the results would not be increased, and a possible occurrence of overcurrent can be observed with the proposed model.

Based on the simulation and measurement results, the system shutdown was safely executed, and the objective of the study was met. On the other hand, the overcurrent situation is not likely considering the DC link voltage rise after disconnection, which leads to a decrease in the input current.

4.4.5 Fuel cell emergency shutdown

A fuel cell emergency shutdown may occur for example when the BoP or the stack has a malfunction. In the FC emergency shutdown situation, the PCU should not be damaged. The measurements were implemented by shutting down the DC power supply while operating, and the simulation case was implemented as follows:

- Wait for the startup transients to mitigate,
- set the DC/DC converter current reference to 0 A,
- enable the protection scheme, and
- wait for the protection scheme to trigger and observe the DC link voltage.

The simulation measurements do not completely describe the actual situation, but in order to verify the control and protection of the PCU, it can be assumed that the accuracy is adequate. The simulation results for the fuel cell emergency shutdown are presented in Fig. 4.11a and the corresponding measurements in Fig. 4.11b.

Figure 4.11 shows that the simulation follows the measurement results with a sufficient accuracy. As the objective is to maintain the stability of the system and prevent the PCU breakdown in an emergency shutdown situation, we may conclude that the target was reached.

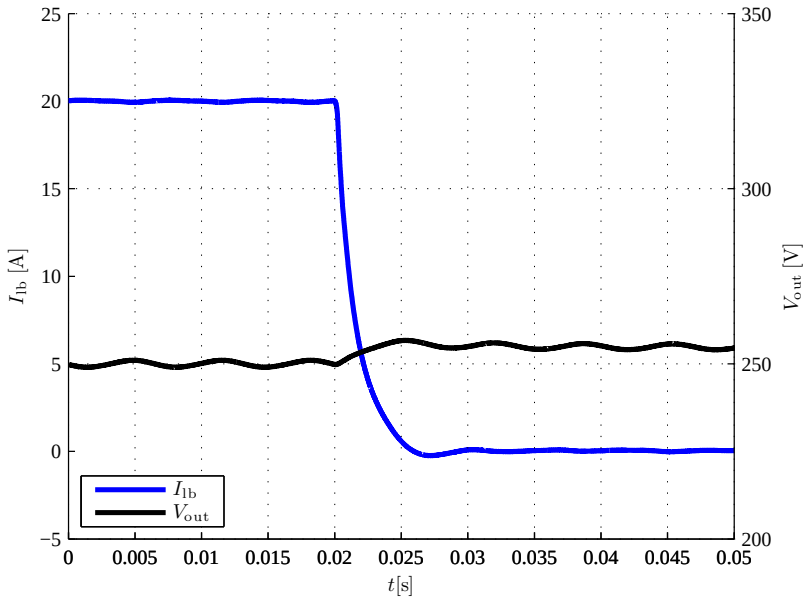

(a) Simulated

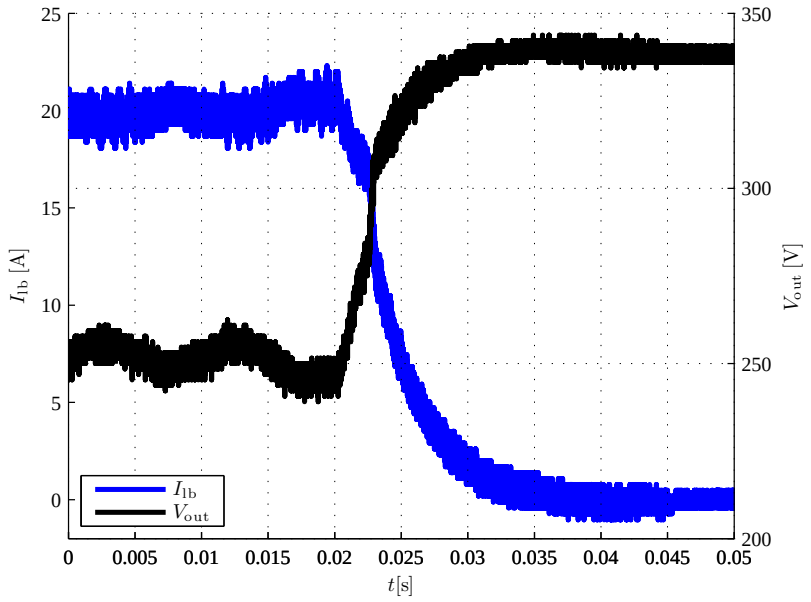

(b) Measured

Figure 4.10. Simulated (a) and measured (b) DC link voltages and input currents during the grid disconnection. The results indicate that a noticeable overcurrent does not occur at the moment of disconnection, and the shutdown process is controlled.

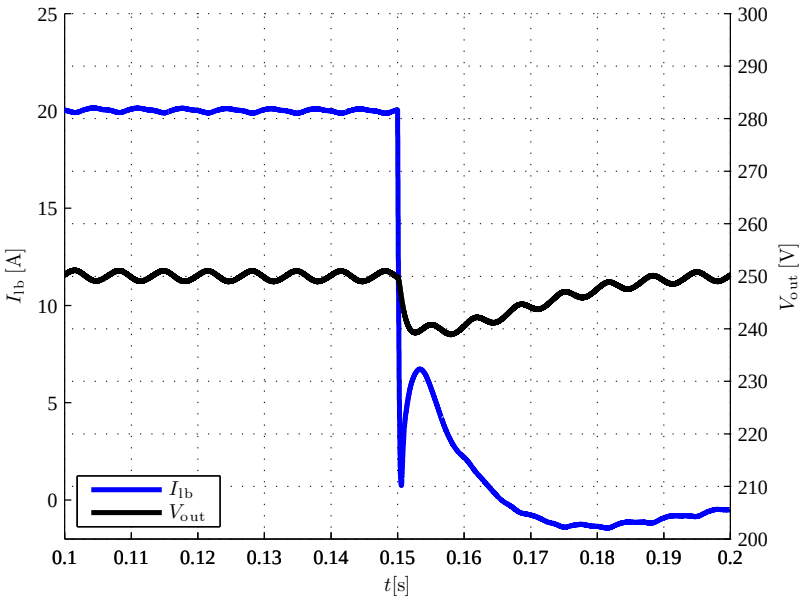

(a) Simulated

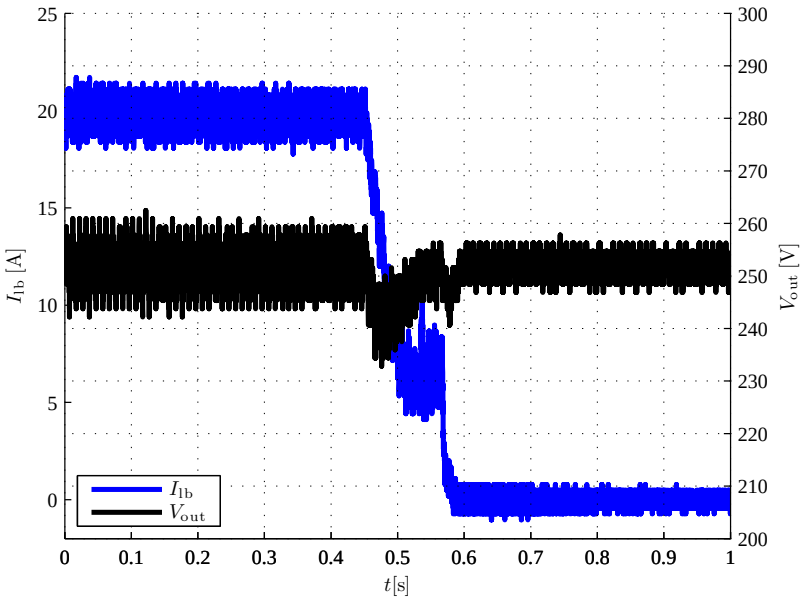

(b) Measured

Figure 4.11. Fuel cell emergency shutdown (simulation (a) and measurements (b)). In the fuel cell emergency shutdown, the PCU is disconnected from the stack with a contactor. Because of the disconnection, the DC link voltage is the point of interest in the experiment.

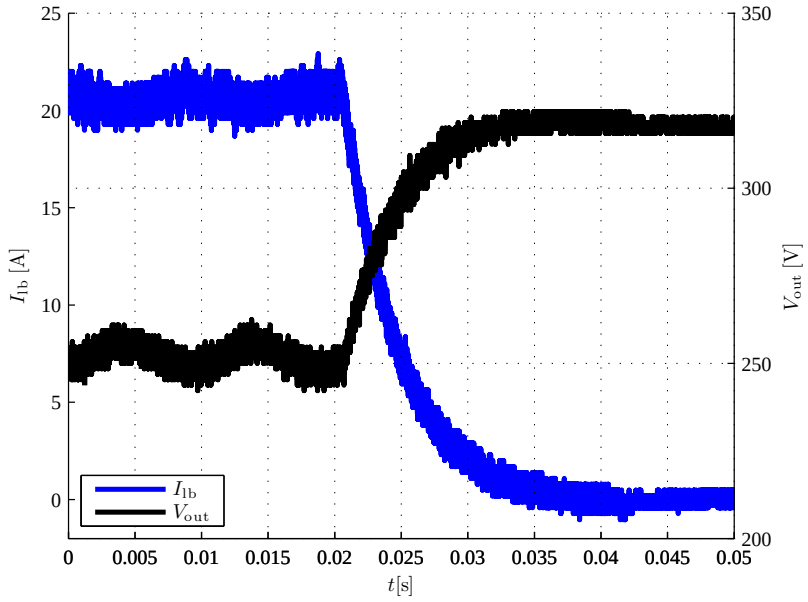

Figure 4.12. Experiment on the DC/DC overcurrent protection. The current is ramped up with a velocity of approx. one ampere/sec, while the overcurrent limit is set to 20 A. The measurements show that the system is able to shut down safely in the case of an overcurrent. The DC link voltage rises, but does not exceed the 350 V trigger voltage for breaking. The DC link voltage starts to decrease after the shutdown because of the discharge resistors.

4.4.6 DC/DC converter overcurrent protection

The DC/DC converter overcurrent may occur when the DC/DC converter is close to breakdown. In that case, the safety limits set on the input current can help in performing a controlled shutdown. Assuming that the simulation case is identical to the fuel cell emergency shutdown case (protection scheme sets the current reference to 0), only the measurement is presented here.

The overcurrent measurement was implemented by setting the overcurrent limit to 20 A and ramping the current up with a rate of approximately one ampere/sec. At 20 A, the protection scheme was triggered, and the PCU was driven down in a controlled manner. The overcurrent shutdown measurements are presented in Fig. 4.12.

4.5 Summary of the experimental results

The objectives set to the experimental results were to verify the developed models against the actual prototypes and to ensure that the fuel cell stack is interfaced safely in the steady state and in the most common abnormal situations. It was found that the developed model is suitable for the control system design, but in more complex simulation cases, a more sophisticated simulation software such as Spice

should be applied. The SSA model is not accurate enough for the simulation of abnormal operation, while the model can still provide guidelines for actual measurements.

It was also observed that the P+R controller met the expectations arising from simulations. The unexpected result was the high-frequency ripple that originated from the P+R controller. Hence, further research is recommended on the topic.

Based on the objectives set on the experimental research, we can draw a conclusion that the system is able to operate safely with a fuel cell stack, and the models are accurate enough to be used in the control design. In the further research, it is suggested to develop a method to measure the loop gains from a digitally controlled RPP converter.

Chapter 5

Conclusions and Discussion

The objective of this thesis was to model a PCU for the SOFC environment, and design and implement a control system for the PCU based on the requirements set by the SOFC. First, a literature survey was made of the fuel cells and fuel cell applications with the focus on the SOFC. By the literature survey, the characteristics and limitations set by the SOFC were identified. Based on the limitations, the literature study was extended to feasible control methods to meet the requirements.

After the literature survey, the suitable modeling methods for the DC/DC converter and the grid converter were introduced with the associated theories considering the modeling process. The digital control system characteristics were introduced, and the effects of the digitalization on the modeling procedure were identified.

Based on the literature survey and introduction, the DC/DC converter and the grid converter were modeled. By the model, an analysis in the frequency domain was made. Based on the derived models, a suitable control system was designed for the DC/DC converter and the grid converter. In the design, the interaction between the DC/DC converter and the grid converter was considered from the viewpoint of the SOFC. In addition, special emphasis was placed on the digital control system, and the effects of the digitalization were considered. From the perspective of the SOFC, the most interesting effects were identified. The proposed models were verified against the actual prototypes, and the control system design was tested and validated with the laboratory setup.

The major contributions of the study were:

- The characteristics of the SOFC as an electrical power source were identified.
- A solution to the interfacing of the SOFC in the distributed generation was proposed.
- A mathematical model of the PCU was provided.
- The control design for the DC/DC converter and the grid converter suitable for the SOFC was made.
- The limit-cycling phenomena of the digital control system as a source of low-frequency current ripple were identified.

- Because of the fluctuation of the DC link voltage, limit cycling was found to be insignificant when the DC/DC converter is tied to the grid converter.
- A method was proposed to reduce the second harmonic that arises from the grid unbalance in the output current of the stack.
- Practical considerations regarding the operating of the SOFC plant were presented.

The characteristics of the SOFC as an electrical power source were determined based on the literature survey. According to the results of the survey, the electrical equivalent circuit was developed. As it was not possible to measure the characteristics of the SOFC stack used, the model of the SOFC was addressed only at a theoretical level. It was found that a stability analysis can be made with the DC/DC converter and the stack by applying the well-known impedance theory, where the output impedance of the stack and the input impedance of the DC/DC converter are analyzed.

Based on the findings of the literature survey, also a steady-state equivalent model was presented for the stack. The proposed steady-state model was Thevenin's equivalent model with the measurement data fitted with the least-square method. Nevertheless, the applicability of the steady-state model to the dynamic modeling of the PCU is questionable. Even though the model is not relevant from the viewpoint of the control design, it can be useful when the electronics of the PCU is designed, because it is possible to approximate the operation point of the PCU and carry out the optimization of the topology based on this approximation.

A PCU that is able to connect the SOFC to the distribution grid was presented. At the start of the study, and at the moment of writing the conclusions, there was or is no commercial PCU available that would be able to connect the SOFC plant of the study to the grid. Even though a commercial device was chosen as the grid interface of the prototype plant based on reliability requirements, the suitability of the proposed PCU was verified. The DC/DC converter prototypes used with the actual stack and in this thesis corresponded with each other.

The mathematical model of the PCU was developed in the study. The DC/DC converter was modeled by the state-space averaging method, while the grid converter was modeled as a state-space model where the power stage was simplified to produce the required voltage vector to the input of the grid filter. The dynamical model of the resonant push pull converter has not been presented in the literature. The model was verified against the actual prototype; however, the frequency responses were not measured. At the moment of writing, a frequency analyzer was purchased as a consequence of the observations of the study, and measurements will be carried out in the future. The issue with the measurements of the prototype converter is the digital control system, where the suitable current injection path to the feedback loop is not unambiguous. Based on the model, it was also noticed that when operating with small duty cycles (approx. D<0.2), there was a resonance peak of the snubber capacitors, which can produce problems with the control design if not taken into account during the design process.

A similar effect was detected with the model of the grid converter, where the grid inductance was varied. The grid inductance has an impact on the frequency response and the resonance peak of the LC(L) filter, and therefore, changes in the grid-side inductance should be observed during the design of the control system.

The control design of the system was carried out by converting the demands arising from the SOFC into the requirements for the control system. Based on the requirements set by the SOFC, a suitable control

system was designed for the DC/DC converter and the grid converter. The focus of the control system was on the DC/DC converter because there was no commercial DC/DC converter available that would be suitable to interface the SOFC of the research, whereas grid converters of the corresponding power levels are widely available. The control design of the grid converter was completed because the dynamics of the PCU arise from the series connection of the DC/DC converter and the grid converter, and the in-depth understanding of the PCU behavior requires detailed knowledge of both converters.

The limit cycling phenomenon, which results from the finite precision of the digital arithmetics, was observed. The significance of the phenomenon when operating with the SOFC is related to the lacking tolerance of the stack to the low-frequency current ripple, which may be produced by the digital controller. The limit cycling phenomenon can be avoided by the conditions presented in the literature, but the implementation can be problematic because the operating frequencies of the FPGAs and the accuracy of the digital modulator are interlinked. Even though the limit cycling can be avoided, the price of the required integrated circuits (ICs) may be an obstacle in a commercial application.

Because of the fluctuation of the DC link voltage, limit cycling was observed to be insignificant when the DC/DC converter was connected with the grid converter. It was observed that the second harmonic of the grid is a more significant source of the low-frequency ripple component than the limit cycling. Therefore, if the DC/DC converter operates without a grid converter, the LC must be observed to ensure that the low-frequency ripple component is kept within the allowed limits.

As it was found significant to mitigate the second harmonic of the grid, a method was proposed to reduce the second harmonic in the input current of the DC/DC converter. The method uses a simple proportional+resonant controller, which is tuned to reduce the harmful low-frequency component. The method was observed to effectively mitigate the second harmonic in the simulation, and the measurement results confirmed the simulation results when an HF frequency component was induced to the current. The reason for this high-frequency component could be a topic of further research, although we may ask how well the mitigation could be achieved by increasing the gain and decreasing the phase margin of the average current controller, which occurs when the P+R controller is added.

When operating with an actual SOFC stack, the protection principles and filtering of the input current reference are presented. Based on the practical issues related to the integration of the PCU to the stack, guidelines for the successful control system design, both theoretical and practical, are presented.

Based on the observations of this study, many interesting research topics arise:

- Placement of the grid harmonic compensation,
- determination of the grid-side inductance,
- usage of the parallel DC/DC converters,
- detailed analysis of the discrete implementation of P+R controller,
- control of the additional power storage in the islanding mode, and
- stability of the series-connected converters.

The second harmonic compensation can be carried out in the grid converter stage or in the DC/DC converter stage. A question where this should be done remains to be answered. Further: What are

the benefits of compensating the harmonics in the grid converter, and what are the limitations set by the standards? An interesting approach would be to use a repetitive resonant controller to mitigate all significant grid harmonics seen by the fuel cell stack. Does the solution introduce stability issues, or are there some drawbacks with the proposed controller? From the viewpoint of a commercial device, a further question is whether these phenomena are significant at all. The limits of the low-frequency current ripple that the stack can tolerate should be defined more accurately. The effects of the high-frequency current ripple in the long term should also be studied.

In the grid converter, it was noticed that the grid-side inductance can add instability to the system, and in the worst case, the resonance frequency of the filter and the grid can be close to the switching frequency. Based on this observation, it is suggested to study the grid-side inductance detection. The IMC controller stability in the discrete systems should also be studied, for example, by Youla parametrization.

The issue of the optimal unit size of the DC/DC converter raises a question of how to use the parallel DC/DC converters. The benefit of using parallel converters is the opportunity to optimize the usage of the parallel converters in such a way that the optimum efficiency is achieved by load sharing. Furthermore, with adequate synchronization, the effective current ripple seen by the fuel cell stack can be reduced.

A further interesting research question is how the system could be made to operate in the islanding mode. Because of the slow response times of the SOFC, an additional power storage should be included in the system to compensate the load peaks. Moreover, the optimization of the power storage, the grid converter, and the DC/DC converter from the perspective of efficiency and total costs of ownership (TCO) is an important research topic. In addition, the stability issues that arise from the complex composition of separate converters with varying load conditions have to be studied.

From the theoretical perspective, the mathematical form of the stability criteria of a series-connected DC/DC converter and a grid converter is of interest. A possible method to describe and analyze the stability of a series-connected system could be the impedance matching of the output impedance of the DC/DC converter and the input impedance of the grid converter. The grid converter can be presented in DC quantities in the dq coordinates, which makes it possible to apply the known impedance matching theorems (Erickson and Maksimovic, 2001).

At a theoretical level, the study has gathered the methods to successfully derive a model for a DC/DC converter, a grid converter, and the whole PCU. The results of the study can also be used in other applications. The series connection of the DC/DC converter and the voltage source inverter is widely used in distributed generation, such as photovoltaic systems. Based on the results of the study, the models and methods can be adopted to further use. The theoretical model of the RPP converter can be used as such, while the model of the PCU can be applied to the modeling process of the fuel cell plant, with an in-depth knowledge of the inner dynamics of the PCU.

When comparing the results with the initial objectives of the doctoral study, we may conclude that the study has met the set objectives. Numerous interesting research topics have arisen during the study, while the focus has been kept on the fuel cell environment. In this doctoral thesis, theoretical and practical guidelines have been presented for the successful control design to connect a SOFC to the utility grid in a distributed generation application.

References

Acharya, K., Mazumder, S., Burra, R., Williams, R., and Haynes, C. (2003), "System-interaction analyses of solid-oxide fuel cell (sofc) power-conditioning system," in *Conference Record of the 38th IAS Annual Meeting, Industry Applications Conference*, vol. 3, pp. 2026–2032.

Akkinapragada, N. and Chowdhury, B. (2006), "Sofc-based fuel cells for load following stationary applications," in *the 38th North American Power Symposium, NAPS, 2006*, pp. 553–560.

Al-Atrash, H. and Batarseh, I. (2007), "Digital controller design for a practicing power electronics engineer," in *Twenty Second Annual IEEE Applied Power Electronics Conference, APEC 2007*, pp. 34–41.

Buso, S. and Mattavelli, P. (2006), *Digital control in power electronics*, Synthesis lectures on power electronics, Morgan & Claypool Publishers.

Candusso, D., Valero, L., and Walter, A. (2002), "Modelling, control and simulation of a fuel cell based power supply system with energy management," in *the 28th Annual Conference of the IEEE Industrial Electronics Society, 2002, IECON 02*, vol. 2, pp. 1294–1299.

Chiu, L.Y. and Diong, B. (2003), "An improved small-signal model of the dynamic behavior of pem fuel cells," in *Conference Record of the 38th Industry Applications Conference, IAS Annual Meeting, 2003*, vol. 2, pp. 709–715.

Choi, B., Lim, W., Choi, S., and Sun, J. (2008), "Comparative performance evaluation of current-mode control schemes adapted to asymmetrically driven bridge-type pulsewidth modulated dc-to-dc converters," *IEEE Transactions on Industrial Electronics*, vol. 55, no. 5, pp. 2033–2042.

EN6100 (2005), *EN 61000-3-3, Ed. 1.2 Electromagnetic Compability (EMC) - Part 3-3: Limits - Limitation of Voltage Changes, Voltage Fluctuations and Flicker in Public Low-Voltage Supply Systems, for Equipment with Rated Current $\leq$ 16 A per Phase and Not Subject to Conditional Connection*, European Committee For Electrotechnical Standardization (CENELEC), Brussels, Belgium.

Engler, A. and Soultanis, N. (2005), "Droop control in lv-grids," in *International Conference on Future Power Systems, 2005*.

Erickson, R.W. and Maksimovic, D. (2001), *Fundamentals of Power Electronics*, Springer Science+Business Media, Inc, 233 Spring Street, New York, NY 10013, USA.

Farooque, M. and Maru, H. (2001), "Fuel cells-the clean and efficient power generators," *in Proceedings of the IEEE*, vol. 89, no. 12, pp. 1819–1829.

Fontes, G., Turpin, C., Astier, S., and Meynard, T. (2007), "Interactions between fuel cells and power converters: Influence of current harmonics on a fuel cell stack," *IEEE Transactions on Power Electronics*, vol. 22, no. 2k, pp. 670–678.

Guerrero, J., Blaabjerg, F., Zhelev, T., Hemmes, K., Monmasson, E., Jemei, S., Comech, M., Granadino, R., and Frau, J. (2010), "Distributed generation: Toward a new energy paradigm," *IEEE Industrial Electronics Magazine*, vol. 4, no. 1, pp. 52–64.

Halinen, M., Rautanen, M., Saarinen, J., Pennanen, J., Pohjoranta, A., Kiviaho, J., Pastula, M., Nuttall, B., Rankin, C., and Borglum, B. (2011), "Performance of a 10 kw sofc demonstration unit," *ECS Transactions*, vol. 35, no. 1, pp. 113–120, URL `http://link.aip.org/link/abstract/ECSTF8/v35/i1/p113/s1`.

Harnefors, L. and Nee, H.P. (1998), "Model-based current control of ac machines using the internal model control method," *IEEE Transactions on Industry Applications*, vol. 34, no. 1, pp. 133–141.

Hatziadoniu, C., Lobo, A., Pourboghrat, F., and Daneshdoost, M. (2002), "A simplified dynamic model of grid-connected fuel-cell generators," *IEEE Transactions on Power Delivery*, vol. 17, no. 2, pp. 467 –473.

Hoogers, G. (2003), *Fuel cell technology handbook*, Mechanical Engineering Series, CRC Press LLC, Florida, USA.

Huang, X., Zhang, Z., and Jiang, J. (2006), "Fuel cell technology for distributed generation: An overview," in *IEEE International Symposium on Industrial Electronics*, vol. 2, pp. 1613 –1618.

Hwang, J., Lehn, P., and Winkelnkemper, M. (2007), "Control of grid connected ac-dc converters with minimized dc link capacitance under unbalanced grid voltage condition," in *European Conference on Power Electronics and Applications*, pp. 1 –10.

IEC (2000), *IEC 61000-3-11. Ed. 1, Electromagnetic Compability (EMC) - Part 3-11: Limits - Limitation of Voltage Changes, Voltage Fluctiations and Flicker in Public Low-Voltage Supply Systems - Equipment with Rated Current $\leq$ 75 A and Subject to Conditional Connection*, 61000-3-11, International Electrotechnical Commission (IEC), Geneva, Switzerland.

IEC (2003), *IEC 61000-3-12 Ed. 1, Electromagnetic Compability (EMC) - Part 3-12: Limits - Limits for Harmonic Currents Produced by Equipment Connected to Public Low-Voltage Systems with Input Current > 16 A and $\leq$ 75 A per Phase*, 61000-3-12, International Electrotechnical Commission (IEC), Geneva, Switzerland.

IEC (2004), *IEC 61727 Ed. 2, Photovoltaic (PV) Systems - Characteristics of the Utility Interface*, 61727, International Electrotechnical Commission (IEC), Geneva, Switzerland.

IEC (2005), *IEC 61000-3-2 Ed. 3.0, Electromagnetic Compatibility (EMC) - Part 3-2: Limits - Limits for Harmonic Current Emissions (Equipment Input Current $\leq$ 16 A per Phase)*, 61000-3-2 Ed. 3.0, International Electrotechnical Commission (IEC), Geneva, Switzerland.

IEEE (2000), *IEEE Std 929-2000, IEEE Recommended Practice for Utility Interface of Photovoltaic (PV) Systems*, 929, The Institute of Electrical and Electronics Engineers, Inc. New York, USA.

IEEE (2003), *IEEE Std 1541-2003, IEEE Standard for Interconnecting Distributed Resources With Electric Power Systems*, 1547, The Institute of Electrical and Electronics Engineers, Inc. New York, USA.

Kaura, V. and Blasko, V. (1997), "Operation of a phase locked loop system under distorted utility conditions," *IEEE Transactions On Industry Applications*, vol. 33, pp. 58–63.

Kazmierkowski, M. and Malesani, L. (1998), "Current control techniques for three-phase voltage-source pwm converters: a survey," *IEEE Transactions on Industrial Electronics*, vol. 45, no. 5, pp. 691–703.

Kovács, K. and Rácz, I. (1959), *Transiente Vorgänge in Wechselstrommaschinen [Transient phenomena in AC machines]*, no. nid. 1 in Transiente Vorgänge in Wechselstrommaschinen, Verlag der Ungarischen Akademie der Wissenschaften.

Kron, G. (1938), *The Application of Tensors to the Analysis of Rotating Electrical Machinery*, General Electric Review.

Kwon, J.M., Kim, E.H., Kwon, B.H., and Nam, K.H. (2009), "High-efficiency fuel cell power conditioning system with input current ripple reduction," *IEEE Transactions on Industrial Electronics*, vol. 56, pp. 826–834.

Kwon, J.M. and Kwon, B.H. (2009), "High step-up active-clamp converter with input-current doubler and output-voltage doubler for fuel cell power systems," *IEEE Transactions on Power Electronics*, vol. 24, no. 1, pp. 108–115.

Laffly, E., Pera, M.C., and Hissel, D. (2006), "Dynamic model of a polymer electrolyte fuel cell power device," in *the 32nd Annual Conference on IEEE Industrial Electronics, IECON 2006*, pp. 466–471.

Larminie, J. and Dicks, A. (2003), *Fuel Cell Systems Explained*, John Wiley & Sons Ltd, West Sussex, England, 2 edn.

Lee, J., Jo, J., Choi, S., and Han, S.B. (2006), "A 10-kw sofc low-voltage battery hybrid power conditioning system for residential use," *IEEE Transactions on Energy Conversion*, vol. 21, no. 2, pp. 575–585.

Leonhard, W. (2001), *Control of Electrical Drives, 3rd edition*, Electric energy systems and engineering series, Springer-Verlag Berlin.

Li, Y., Choi, S., and Rajakaruna, S. (2005), "An analysis of the control and operation of a solid oxide fuel-cell power plant in an isolated system," *IEEE Transactions on Energy Conversion*, vol. 20, no. 2, pp. 381–387.

Li, Y., Rajakaruna, S., and Choi, S. (2007), "Control of a solid oxide fuel cell power plant in a grid-connected system," *IEEE Transactions on Energy Conversion*, vol. 22, no. 2, pp. 405–413.

Lim, W., Choi, B., and Sun, J. (2005), "Comparative performance evaluation of current-mode controls adapted to asymmetrically-driven bridge-type pulse-width modulated dc-to-dc converters," in *the 20th Annual IEEE Applied Power Electronics Conference and Exposition, APEC 2005*, vol. 2, pp. 1179–1185.

Liserre, M., Blaabjerg, F., and Teodorescu, R. (2007), "Grid impedance estimation via excitation of lcl -filter resonance," *IEEE Transactions on Industry Applications*, vol. 43, no. 5, pp. 1401–1407.

Liu, C. and Lai, J.S. (2007), "Low frequency current ripple reduction technique with active control in a fuel cell power system with inverter load," *IEEE Transactions on Power Electronics*, vol. 22, no. 4, pp. 1429–1436.

Maksimovic, D. and Zane, R. (2007), "Small-signal discrete-time modeling of digitally controlled pwm converters," *IEEE Transactions on Power Electronics*, vol. 22, no. 6, pp. 2552–2556.

Mazumder, S., Acharya, K., Haynes, C., Williams, R., J., von Spakovsky, M., Nelson, D., Rancruel, D., Hartvigsen, J., and Gemmen, R. (2004), "Solid-oxide-fuel-cell performance and durability: resolution of the effects of power-conditioning systems and application loads," *IEEE Transactions on Power Electronics*, vol. 19, no. 5, pp. 1263–1278.

Middlebrook, R.D. and Cuk, S. (1977), "A general unified approach to modelling switching-converter power stages," *International Journal of Electronics*, vol. 42, pp. 521–550.

Mohan, N., Undeland, T.M., and Robbins, W.P. (2002), *Power Electronics: Converters, Applications, and Design, 3rd. Edition*, John Wiley & Sons, Inc., 111 River Street, Hoboken, NJ 07030.

National Energy Technology Laboratory (2004), *Fuel Cell Handbook, seventh edition*, U.S. Department of Energy, Office of Fossil Energy, National Energy Technology Laboratory, P.O. Box 880 Morgantown, West Virginia 26507-0880.

Neacsu, D.O. (2006), *Power Switching Converters. Medium and High Power*, CRC Press Taylor & Francis Group, FL, USA.

Nymand, M. and Andersen, M. (2008), "A new approach to high efficiency in isolated boost converters for high-power low-voltage fuel cell applications," in *The 13th Power Electronics and Motion Control Conference, EPE-PEMC 2008*, pp. 127–131.

Oates, C., Crookes, R., Pyke, S., and Leah, R. (2002), "Power conditioning for solid oxide fuel cells," in *International Conference on (Conf. Publ. No. 487) Power Electronics, Machines and Drives, 2002*, pp. 12 – 17.

Ogata, K. (1995), *Discrete-Time Control Systems, 2nd. edition*, Pearson Education Inc., Upper Saddle River, New Jersey, U.S.A.

Ottersten, R. and Svensson, J. (2002), "Vector current controlled voltage source converter-deadbeat control and saturation strategies," *IEEE Transactions on Power Electronics*, vol. 17, no. 2, pp. 279–285.

Ozpineci, B., Tolbert, L.M., and Adams, D.J. (2004), "Trade study on aggregation of multiple 10-kw solid oxide fuel cell power modules," Tech. rep., Oak Ridge National Laboratory, Oak Ridge, Tennessee, USA.

Padullés, J., Ault, G.W., and McDonald, J.R. (2000), "An integrated sofc plant dynamic model for power systems simulation," *Journal of Power Sources*, vol. 86, no. 1–2, pp. 495–500.

Park, R. (1929), "Two-reaction theory of synchronous machines," *AIEE Transactions*, vol. 48, pp. 716–730.

Park, S.Y., Chen, C.L., and Lai, J.S. (2008), "A wide-range active and reactive power flow controller for a solid oxide fuel cell power conditioning system," *IEEE Transactions on Power Electronics*, vol. 23, no. 6, pp. 2703–2709.

Pasricha, S., Keppler, M., Shaw, S., and Nehrir, M. (2007), "Comparison and identification of static electrical terminal fuel cell models," *IEEE Transactions on Energy Conversion*, vol. 22, no. 3, pp. 746–754.

Peterchev, A. and Sanders, S. (2003), "Quantization resolution and limit cycling in digitally controlled pwm converters," *IEEE Transactions on Power Electronics*, vol. 18, no. 1, pp. 301–308.

Proakis, J.G. and Manolakis, D.G. (1996), *Digital Signal Processing - Principles, Algorithms, and Applications*, Prentice-Hall Inc. Simon & Schuster, New Jersey, USA.

Rajashekara, K. (2003), "Power conversion and control strategies for fuel cell vehicles," *the 29th Annual Conference of the IEEE Industrial Electronics Society, IECON 2003*, vol. 3, pp. 2865–2870.

Riipinen, T., Laakkonen, O., Lehonkoski, L., Vaisanen, V., Silventoinen, P., and Pyrhonen, O. (2009), "Design and analysis of fpga-based control of a fuel cell line converter," in *the 35th Annual Conference of IEEE Industrial Electronics, 2009, IECON '09*, pp. 363–366.

Riipinen, T., Vaisanen, V., Kuisma, M., Seppa, L., Mustonen, P., and Silventoinen, P. (2008), "Requirements for power electronics in solid oxide fuel cell system," in *the 13th Power Electronics and Motion Control Conference, EPE-PEMC 2008*, pp. 1233–1238.

Riipinen, T., Vaisanen, V., and Silventoinen, P. (2011), "Requirements for the control system of an sofc power conversion unit in stationary power generation," in *the 26th Annual IEEE Applied Power Electronics Conference and Exposition (APEC) 2011*, pp. 133–141.

Salli, J. (2009), *RTOS Framework for Real-Time Control System*, Master's thesis, Lappeenranta University of Technology, Finland.

Santi, E., Franzoni, D., Monti, A., Patterson, D., Ponci, F., and Barry, N. (2002), "A fuel cell based domestic uninterruptible power supply," in *the 17th Annual IEEE Applied Power Electronics Conference and Exposition, APEC 2002*, vol. 1, pp. 605–613.

Smith, J., Nehrir, M., Gerez, V., and Shaw, S. (2002), "A broad look at the workings, types, and applications of fuel cells," in *IEEE Power Engineering Society Summer Meeting, 2002*, vol. 1, pp. 70–75.

Stanley, H. (1938), "An analysis of the induction motor," *AIEE*, vol. 57, pp. 751–755.

Åström, K.J. and Wittenmark, B. (1997), *Computer-controlled systems, third edition*, Prentice Hall, Inc., NJ, USA.

Sun, J. and Bass, R. (1999), "Modeling and practical design issues for average current control," in *the 14th Annual Applied Power Electronics Conference and Exposition, 1999, APEC '99*, vol. 2, pp. 980–986.

Teodorescu, R., Liserre, M., and Rodríguez, P. (2011), *Grid Converters for Photovoltaic and Wind Power Systems*, John Wiley and Sons, Ltd, West Sussex, United Kingdom.

Timbus, A., Liserre, M., Teodorescu, R., Rodriguez, P., and Blaabjerg, F. (2009), "Evaluation of current controllers for distributed power generation systems," *IEEE Transactions on Power Electronics*, vol. 24, no. 3, pp. 654–664.

Timbus, A., Teodorescu, R., Blaabjerg, F., and Liserre, M. (2005), "Synchronization methods for three phase distributed power generation systems. an overview and evaluation," in *the 36th IEEE Power Electronics Specialists Conference, 2005, PESC '05*, pp. 2474–2481.

Underwriters Laboratories Inc (2001), *UL741 Inverters, Converters, and Controllers for Use in Independent Power Systems*, 741, Underwriters Laboratories Inc. (UL), IL, USA.

Vaisanen, V., Riipinen, T., Hiltunen, J., and Silventoinen, P. (2011), "Design of 10 kw resonant push-pull dc-dc converter for solid oxide fuel cell applications," in *Proceedings of the 14th European Conference on Power Electronics and Applications, EPE 2011*, pp. 1–10.

Vaisanen, V., Riipinen, T., and Silventoinen, P. (2010), "Effects of switching asymmetry on an isolated full-bridge boost converter," *IEEE Transactions on Power Electronics*, vol. 25, no. 8, pp. 2033–2044.

VDE Verlag (2006), *Automatic Disconnection Device between a Generator and the Public Low-Voltage Grid*, 0126-1-1, VDE VERLAG GMBH, Berlin-Offenbach.

Wang, C. and Nehrir, M. (2007a), "A physically based dynamic model for solid oxide fuel cells," *IEEE Transactions on Energy Conversion*, vol. 22, no. 4, pp. 887–897.

Wang, C. and Nehrir, M. (2007b), "Short-time overloading capability and distributed generation applications of solid oxide fuel cells," *IEEE Transactions on Energy Conversion*, vol. 22, no. 4, pp. 898–906.

Wang, J., Peng, F., Anderson, J., Joseph, A., and Buffenbarger, R. (2004), "Low cost fuel cell converter system for residential power generation," *IEEE Transactions on Power Electronics*, vol. 19, no. 5, pp. 1315–1322.

Xu, H., Kong, L., and Wen, X. (2004), "Fuel cell power system and high power dc-dc converter," *IEEE Transactions on Power Electronics*, vol. 19, pp. 1250–1255.

Xue, X., Tang, J., Sammes, N., and Du, Y. (2005), "Dynamic modeling of single tubular sofc combining heat/mass transfer and electrochemical reaction effects," *Journal of Power Sources*, vol. 142, no. 1–2, pp. 211–222.

Yakushev, V., Meleshin, V., and Fraidlin, S. (1999), "Full-bridge isolated current fed converter with active clamp," in *the 14th Annual Applied Power Electronics Conference and Exposition, APEC '99*, vol. 1, pp. 560–566.

Appendices

Appendix A

DC/DC converter steady-state model

A steady-state model is used to verify the steady-state operation of the system. Small-ripple approximation and a DC transformer model are used in the process. In the steady-state analysis, the snubber capacitor C_{c1} and C_{c2} voltages are assumed constant, a symmetrical operation is assumed, the duty cycle is over 0.5, and the switching losses and the transformer leakage inductance are neglected.

The steady-state equivalent circuit can be composed of the inductor voltage equations and the capacitor current equations. When operating in the steady state, Kirchhoff's Voltage Law (KVL) (A.1) and Kirchhoff's Current Law (KCL) (A.2) must be satisfied:

$$\sum_{i=1}^{n} V_i = 0, \tag{A.1}$$

$$\sum_{i=1}^{n} I_i = 0. \tag{A.2}$$

The inductor L_{lb} voltage can be defined during the switching state t_1 by

$$\langle V_{lb} \rangle = V_g. \tag{A.3}$$

During the switching state t_2 , the inductor L_{lb} voltage can be defined by

$$\langle V_{lb} \rangle = V_g - \frac{1}{2} V_{cc1}. \tag{A.4}$$

By observing that during the switching period the average value of V_{cr1} and V_{cr2} is nV_{cc}, we may write Equation (A.4) as follows

$$\langle V_{lb} \rangle = V_g - \frac{1}{2n} V_{cr1}. \tag{A.5}$$

By applying Kirchoff's Voltage Law during each interval and setting the average to zero, we obtain a voltage equation for L_{lb}

$$\langle V_{lb} \rangle = (D - \frac{1}{2}) V_g + (1 - D)(V_g - \frac{1}{2n} V_{cr1}) \tag{A.6}$$

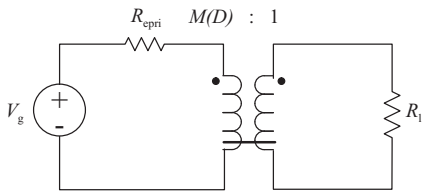

Figure A.1. Equivalent steady-state model for the RPP converter.

By observing that during the switching period $V_{cr1} = \frac{1}{2}V_{dc}$, we can write Equation (A.6) to the form

$$\langle V_{lb} \rangle = (D - \frac{1}{2})V_g + (1-D)(V_g - \frac{1}{4n}V_{dc}) \tag{A.7}$$

Based on (A.7), the relation between V_g and V_{dc} can derived as

$$(D - \frac{1}{2})V_g = -(1-D)(V_g - \frac{1}{4n}V_{dc}) \tag{A.8a}$$

$$DV_g - \frac{V_g}{2} = -(V_g - \frac{1}{4n}V_{dc} - DV_g + D\frac{1}{4n}V_{dc}) \tag{A.8b}$$

$$V_g - \frac{V_g}{2} = (1-D)\frac{1}{4n}V_{dc} \tag{A.8c}$$

$$V_g = \frac{1-D}{2n}V_{dc} \tag{A.8d}$$

$$\frac{V_g}{V_{dc}} = \frac{1-D}{2n} \tag{A.8e}$$

$$\frac{V_{dc}}{V_g} = n\frac{2}{(1-D)} \tag{A.8f}$$

The output voltage and the equilibrium conversion ratio is defined from Equation (A.8d). The equilibrium conversion ratio is

$$M(D) = \frac{1-D}{2n}. \tag{A.9}$$

Based on the equilibrium conversion ratio, the DC transformer model can be defined. The DC-derived transformer model is presented in Fig. A.1.

The input current can be calculated by referring all components to the primary and solving the input current by basic circuit algebra. The input current of the converter can be predicted by

$$I_{lb} = \frac{V_g}{\frac{R_l}{M(D)^2}}, \tag{A.10}$$

where

$$R_l = \frac{V_{dc}}{I_{ac}} \tag{A.11}$$

Appendix B

Simulation models

The presented simulation models are based on the modeling procedure introduced in Chapter 2. The switching model of the RPP converter illustrated in Fig. B.7 is based on Equations (2.38)–(2.65), while the linear model of the RPP converter depicted in Fig. B.8 is based on the state-space equations (2.66)–(2.76). The VSI model shown in Fig. B.3 is based on Equation (2.84). Other modeling blocks are based on the corresponding equations given in Chapters 2 and 3.

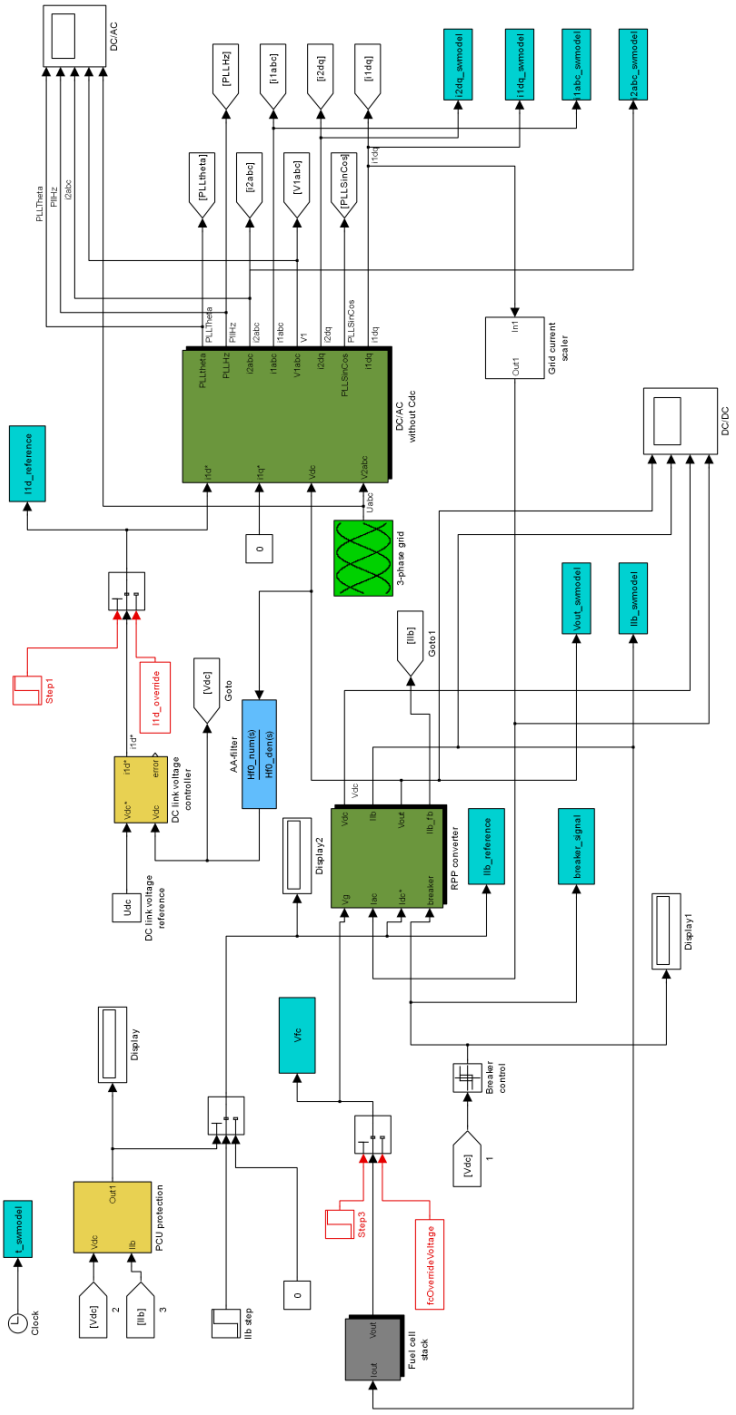

Figure B.1. Top-level diagram of the PCU model.

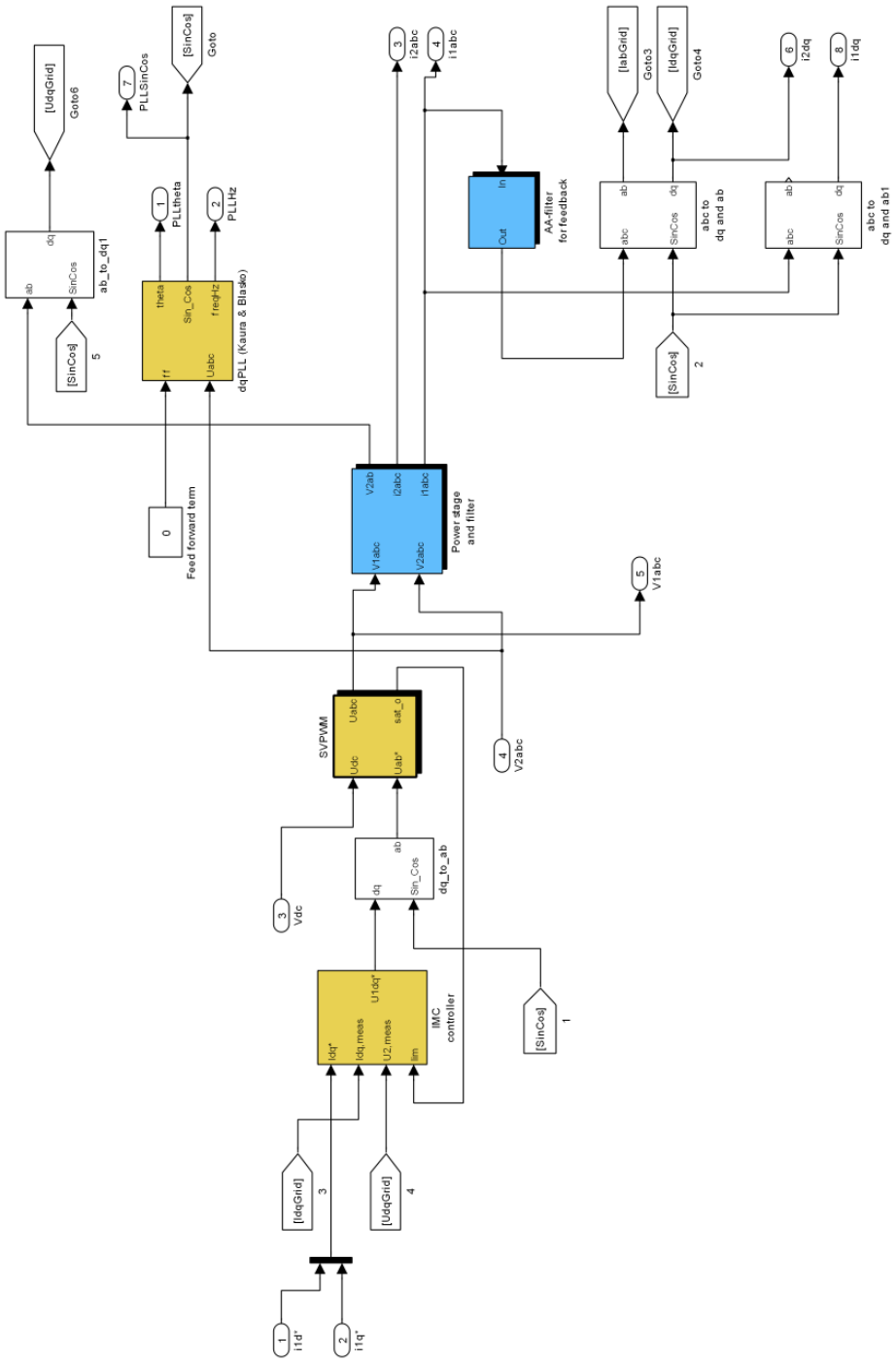

Figure B.2. Top-level diagram of the VSI model.

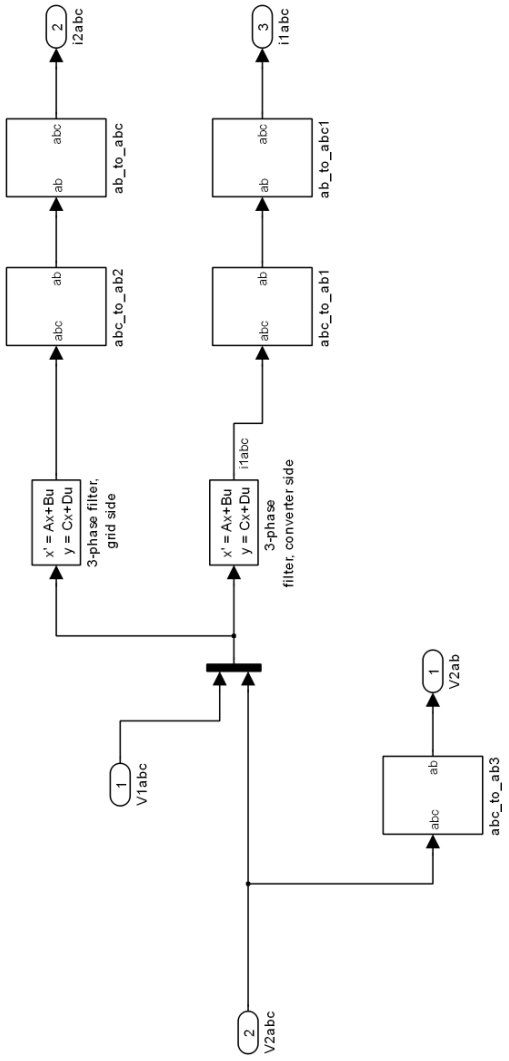

Figure B.3. State-space model of the VSI power stage.

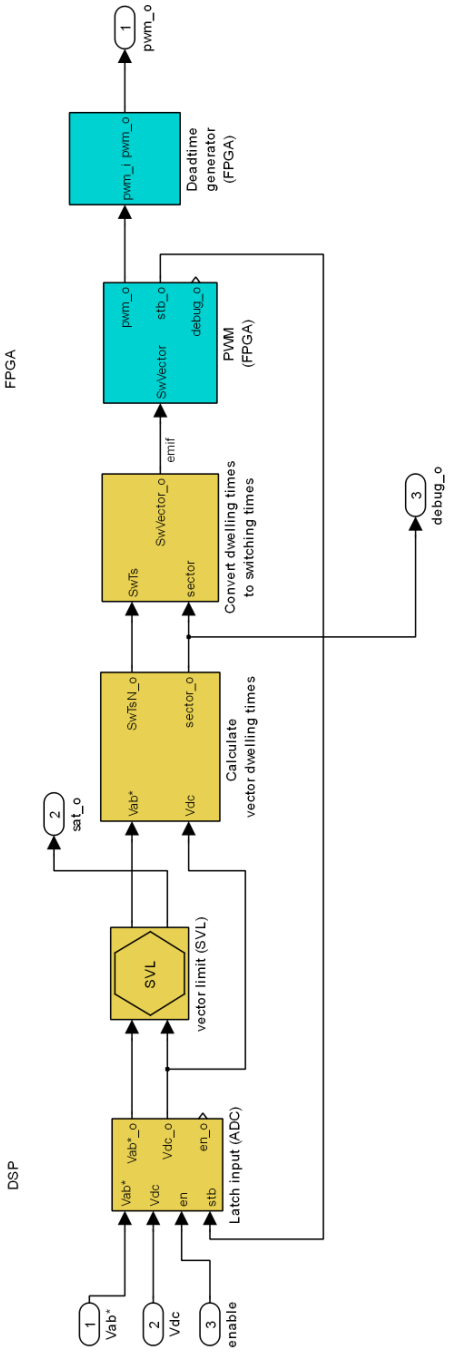

Figure B.4. Space vector pulse width modulator (SVPWM).

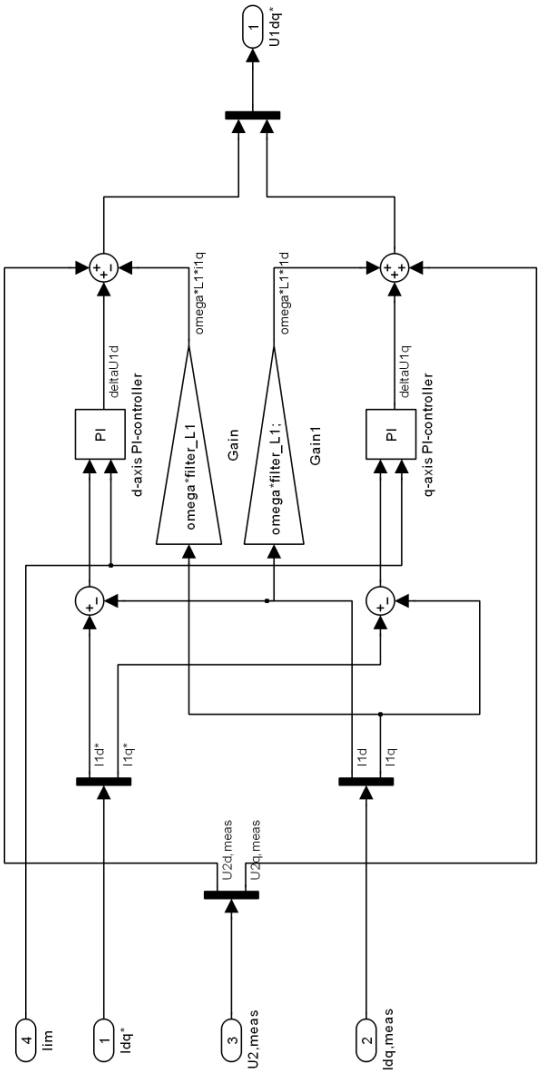

Figure B.5. Internal model control (IMC).

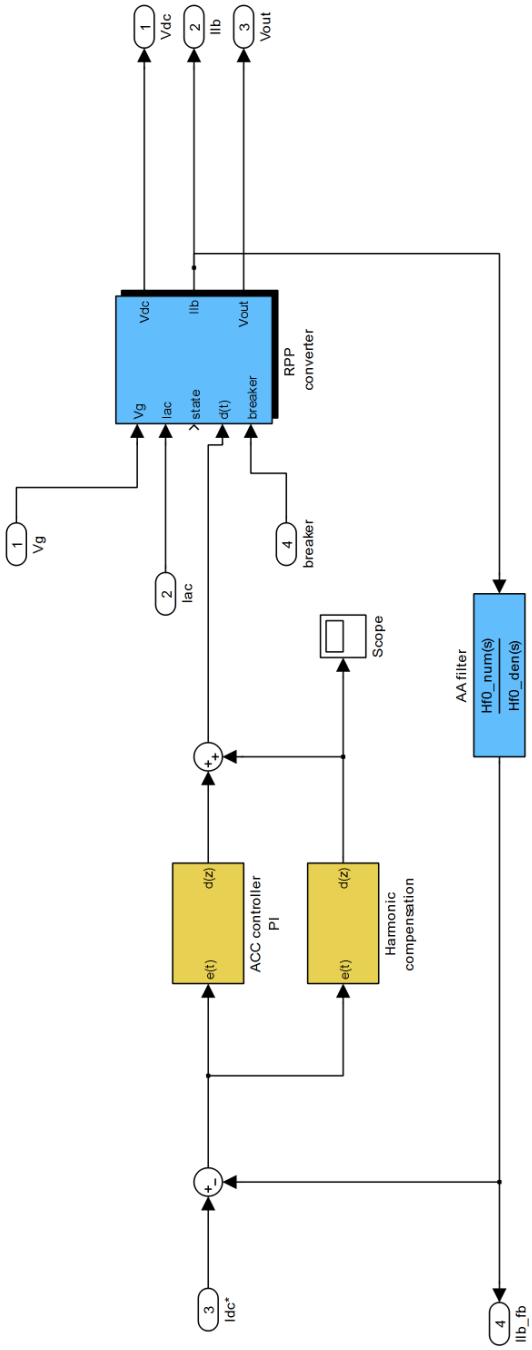

Figure B.6. Top-level model of the RPP converter.

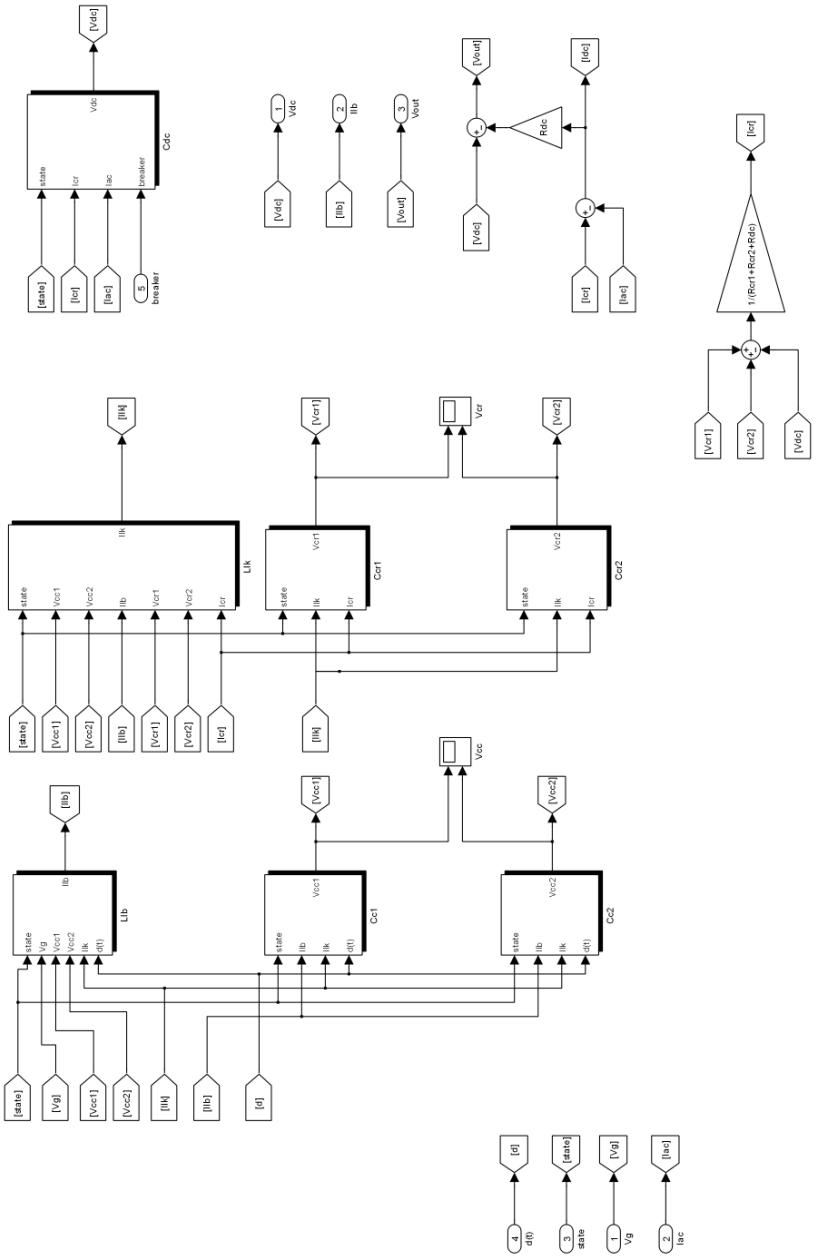

Figure B.7. Switching model of the RPP converter.

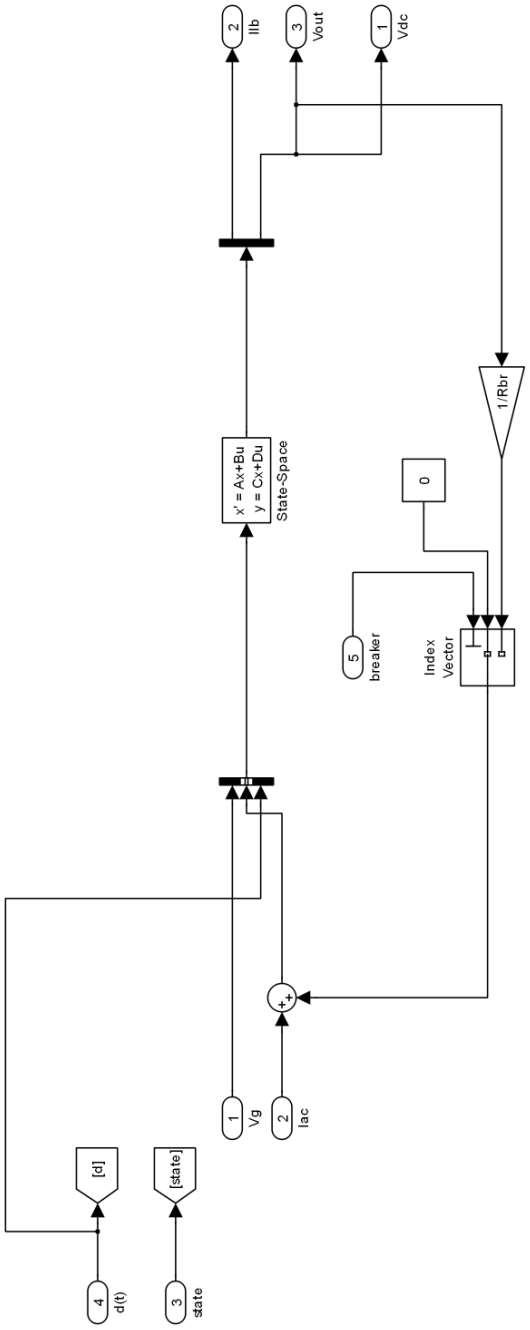

Figure B.8. State-space average model of the RPP converter.

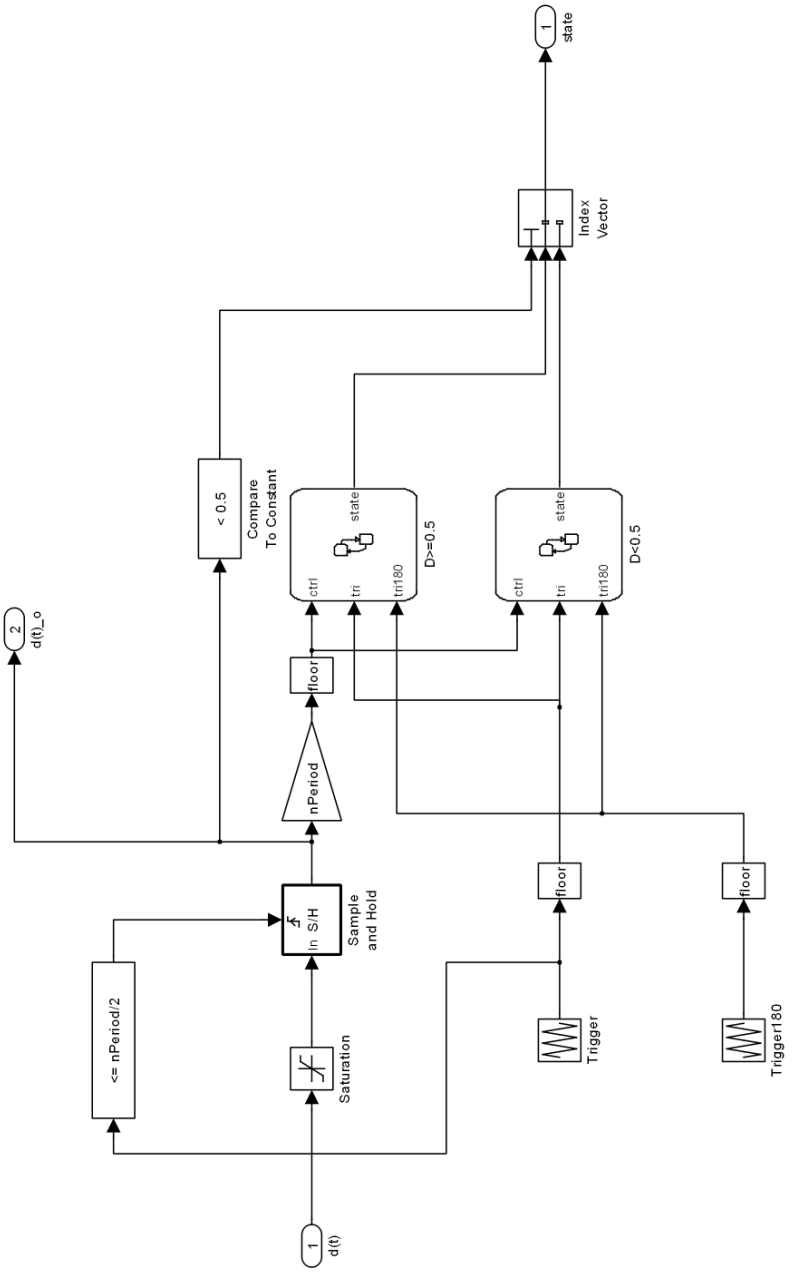

Figure B.9. Modulator used in the switching model of the RPP converter.

Appendix C

PCU test setup

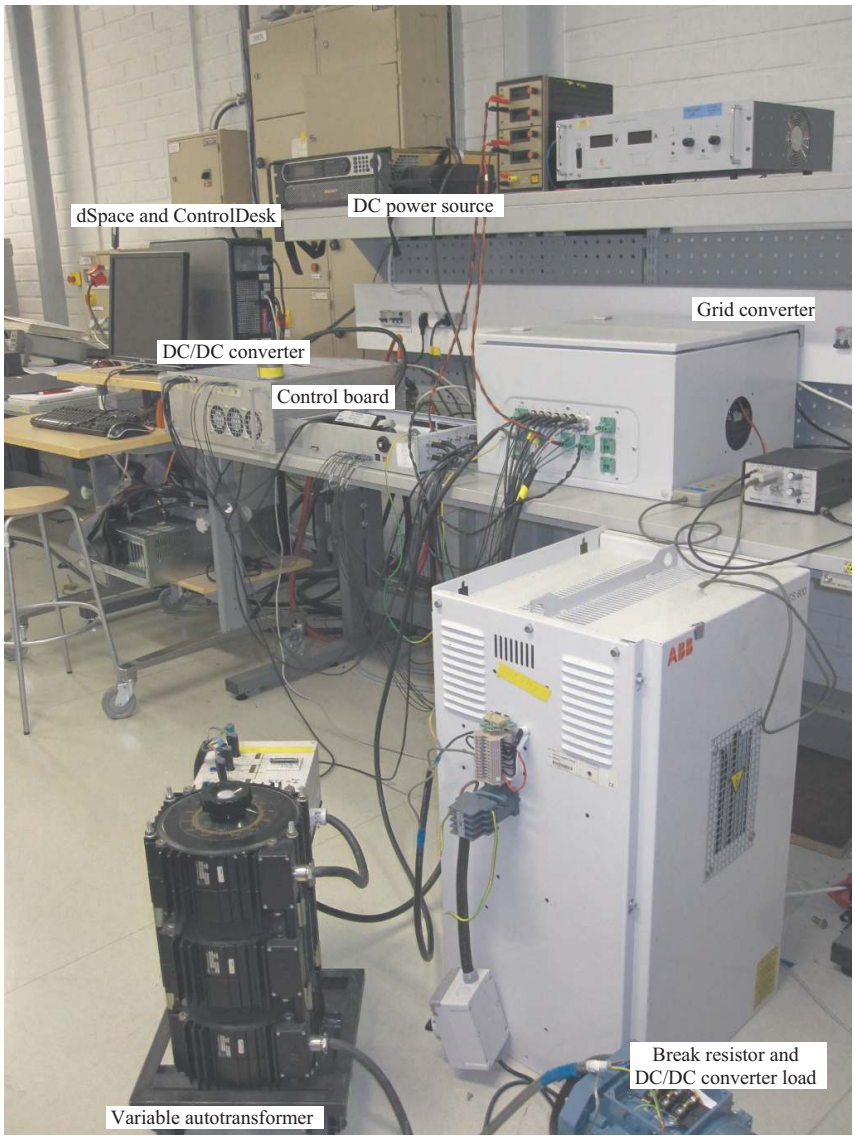

Figure C.1. Test setup used in the PCU measurements. The figure presents the test setup in the laboratory. The DC power supply feeds the DC/DC converter. The DC/DC converter is connected to the grid converter, which is tied to the utility grid with a variable autotransformer. The variable autotransformer is used to step down the grid voltage because of the problems with the VSI. A PC with ControlDesk and dSpace is used to monitor the system, while the control algorithms are implemented in the control board. The resistor load is used as a DC/DC load in the DC/DC converter measurements, and as a break resistor in the PCU measurements.

ACTA UNIVERSITATIS LAPPEENRANTAENSIS

451. MIELONEN, JARI. Making Sense of Shared Leadership. A case study of leadership processes and practices without formal leadership structure in the team context. 2011. Diss.

452. PHAM, ANH TUAN. Sewage sludge electro-dewatering. 2011. Diss.

453. HENNALA, LEA. Kuulla vai kuunnella – käyttäjää osallistavan palveluinnovoinnin lähestymistavan haasteet julkisella sektorilla. 2011. Diss.

454. HEINIMÖ, JUSSI. Developing markets of energy biomass – local and global perspectives. 2011. Diss.

455. HUJALA, MAIJA. Structural dynamics in global pulp and paper industry. 2011. Diss.

456. KARVONEN, MATTI. Convergence in industry evolution. 2011. Diss.

457. KINNUNEN, TEEMU .Bag-of-features approach to unsupervised visual object categorisation. 2011. Diss.

458. RUUSKANEN, VESA. Design aspects of megawatt-range direct-driven permanent magnet wind generators. 2011. Diss.

459. WINTER, SUSANNA. Network effects: scale development and implications for new product performance. 2011. Diss.

460. JÄÄSKELÄINEN, ANSSI. Integrating user experience into early phases of software development. 2011. Diss.

461. KÄÄRIÄINEN, TOMMI. Polymer surface modification by atomic layer deposition. 2011. Diss.

462. KOCHURA, ALEKSEY. Growth, magnetic and transport properties of InSb and II-IV-As2 semiconductors doped with manganese. 2011. Diss.

463. PUTKIRANTA, ANTERO. Possibilities and challenges of longitudinal studies in operations management. 2011. Diss.

464. HAPPONEN, ARI. Muuttuvaan kysyntään sopeutuva varastonohjausmalli. 2011. Diss.

465. VASAVA, PARITOSH. Application of computational fluid dynamics in modelling blood flow in human thoracic aorta. 2011. Diss.

466. PURO, LIISA. Identification of extractives and polysaccharides as foulants in membrane filtration of pulp and paper mill effluents. 2011. Diss.

467. LAPPALAINEN, PIA. Socially Competent Leadership – predictors, impacts and skilling in engineering. 2012. Diss.

468. PLAMTHOTTATHIL, ANSHY OONNITTAN. Application of electrokinetic Fenton process for the remediation of soil contaminated with HCB. 2012. Diss.

469. EBRAHIMI, FATEMEH. Synthesis of percarboxylic acids in microreactor. 2012. Diss.

470. JANTUNEN, SAMI. Making sense of software product requirements. 2012. Diss.

471. VILKO, JYRI. Approaches to supply chain risk management: identification, analysis and control. 2012. Diss.

472. TANSKANEN, VESA. CFD modelling of direct contact condensation in suppression pools by applying condensation models of separated flow. 2012. Diss.

473. HUHTANEN MIKKO. Software for design of experiments and response modelling of cake filtration applications. 2012. Diss.

474. PARJANEN, SATU. Creating possibilities for collective creativity
Brokerage functions in practice-based innovation. 2012. Diss.

475. KUKKONEN, SAKU. Generalized differential evolution for global multi-objective optimization with constraints. 2012. Diss.

476. LAAKSONEN, JONNA. Tactile-proprioceptive robotic grasping. 2012. Diss.

477. KALLIO, ANNE. Enhancing absorptive capacity in a non-research and development context
An action research approach to converting individual observations into organizational awareness. 2012. Diss.

478. LÄTTILÄ, LAURI. Improving transportation and warehousing efficiency with simulation based decision support systems. 2012. Diss.

479. OYOMNO, WERE. Usable privacy preservation in mobile electronic personality. 2012. Diss.

480. LINNALA, MIKKO. Simulation and optimization tools in paper machine concept design. 2012. Diss.

481. KORPIJÄRVI, JUHA. Aging based maintenance and reinvestment scheduling of electric distribution network. 2012. Diss.

482. KORHONEN, JUHAMATTI. Active inverter output filtering methods. 2012. Diss.

483. KLODOWSKI, ADAM. Flexible multibody approach in bone strain estimation during physical activity: quantifying osteogenic potential. 2012. Diss.

484. VUORENMAA, MARKKU. Osaamisen johtaminen pk-yrityksen kansainvälisen kasvun elinkaarella. 2012. Diss.

485. RAUTIAINEN, MARITA. Dynamic ownership in family business systems – a portfolio business approach. 2012. Diss.

486. LILIUS, REIJO. THE FINNISH IT INDUSTRIES IN TRANSITION Defining and measuring the Finnish software product and IT services industries by applying theoretical frameworks . 2012. Diss.

487. TUOMINEN, PASI. The purpose of consumer co-operation: implications for the management and governance of co-operatives. 2012. Diss.

488. SAARI, ESA. Suurnopeus-turbokoneroottoreiden termodynaaminen ja mekaaninen mallinnus sekä rakenneanalyysi. 2012. Diss.

489. PAANANEN, MIKKO. On innovative search: the use of internal and external sources of innovation among Finnish innovators. 2012. Diss.

490. BELOVA, POLINA. Quasiclassical approach to the vortex state in iron-based superconductors. 2012. Diss.

491. HIETANEN, IIRO. Design and characterization of large area position sensitive radiation detectors. 2012. Diss.

492. PÄSSILÄ, ANNE. Reflexive model of research-based theatre – processing innovation of the cross-road of theatre, reflection and practice-based innovation activities. 2012. Diss.